



<https://theses.gla.ac.uk/>

Theses Digitisation:

<https://www.gla.ac.uk/myglasgow/research/enlighten/theses/digitisation/>

This is a digitised version of the original print thesis.

Copyright and moral rights for this work are retained by the author

A copy can be downloaded for personal non-commercial research or study, without prior permission or charge

This work cannot be reproduced or quoted extensively from without first obtaining permission in writing from the author

The content must not be changed in any way or sold commercially in any format or medium without the formal permission of the author

When referring to this work, full bibliographic details including the author, title, awarding institution and date of the thesis must be given

Enlighten: Theses

<https://theses.gla.ac.uk/>  
[research-enlighten@glasgow.ac.uk](mailto:research-enlighten@glasgow.ac.uk)

# Interferometry Developments for Spaceborne Gravitational Wave Detectors

Christian J Killow, M.Sc.

Department of Physics and Astronomy,  
University of Glasgow

Presented as a thesis for the degree of Ph.D.  
in the University of Glasgow, University Avenue,  
Glasgow G12 8QQ

© C J Killow, 2005

May 2, 2006

ProQuest Number: 10753987

All rights reserved

INFORMATION TO ALL USERS

The quality of this reproduction is dependent upon the quality of the copy submitted.

In the unlikely event that the author did not send a complete manuscript and there are missing pages, these will be noted. Also, if material had to be removed, a note will indicate the deletion.



ProQuest 10753987

Published by ProQuest LLC (2018). Copyright of the Dissertation is held by the Author.

All rights reserved.

This work is protected against unauthorized copying under Title 17, United States Code  
Microform Edition © ProQuest LLC.

ProQuest LLC.  
789 East Eisenhower Parkway  
P.O. Box 1346  
Ann Arbor, MI 48106 – 1346

GLASGOW  
UNIVERSITY  
LIBRARY:

# Contents

<b>Acknowledgements</b>	<b>xxiii</b>
<b>Preface</b>	<b>xxvi</b>
<b>Summary</b>	<b>xxix</b>
<b>Acronyms</b>	<b>xxxiii</b>
<b>1 Gravitational waves and detectors</b>	<b>1</b>
1.1 The origin of gravitational waves . . . . .	1
1.2 Sources of gravitational waves . . . . .	3
1.3 Gravitational wave detection . . . . .	6
1.3.1 Ground based detectors . . . . .	7
1.3.2 Detectors in space . . . . .	11

<b>2</b>	<b>Testing critical technologies for LISA</b>	<b>14</b>
2.1	LTP interferometry . . . . .	16
2.2	LTP noise sources . . . . .	22
2.2.1	Laser power fluctuations . . . . .	22
2.2.2	Laser frequency noise . . . . .	24
2.2.3	Path length changes . . . . .	25
2.2.4	Phase information lost at quadrant photodiodes . . . . .	27
2.2.5	Stray light . . . . .	28
2.2.6	Measurement noise . . . . .	29
2.3	Validation of LTP style interferometry . . . . .	31
<b>3</b>	<b>LISA Pathfinder prototype optical bench design and construction</b>	<b>32</b>
3.1	Design of the prototype optical bench . . . . .	33
3.1.1	Design considerations . . . . .	33
3.1.2	Choice of materials . . . . .	34
3.1.3	Layout of interferometer . . . . .	36
3.1.4	Beam path lengths . . . . .	39
3.1.5	Tolerances . . . . .	42

3.1.6	Component Design . . . . .	47
3.1.7	Method of construction . . . . .	48
3.1.8	Non-adjustable components . . . . .	49
3.1.9	Adjustable components . . . . .	51
3.2	Construction . . . . .	54
3.2.1	Verification of component perpendicularity . . . . .	55
3.2.2	Non-adjustable component bonding . . . . .	60
3.2.3	Adjustable component bonding . . . . .	61
3.3	Contrast of output signals . . . . .	62
<b>4</b>	<b>LISA Pathfinder prototype optical bench interferometry</b>	<b>66</b>
4.1	Experimental setup . . . . .	66
4.1.1	Laser injection bench . . . . .	67
4.1.2	Phase measurement system . . . . .	71
4.2	Test environment . . . . .	75
4.3	Optical bench noise performance . . . . .	75
4.3.1	Initial performance . . . . .	77
4.3.2	Amplitude stabilisation . . . . .	80

4.3.3	Reducing <i>rf</i> pickup . . . . .	81
4.3.4	Beam size and position investigations . . . . .	82
4.3.5	Frequency noise . . . . .	87
4.3.6	Fibre noise investigations . . . . .	91
4.3.7	Tests with a prototype LTP style phasemeter . . . . .	97
4.3.8	Noise performance using quadrant photodiodes . . . . .	99
4.3.9	Identifying temperature dependency . . . . .	100
<b>5</b>	<b>LISA Pathfinder engineering model optical bench construction</b>	<b>108</b>
5.1	Design goals . . . . .	109
5.2	Size and component density . . . . .	110
5.3	Fibre injectors . . . . .	111
5.4	Alignment strategy . . . . .	112
5.5	Photodiodes . . . . .	114
5.6	Repairing broken components . . . . .	114
5.7	Test results . . . . .	115
<b>6</b>	<b>LISA Technology Package optical bench developments</b>	<b>117</b>

6.1	Fibre injectors . . . . .	117
6.1.1	New fibre injector design . . . . .	118
6.1.2	Fibre injector construction . . . . .	120
6.1.3	Fibre injector optical subassembly alignment . . . . .	123
6.2	Alignment tolerances . . . . .	125
6.3	Alignment strategy . . . . .	127
6.3.1	Beam measurement . . . . .	127
6.3.2	Precision metrology . . . . .	129
6.4	Alternative adjustable bonding technique . . . . .	131
<b>7</b>	<b>Weak light phase locking for LISA</b>	<b>137</b>
7.1	Introduction . . . . .	137
7.2	Concept . . . . .	139
7.3	Laboratory demonstration . . . . .	140
7.3.1	Phase stability of interferometers . . . . .	141
7.3.2	The need for signal demodulation . . . . .	142
7.4	Subsystems . . . . .	145
7.4.1	The phase measurement system and associated electronics	145

7.4.2	Signal demodulation . . . . .	149
7.4.3	Testing of <i>rf</i> amplifiers . . . . .	152
7.4.4	Optical signal generation . . . . .	155
7.4.5	Phase locking servo . . . . .	156
7.4.6	Test of measurement electronics using optical signals . .	157
7.4.7	Attenuation . . . . .	159
7.5	Current status . . . . .	161
<b>8</b>	<b>Conclusions</b>	<b>162</b>
<b>A</b>	<b>Optical test bench</b>	<b>164</b>
A.1	Approach . . . . .	164
A.1.1	LTP modulation scheme . . . . .	165
A.1.2	LISA modulation scheme . . . . .	166
A.2	Test bench layout . . . . .	169
<b>B</b>	<b>Optical fibre positioning unit</b>	<b>171</b>
B.1	LISA requirements . . . . .	172
B.2	Relating fibre end movement to optical bench field of view and to telescope field of view . . . . .	173

B.2.1	Calculating lateral translation of fibre end to telescope field of view relationship . . . . .	176
B.2.2	Calculating defocus of beam from fibre to telescope field of view relationship . . . . .	177
B.3	Measurement requirements . . . . .	180
B.4	Current status . . . . .	180
<b>C</b>	<b>Investigation of amplitude modulation created by acousto- optic modulators</b>	<b>182</b>
	<b>Bibliography</b>	<b>188</b>

# List of Figures

1.1	<i>Illustration showing the two independent linear polarisations of a gravitational wave acting on a ring of free particles. Wave has amplitude 0.2 (Source [1]). . . . .</i>	4
1.2	<i>Graph showing how space based and ground based observations will complement each other by covering a different frequency range with similar sensitivities (Source [1]). . . . .</i>	13
2.1	<i>Schematic showing the principle of the heterodyne interferometry.</i>	16
2.2	<i>Optical model of the LTP reference interferometer. . . . .</i>	19
2.3	<i>Optical model of the LTP frequency noise interferometer. . . . .</i>	19
2.4	<i>Optical model of the LTP <math>x_1</math> interferometer. . . . .</i>	20
2.5	<i>Optical model of the LTP <math>x_1 - x_2</math> interferometer. . . . .</i>	20
2.6	<i>Optical model of the LTP optical bench interferometer. Dimensions are in metres. . . . .</i>	21
2.7	<i>Optical model of the LTP interferometers showing all stray beams.</i>	30

2.8	<i>Optical model of the LTP interferometers showing the stray beam dumps.</i> . . . . .	30
3.1	<i>Layout of optical paths on the prototype optical bench</i> . . . . .	37
3.2	<i>Lateral beam shift on transmission with changing entry angle.</i> .	46
3.3	<i>Lateral beam shift on transmission with changing component thickness.</i> . . . . .	47
3.4	<i>Close up of brass template showing locating surfaces and corners with radii removed.</i> . . . . .	49
3.5	<i>The brass alignment template for bonding the prototype optical bench. The hinges for aligning adjustable components are shown attached to the template.</i> . . . . .	50
3.6	<i>CAD drawing of left handed fine adjuster. The light blue cuboid represents a mirror/beamsplitter component.</i> . . . . .	52
3.7	<i>Photograph of a 'composite component' - two normal components water bonded together</i> . . . . .	55
3.8	<i>Photograph viewing through a water bond</i> . . . . .	55
3.9	<i>Diagrams showing 'composite' mirror (side view) of components 'P' and 'Q'. The blue rectangles indicate the mirror coating: a. showing cancelation of component error angles due to non-perpendicularity of bonding and reflecting surfaces, b. manifestation of error angle showing component imperfection.</i> . . . .	56

3.10	<i>Diagram showing ‘composite’ mirror (side view) with variation of bond thickness negating component error angle . . . . .</i>	58
3.11	<i>Flatness measurement of two water bonded components before repolishing. . . . .</i>	59
3.12	<i>Flatness measurement of two water bonded components after repolishing. . . . .</i>	59
3.13	<i>OB after first nine components have been bonded, showing the brass alignment template in position above the baseplate . . . . .</i>	61
3.14	<i>Prototype optical bench during bonding showing fibre couplers and quadrant photodiode attached to invar mount (foreground) and adjusters (back right) . . . . .</i>	62
3.15	<i>Fully bonded optical bench with fibre couplers attached to invar mount . . . . .</i>	63
3.16	<i>Heterodyne signals at the output of the optical bench upon installation. . . . .</i>	64
3.17	<i>Heterodyne signals at the output of the optical bench (with improved contrast in the frequency noise arm). . . . .</i>	65
4.1	<i>Schematic layout of laser injection bench, prototype optical bench, measurement photodiodes and phase measurement system. The optical beam colour key used in Figure 3.1 is also used here. . . . .</i>	67

4.2	<i>Photograph of the laser injection bench. Beam paths are shown using the same colour key as Figure 3.1. . . . .</i>	68
4.3	<i>Plot showing beam parameter fitting. The red crosses are measured data points and the blue line is the fitted data. . . . .</i>	70
4.4	<i>Principle of the ‘stopwatch’ style phasemeter. . . . .</i>	72
4.5	<i>Circuit diagram of the 10 kHz measurement photodiodes. . . . .</i>	72
4.6	<i>Photograph of the logic chips in the ‘stopwatch’ style phasemeter. . . . .</i>	74
4.7	<i>Time series of temperature variations in the test facility. . . . .</i>	76
4.8	<i>Power spectral density of temperature variations in the test facility. . . . .</i>	76
4.9	<i>Time series showing initial noise performance of optical bench. The data was taken over 16 hours. . . . .</i>	78
4.10	<i>PSD showing initial noise performance of optical bench. The green curve is the measurement channel and the blue curve is the frequency noise channel. The red line is the LTP interferometry goal. . . . .</i>	78
4.11	<i>Time series showing noise performance of optical bench under vacuum. The data was taken over 17 hours. . . . .</i>	79
4.12	<i>PSD showing noise performance of optical bench under vacuum. The green curve is the measurement channel and the blue curve is the frequency noise channel. The red line is the LTP interferometry goal. . . . .</i>	79

4.13	<i>Layout of the power stabilisation servo. Wires are denoted by black lines and laser light (of all frequencies) by red lines. Only one AOM and feedback path is shown for clarity. . . . .</i>	81
4.14	<i>Diagram showing effect of beam jitter on measured phase at photodiode. . . . .</i>	84
4.15	<i>Apparent phase change as a photodiode is moved across an output beam. . . . .</i>	86
4.16	<i>Times series plot showing effect of 1 Hz modulation of laser frequency on measurement and frequency noise output signals. . . .</i>	88
4.17	<i>Phase spectral density plot showing effect of 1 Hz modulation of laser frequency on measurement and frequency noise output signals. . . . .</i>	89
4.18	<i>Phase spectral density plot showing noise performance of the prototype optical bench with and without frequency noise correction. The red line is the LTP interferometry goal. The residual noise bulge above the interferometry goal is due to noise sources that had not been identified at that time. . . . .</i>	90
4.19	<i>Phase spectral density plot showing noise performance of the prototype optical bench with frequency stabilisation servo implemented. The green curve exhibits the frequency modulation spikes, which are removed by frequency noise subtraction (magenta curve). The red line is the LTP interferometry goal. . . .</i>	91
4.20	<i>Photograph of the piezo mounted mirror for path length stabilisation. The beam path is indicated by a red line. . . . .</i>	93

4.21	<i>PSD showing noise performance of the optical bench with the piezo mount path length servo in operation. The red line is the LTP interferometry goal. . . . .</i>	94
4.22	<i>Temperature spectrum during the data run shown in Figure 4.21. The larger variations are from a sensor mounted on a measurement photodiode and the other three curves are from sensors mounted inside the vacuum tank. . . . .</i>	94
4.23	<i>Diagram showing how a small vector at the heterodyne frequency of varying phase can influence the optical phase measurement. .</i>	95
4.24	<i>Photograph of a section of fibre with heater wire. The wire is insulated from the optical table by a sheet of acetate. . . . .</i>	97
4.25	<i>PSD showing noise performance of the optical bench with the fibre heater path length servo in operation. The red line is the LTP interferometry goal. . . . .</i>	98
4.26	<i>Temperature spectrum during the data run shown in Figure 4.25. The larger variations are from a sensor mounted on a measurement photodiode and the other three curves are from sensors mounted inside the vacuum tank. . . . .</i>	98
4.27	<i>PSD showing noise performance of the optical bench with the piezo mounted mirror path length servo in operation, the LTP prototype AOM unit and LTP style phasemeter. The red line is the LTP interferometry goal. . . . .</i>	99
4.28	<i>PSD showing apparent path length stability of optical bench with reference photodiode being heated at 3 mHz. . . . .</i>	101

4.29	<i>Temperature spectrum during the data run shown in Figure 4.28. The blue (top) curve shows the temperature spectrum as measured at the reference photodiode. . . . .</i>	102
4.30	<i>Photograph of the fibre injector heaters. The superimposed green arrows indicate direction of light through the fibres onto the optical bench and the heaters are circled in red. . . . .</i>	103
4.31	<i>PSD of apparent path length difference whilst temperature modulating areas of the optical bench. The main bench was heated at 4 mHz, fibre injector mount 1 at 5 mHz and BS7 at 6 mHz. . .</i>	103
4.32	<i>PSD of measured temperature variations during temperature modulation of the optical bench during the run shown in Figure 4.31.</i>	104
4.33	<i>Photograph of the prototype optical bench in the vacuum enclosure with heaters. The bulk optical bench heaters are circled in green, the fibre injector heaters in blue and the individual component heater in red. . . . .</i>	105
4.34	<i>PSD of apparent path length difference whilst temperature modulating the optical bench ‘uniformly’ at 8 mHz. . . . .</i>	106
4.35	<i>PSD of measured temperature variations during temperature modulation of the optical bench during the run shown in Figure 4.34.</i>	106
5.1	<i>The adjustable arms used to position components prior to bonding (photograph courtesy of CCLRC Rutherford Appleton Laboratory). . . . .</i>	110

5.2	<i>The engineering model fibre injectors (photograph courtesy of CCLRC Rutherford Appleton Laboratory).</i> . . . . .	112
5.3	<i>The principle of adjustable component manipulation for the engineering model optical bench construction. The black (solid) lines indicate initial adjuster and component position and the red (dashed) lines after adjustment</i> . . . . .	113
5.4	<i>The completed engineering model optical bench (photograph courtesy of CCLRC Rutherford Appleton Laboratory).</i> . . . . .	115
6.1	<i>Sketch showing the new fibre injector design. The laser beam is indicated in red.</i> . . . . .	119
6.2	<i>Photograph of a fibre with welded pellet (clamped in a metal V-groove).</i> . . . . .	119
6.3	<i>Screen capture of reconstructed 3-D profile of beam a short distance from pellet end.</i> . . . . .	119
6.4	<i>Plot of the beam radius squared as a function of distance from the pellet end. Red crosses show measured data points and the blue line shows the fitted hyperbola from which the beam parameters were extracted.</i> . . . . .	121
6.5	<i>Plot of the beam radius as a function of distance from the pellet end. Red crosses show measured data points and the blue dashed line shows the fitted hyperbola.</i> . . . . .	122

6.6	<i>Diagram showing the coordinate system for the optical bench interferometer. Taken from the LTP Optical Metrology Sub-assembly Requirement Specification [2]. . . . .</i>	124
6.7	<i>Diagram showing the concept of fibre injector alignment with respect to the baseplate. . . . .</i>	125
6.8	<i>CAD drawing showing the fibre injector optical subassemblies in place. The ruler has 10 mm graduations for reference. . . .</i>	126
6.9	<i>Schematic showing alignment of the beam to test mass 2 using mirror M4. The distance of 0.2m is exaggerated slightly as a precaution so as not to underestimate the required sensitivity. . .</i>	127
6.10	<i>CAD drawing of quadrant photodiode mount. The hole visible at the centre of the left side face is the photodiode location. . . .</i>	128
6.11	<i>Photograph of the coordinate measuring machine used for precision metrology (left) and one of the Zerodur® baseplate blanks being measured (right). . . . .</i>	129
6.12	<i>Diagram showing quadrant photodiode calibration, viewing along beam axis. In the right hand diagram the mount has been rotated 180° and is indicated using red dashed lines. . . . .</i>	130
6.13	<i>Photograph of a ground surface on a representative fused silica component. . . . .</i>	133
6.14	<i>Photograph of nine of the 12 ground bonding strength test pieces.</i>	135
6.15	<i>Photograph of a test piece (TM006) in the strength testing machine. . . . .</i>	135

6.16	<i>Plot showing the force required to break the ground bonds (in terms of equivalent number of g) against the time since bonding. The blue triangles are data points and the red line is the 80g static load qualification threshold. The four batches of three components shown were tested after approximately one hour, five hours, 16 hours and seven days. . . . .</i>	135
7.1	<i>Conceptual schematic of the phase locking loop between two LISA spacecraft showing incoming weak light and outgoing phase locked light. Laser beams are indicated by red lines. . . . .</i>	139
7.2	<i>Conceptual schematic of a single arm of one LISA spacecraft showing incoming weak light and outgoing phase locked light. Laser beams are indicated by red lines. . . . .</i>	140
7.3	<i>Conceptual schematic of experimental layout to demonstrate weak light phase locking. Laser beams are indicated by red lines. The 10 kHz reference for the PMS is generated by mixing the two signal generator outputs in order to achieve the stability needed. . . . .</i>	141
7.4	<i>Schematic of experimental layout to demonstrate weak light phase locking showing the dual path analogue and digital feedback. Laser beams are indicated by red lines. The 15 MHz and 15.01 MHz signal generators are phase locked together. . . . .</i>	144
7.5	<i>Diagram showing set up for phase stability testing of comparators and phasemeter. . . . .</i>	146

7.6 *PSD showing result of test set up shown in Figure 7.5. Channels one and four are two measurement channels and channel five is the difference between one and four. The red line is the LTP interferometry goal, shown for reference. The LISA goal is  $6 \mu\text{cycles}/\sqrt{\text{Hz}}$ .* . . . . . 146

7.7 *Diagram showing set up for phase stability testing of mixers.* . . 147

7.8 *PSD showing result of test set up shown in Figure 7.7. Channels one and four are two measurement channels and channel five is the difference between one and four. The red line is the LTP interferometry goal, shown for reference. The LISA goal is  $6 \mu\text{cycles}/\text{sqrtHz}$ .* . . . . . 148

7.9 *Amplitude response of the 10 kHz low pass filters used prior to the phasemeter.* . . . . . 148

7.10 *Diagram showing the signal splitting and demodulation scheme for the full experiment. ‘LP’ denotes a low pass filter, ‘S’ a 50:50 signal splitter, ‘p.d.’ a photodiode and ‘X’ mixers. The red dashed line indicates the limits of the circuit board used to demodulate the high frequency signals to 10 kHz outputs. The constituents of the PMS are within the blue dashed line.* . . . . . 149

7.11 *Photograph of the signal splitting and demodulation board. One of the 50:50 signal splitters is boxed with a blue dashed line and one of the mixers with a green dashed line. The 10 kHz outputs go to the filters and PMS.* . . . . . 150

7.12	<i>Diagram showing the set-up being used to test the amplifiers using only electrically generated signals. ‘S’ indicates a 50:50 signal splitter and ‘X’ a mixer. The red dashed line indicates the limits of the demodulation board and the blue dashed line the PMS.</i>	153
7.13	<i>PSD showing phase stability of the amplifiers. Channels one and two are the phase stability of the amplifiers with respect to the electrical reference. The red line shows the interferometry target sensitivity, which is set by the shot noise limit of the weak light interference.</i>	154
7.14	<i>Photograph of the laser preparation bench.</i>	155
7.15	<i>Diagram showing the set up for the test of the measurement electronics using an optical signal.</i>	158
7.16	<i>PSD showing apparent phase stability of the independently measured in-loop signal (channel one) and the locking signal (channel two) with respect to the electrical reference signal. The red line shows the interferometry target sensitivity, which is set by the shot noise limit of the weak light interference.</i>	158
7.17	<i>Photograph of the beam attenuator subassembly.</i>	160
7.18	<i>Photograph of the beam attenuator subassembly in place on the optical bench (circled in red).</i>	160
A.1	<i>Schematic layout of the LTP side of the optical test bench.</i>	165

A.2	<i>Drive signal to AOM (blue) and optical signal (red) with no control loop. . . . .</i>	166
A.3	<i>Drive signal to AOM (blue), in loop signal (orange) and independent optical signal (red) with control loop on (the red line is entirely obscured by the blue trace). . . . .</i>	167
A.4	<i>Modeled (blue) and actual (red) control loop performance. . . . .</i>	167
A.5	<i>Schematic layout of the LISA side of the optical test bench. . . . .</i>	168
A.6	<i>Schematic layout of optical test bench showing the beam path and optical elements. . . . .</i>	169
A.7	<i>Schematic layout of optical test bench showing the beam power and optical matching. . . . .</i>	170
A.8	<i>Photograph of optical test bench. The superimposed red lines indicate the LTP test beams and the blue lines the LISA test beams. . . . .</i>	170
B.1	<i>Schematic of the LISA optical bench. . . . .</i>	172
B.2	<i>Effect of lateral fibre end movement on optical bench field of view. . . . .</i>	174
B.3	<i>Effect of fibre end translation on optical bench field of view. . . . .</i>	174
B.4	<i>Effect of optical bench field of view on telescope field of view for lateral translation. . . . .</i>	175
B.5	<i>Effect of optical bench field of view on telescope field of view for defocus. . . . .</i>	175

B.6	<i>Diagram showing parameters for calculating effect of lateral displacement of fibre end. . . . .</i>	176
B.7	<i>Lateral translation of fibre end versus telescope field of view. . .</i>	178
B.8	<i>Diagram showing parameters for calculating effect of defocus. . .</i>	179
B.9	<i>Lateral translation of fibre end versus telescope field of view. . .</i>	179

# List of Tables

3.1 Optical properties of potential beamsplitter substrates . . . . . 35

4.1 Beam diameters (in  $\mu\text{m}$ ) at output photodiodes. . . . . 84

# Acknowledgements

I would like to convey my deepest gratitude to Harry Ward, Dave Robertson and Ken Strain. They have influenced my thinking most of all and I am indebted to them for all their help.

The uncompromising efforts of Jim Hough make the IGR a productive and fulfilling place to be and I thank him for his help, both direct and indirect.

Mike Perreur-Lloyd and Russell Jones have provided countless CAD models and engineering help with very unique bits of apparatus. They've also been great people to share time with. Many thanks.

Eoin Elliffe successfully transferred a subset of his bonding knowledge to me, sufficient to enable me to achieve my goals. His transfer of chess wisdom was marginally less successful, but thank you for trying.

I was helped during the bonding of the prototype optical bench by Jim Hough and Johanna Bogenstahl for which I am very grateful.

Thank you to Gavin Newton for revealing some of the black art of *rf* electronics to me and telling me how to go about soldering a capacitor that you can barely see.

Thanks to the technicians of the IGR who have been kept busy supplying ever expanding experiments with kit: Stevie Craig, Colin Craig, Allan Latta and Neil Robertson.

Thank you to all in the IGR for your help and your humour. Especially those who have had to suffer me as an office mate: Bryan Barr, Dave Crooks, Eoin Elliffe and Peter Sneddon way back when, Peter Murray, Stuart Reid and Bob Taylor not so long ago and now MPL, Jonesy and Johanna.

My colleagues in Hannover have provided many interesting conversations, much help and have been a pleasure to work (and play) with. Danke schön Gerhard Heinzl, Frank Steier, Vinzenz Wand and Antonio García. A special thank you to Felipe Guzmán Cervantes for generating the LTP optical models.

Thanks to Kevin Middleton and Martin Caldwell at RAL who fulfilled their supervisory duties and then some. I look forward to working with you again in the future.

I would also like to thank my sixth form physics teacher, John Carrington, who helped me to see what a rewarding field physics can be.

I wish to acknowledge the support of the Particle Physics and Astronomy Research Council for supporting me during my Ph.D. and the CCLRC Rutherford Appleton Laboratory for providing my CASE studentship award.

A big thank you to a special little lady: thank you Gail for all your support and encouragement.

I would not have been able or willing to have seen and done so many things without the all-encompassing support of my family. Diolch yn fawr.

*“We have a hunger of the mind which asks for knowledge of all around us,  
and the more we gain, the more is our desire; the more we are capable  
of seeing.”*

Maria Mitchell (1811-1889)

# Preface

This thesis is an account of work carried out between October 2001 and October 2005 towards interferometry for spaceborne gravitational wave detectors.

Chapter 1 gives a brief overview of the nature of gravitational waves and of present and future detectors, particularly the planned space based gravitational wave detector LISA. This work is derived from published literature.

Chapter 2 examines the critical technologies for LISA that will be tested on the technology demonstrator mission LISA Pathfinder. Of these technologies the interferometry of the LISA Technology Package on board LISA Pathfinder is described and the expected noise sources defined. This work is derived from published literature.

Chapter 3 describes the design and construction of a prototype optical bench interferometer. This optical bench was created to demonstrate the possibility of building similar benches for LISA Pathfinder and eventually LISA. The design of the optical bench was carried out by D. I. Robertson, H. Ward and the author. The bench was constructed by the author with assistance from J. Hough and J. Bogenstahl. The associated optical and electrical equipment built to enable the optical bench construction were assembled by the author with input from D. I. Robertson and H. Ward.

Chapter 4 describes a series of tests on the prototype optical bench to determine its intrinsic stability. The laser injection bench was the work of the author. The phasemeter was designed and constructed by H. Ward. The series of tests were carried out principally by the author with D. I. Robertson and H. Ward. The optical bench was also tested using a prototype LISA Technology Package phasemeter designed and built at the Albert Einstein Institute, Hannover. G. Heinzl, V. Wand and A. García from the Albert Einstein Institute were present in Glasgow and assisted in the experiments.

Chapter 5 describes the construction of the LISA Technology Package engineering model at the Rutherford Appleton Laboratory, Oxford. The engineering model was built by K. Middleton of the Rutherford Appleton Laboratory with on site assistance from the author and G. Heinzl of the Albert Einstein Institute, Hannover. The hydroxide-catalysis bonding technology used was transferred to the Rutherford Appleton Laboratory by the author with advice from J. Hough.

Chapter 6 reports on the current effort at the University of Glasgow towards building the flight model LISA Technology Package optical bench interferometer. This work is being carried out by a team including D. I. Robertson, H. Ward, M. Perreux-Lloyd and the author. F. Steier of the Albert Einstein Institute, Hannover assisted this work during the summer of 2005.

Chapter 7 describes an ongoing experiment investigating weak light phase locking relevant to the LISA mission. This experiment utilises the proven stable optical bench described in Chapters 3 and 4 and was carried out by the author with assistance from H. Ward and D. I. Robertson. Advice on *rf* circuitry was given by G. Newton.

Chapter 8 presents the conclusions of the reported work.

Appendix A describes the design and construction of an optical signal generation test bench to provide signals for a prototype phasemeter. The test bench provided both LISA Technology Package and LISA type signals. The test bench was designed by D. I. Robertson, H. Ward and the author. The test bench was constructed by the author and the tests carried out by D. I. Robertson.

Appendix B describes a study carried out by the author at the Rutherford Appleton Laboratory on the fibre positioning unit for LISA. This work will be used to carry out tests of potential technologies, which will be completed by staff at the Rutherford Appleton Laboratory. M. Caldwell and K. Middleton assisted the author with this work.

Appendix C is report that was submitted to the Albert Einstein Institute, Hannover as part of an extensive study being conducted there to define sideband-induced noise in the LISA Technology Package interferometer. The experiment described was constructed and executed by the author.

# Summary

The existence of gravitational waves is predicted by Einstein's General Theory of Relativity. They can be considered as a wave-like distortion of four dimensional spacetime. Gravitational waves are produced by systems with time varying quadrupole mass moment. Spacetime is a stiff elastic medium, implying that waves traveling through it will have small amplitudes and this makes their detection very challenging.

There are well established efforts towards the detection of gravitational waves using ground-based systems. These detectors are limited by a lower frequency limit of  $\sim 10$  Hz set by the gravity gradient wall, which is a consequence of being in a gravitationally noisy environment. However, there are many predicted sources of gravitational radiation of relatively large amplitude at lower frequencies. Thus to complement the ground based network of detectors a spaceborne detector, the Laser Interferometer Space Antenna (LISA), is planned.

Gravitational wave detection by interferometry on Earth involves displacement measurements of order  $10^{-18}$  m/ $\sqrt{\text{Hz}}$  on tens of millisecond timescales and over arm lengths of kilometers. In contrast, LISA requires the monitoring of 5 million kilometer baselines at a noise level of  $10^{-12}$  m/ $\sqrt{\text{Hz}}$  and over 1000 second timescales. So while the displacement sensitivities required of LISA may ap-

pear routine in the context of current ground-based detectors, the frequency regime and distances involved introduce new challenges.

In order to try and reduce some of the technological risks of LISA, a precursor mission (called LISA Pathfinder) will be flown to demonstrate performance of technologies that cannot be adequately demonstrated on Earth. LISA Pathfinder contains an experiment called the LISA Technology Package (LTP). The work presented in this thesis deals mainly with investigations of the interferometry that will be used in the LTP and in LISA, with particular emphasis on the identification of sources of excess noise and of methods to minimise their effects.

LTP will use interferometry to monitor the distance between two inertial proof masses. The goal is to demonstrate the performance of the inertial sensors to within an order of magnitude of that required for LISA. To do this the interferometer sensitivity is relaxed an order of magnitude from the LISA goal but is still technically very challenging.

The approach adopted to demonstrate the interferometry for LTP was to build a stable optical bench using hydroxide-catalysis bonding of optical components to a low thermal expansion baseplate. This is the construction approach to be used in LTP and likely to be adopted for LISA. The stability of the optical bench was then tested using an LTP style heterodyne interferometer arrangement and demonstrated to be stable to  $10 \text{ pm}/\sqrt{\text{Hz}}$  from 3 mHz to 30 mHz, with the exception of a minor spectral feature of temperature driven excess noise when operated in a laboratory environment.

The experience gained by constructing and testing the optical bench strongly influenced the techniques used to construct the engineering model LTP bench and the techniques that will be used for building the flight model. A significant

result of the interferometry investigations was the discovery of a previously unexpected noise source. This involved spurious coupling of fluctuations in relative length of the optical fibres used to convey light to the interferometer. Techniques to reduce the significance of the noise source were demonstrated and have now been adopted for LTP.

The stable optical bench was then used as part of an experiment designed to provide essential information for the interferometry of LISA. Due to the unprecedented armlength of the LISA interferometer the light received at the end of an arm has light power at the  $\sim 100$  pW level. The corresponding shot noise sets the level of phase information that can be determined. In the design of LISA this fundamental effect is planned to set the limit to sensitivity over a significant part of the frequency spectrum; other noise sources must therefore be reduced to have lesser significance.

In one mode of LISA operation a local laser on each of the three LISA spacecraft is phase-locked to the weak incoming light from another distant spacecraft. This weak-light phase locking has never been adequately demonstrated at LISA frequencies and noise performance. To address the need for such a demonstration the stable optical bench developed during the prototyping of the LTP interferometer is now being adapted to mimic the core part of a LISA phase locking arrangement. Essentially the proven dimensional stability of the interferometer is being used to replace the equivalently stable LISA arm length. The phase locking system requires extremely phase stable signal chains to reach the LISA sensitivity, of which the *rf* amplifier and demodulation topologies are seen as one of the few remaining noise sources preventing a full weak-light phase locking system being realised. The experimental progress is described, together with a route to the near term goal of a demonstration at the LISA performance goals.

Also reported is work describing the design and construction of a phase measurement test bench that provides optical signals to stimulate LTP and LISA prototype photodiodes and phase readout systems.

A study into the requirements and current options of actuators for fibre positioning needs on LISA is presented. This will lead to experimental testing of a potential actuator.

Finally, a report submitted as part of a large investigation into the cause of the previously identified noise source is included. It examines the production of frequency shifted laser beams by acousto-optic modulators driven by *rf* signals containing two spectral components and the resultant beat notes observed when the light is detected by a photodiode.

# Acronyms

Much of the content of this thesis discusses space-based projects which tend to be acronym-rich. All acronyms are defined prior to use but an acronym list is included for reference.

Acronym	Definition
AEI	Albert Einstein Institute
AIGO	Australian International Gravitational Observatory
AOM	Acousto-Optic Modulator
BP	Band Pass filter
BS	Beamsplitter
CAD	Computer Aided Design
CCLRC	Council for the Central Laboratory of the Research Councils
CEA	Combined Error Angle
CMM	Coordinate Measurement Machine
CTE	Coefficient of Thermal Expansion
<i>d.c.</i>	Direct Current
DRS	Disturbance Reduction System
EA	Error Angle
EM	Engineering Model
EOM	Electro-Optic Modulator
ESA	European Space Agency
FFT	Fast Fourier Transform
FIOS	Fibre Injector Optical Subassembly
FOV	Field Of View
GPIB	General Purpose Instrumentation Bus
HF	High Frequency
HP	High Pass filter
IGR	Institute for Gravitational Research
LCA	LTP Core Assembly
LCGT	Large-scale Cryogenic Gravitational wave Telescope
LF	Low Frequency
LIGO	Laser Interferometer Gravitational wave Observatory

Acronym	Definition
LISA	Laser Interferometer Space Antenna
LP	Low Pass filter
LPF	LISA Pathfinder
LTP	LISA Technology Package
$M_{\odot}$	Solar Mass
NA	Numerical Aperture
NASA	National Aeronautics and Space Administration
Nd:YAG	Neodymium-doped Yttrium Aluminium Garnet
OB	Optical Bench
OMS	Optical Metrology Subsystem
PBS	Polarising Beamsplitter Cube
PC	Personal computer
PD	Photodiode
PFM	Proto-Flight Model
PMS	Phase Measurement System
POB	Prototype Optical Bench
ppm	parts per million
PSD	Power Spectral Density
QPD	Quadrant Photodiode
RAL	Rutherford Appleton Laboratory
<i>rf</i>	Radio Frequency
SMART	Small Missions for Advanced Research of Technology
ST-7	Space Technology 7
TNO	Netherlands Institute for Applied Geoscience

# Chapter 1

## Gravitational waves and detectors

### 1.1 The origin of gravitational waves

General relativity predicts the existence of gravitational radiation [3] and that it manifests itself as a wave-like distortion of spacetime. It also restricts the number and type of polarisation states of gravitational radiation and shows that radiation propagates at the speed of light. Hermann Bondi provided a rigorous proof [4] that gravitational radiation is a physically observable phenomenon: that gravitational waves carry energy.

This deformation of spacetime can be described by the Einstein curvature tensor  $\mathbf{G}$ , and the source by the stress energy tensor  $\mathbf{T}$ . These are related as

$$\mathbf{T} = \frac{c^4}{8\pi G} \mathbf{G}, \quad (1.1)$$

where the coupling constant contains the speed of light,  $c$ , and the Gravitational constant  $G$ . From the large coupling constant in equation 1.1 we can

deduce that spacetime is a very stiff elastic medium. Waves travelling through the fabric of spacetime will be small in amplitude with high energy density, so even when dealing with large amounts of energy from violent astrophysical events the observable effects at a distance will be small.

The constraints imposed by mass having a single sign and the conservation of momentum result in gravitational radiation being quadrupole in nature, with monopole and dipole radiation being forbidden. The spherically symmetric collapse of a star would therefore not create gravitational waves, whereas a binary system will radiate gravitational waves.

The quadrupole nature of gravitational radiation, coupled with its very weak interaction with matter, imply that a source of gravitational radiation large enough to be detected would have to come from fast, coherent motion of large amounts of matter. This denies us the opportunity of performing experiments using laboratory manufactured gravitational waves [5] and so instead we have to look to nature to provide us with sources of gravitational radiation. We find that there are many possible astrophysical sources such as supernovae, pulsars, binary stars and the Big Bang. We also find that the radiation from even these enormously energy rich sources is challengingly difficult to detect. When these signals are detected, however, they will provide astrophysical data of a kind that has never been seen before, as gravitational waves pass almost unhindered through matter in contrast to other forms of radiation currently observed.

General relativity, unlike classical electromagnetism, is non-linear. This causes problems when trying to resolve the curvature of spacetime into separate components, forcing us to adopt an assumption that is not rigorously correct, *i.e.* that we can apply the principle of superposition to gravitational waves. Far from the sources of strong gravitational radiation we can consider gravitational

waves to be superimposed as plane waves on a locally flat background. Once we have made this approximation, we can then solve Einstein's equations for weak fields and derive a wave solution. This leads us to the two possible polarisation states for gravitational waves,  $h_+$  and  $h_\times$ .

When a gravitational wave passes through a region its effect is to change the curvature of the spacetime within. If this region contains free masses then the effect on the masses as seen by an observer will be a change in the separation of the masses that depends on the amplitude and polarisation of the wave (see Figure 1.1). The effect of a gravitational wave passing through a ring of free test particles will be that the ring is compressed in one axis whilst being elongated in a perpendicular axis when the wave has a phase of  $\pi/2$ , then return to its undisturbed state when the phase of the wave is  $\pi$ . The previously elongated axis then becomes compressed and *vice versa* at phase  $3\pi/2$ . Finally the ring returns to its undisturbed state when the wave reaches a phase of  $2\pi$ . In attempting to detect the passage of such a wave we can recognise that this perpendicularly opposite motion lends itself ideally to the use of a Michelson interferometer [6]. The optics involved have to be isolated in order to act as independent 'free' masses. This is the basic idea used in ground based laser interferometric gravitational wave detectors.

## 1.2 Sources of gravitational waves

There are many potential sources of gravitational radiation that could produce radiation of a detectable level with suitable frequency. The theoretical analysis of these sources informs the design of detectors and also the methods used to search for gravitational wave signals in the data. Perhaps the most interesting gravitational radiation that will be detected is that from sources which have

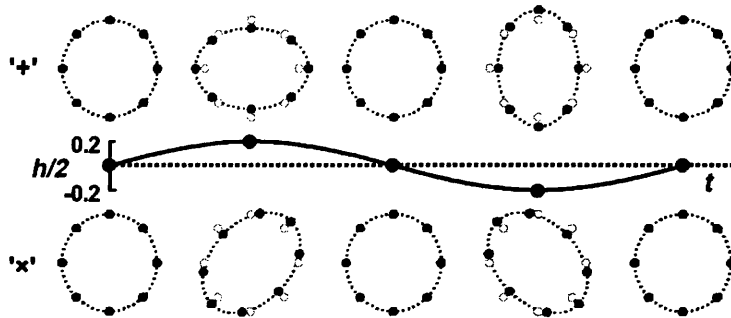


Figure 1.1: *Illustration showing the two independent linear polarisations of a gravitational wave acting on a ring of free particles. Wave has amplitude 0.2 (Source [1]).*

not yet been anticipated. This kind of a discovery could open whole new debates as to the nature of the universe.

Some postulated sources of measurable gravitational radiation are:

- Spinning neutron stars whose centre of mass does not lie on their rotation axis (possibly due to small irregularities on the surface) will emit gravitational waves. The system would emit gravitational radiation as twice the rotation frequency due to the mass distribution having a period every half rotation cycle and this could be well into the detection band for ground-based (higher frequency) detectors. Furthermore, a neutron star acting in this way could provide a long lived signal if it were accreting material from a neighbour and replenishing the energy it was losing by gravitational radiation.
- Binary star systems will emit gravitational radiation similarly to spinning neutron stars. In a binary system the orbital motion produces gravitational waves which carry energy away from the system. This results in the orbit decreasing and eventually the inspiralling trajectory will lead to the two objects merging. This sequence of events produces a distinct gravitational wave

signature: a chirp signal. The periodic signal will increase in amplitude and frequency until the final merger. These signals will sweep from low frequency through all the detector bands and will provide a good source of astronomy.

- Type II supernovae are the violent collapse of a massive stellar core to form a neutron star or a black hole. If the collapse is not spherically symmetric a burst of gravitational radiation will be emitted. The exact waveform resulting from such an occurrence is very difficult to predict and so detection would allow the reverse to occur: the observation could assist the efforts to model such an event.

- The observation of a gravitational wave stochastic background would provide interesting information. One possible source of a stochastic background is the gravitational waves produced from  $\sim 10^{-24}$  s after the Big Bang. Stochastic background measurements could be made by both ground and space based (lower frequency) detectors [7].

- Black holes of mass  $\sim 10 M_{\odot}$  are expected to be found in binary systems in similar numbers to neutron star binaries. Due to the greater mass (and therefore energy) associated with these black holes they will be visible from further distances. Gravitational waves from binaries containing black holes are prime candidates for the first ground-based detection and may even be detected by the first generation of detectors.

- Supermassive black holes (having mass  $> 10^6 M_{\odot}$ ) are a very exciting source for space-based detectors. We do not yet know how they are formed but we do know they exist. These black holes can emit gravitational radiation when linked as a binary, similarly to the lower mass black holes, but with lower frequency and emitting radiation of much larger amplitude. If these sources exist they will be seen by LISA. Supermassive black holes can also

emit gravitational waves when capturing smaller compact bodies.

A review of gravitational wave sources potentially detectable with first and second generation detectors can be found in [5].

### 1.3 Gravitational wave detection

The enormity of the task of measuring gravitational waves becomes apparent when we realise that we are trying to measure strain amplitudes of the order  $10^{-21}$ . For an interferometer with 1 km long arms, this translates to a movement of approximately  $10^{-18}$  m. The tiny magnitude of this movement tells us that any noise included in our measurement will have to be very low to avoid completely washing out the signal. Noise sources associated with gravitational wave detectors include thermal noise, seismic noise, shot noise and laser (intensity and frequency) noise [8].

The search for gravitational waves is ongoing and direct detection is yet to be accomplished. In 1975 Hulse and Taylor reported on the discovery of a binary system containing a pulsar (PSR 1913+16) [9] (this was also followed up in the 1976 publication [10]). They pointed to the opportunity of measuring the rate of loss of orbital energy to test relativistic gravitation theories. This binary system was studied over many years, culminating in the publications [11, 12]. This work indirectly shows evidence of gravitational wave emission and is in excellent agreement with general relativity. Hulse and Taylor jointly received the Nobel Prize for Physics in 1993 for *‘the discovery of a new type of pulsar, a discovery that has opened up new possibilities for the study of gravitation’*.

### 1.3.1 Ground based detectors

Despite the considerable challenges of direct gravitational wave detection many first generation ground based detectors are currently on-line, with the second generation in the advanced planning stages.

#### Resonant bar detectors

The field of experimental gravitational wave detection began in earnest with a resonant bar detector antenna that was planned and built by Joseph Weber [13, 14]. The basic design included a large cylindrical aluminium bar with strain gauges used to monitor the amplitude of the resonant modes. The principle was that when a gravitational wave of frequency close to the longitudinal resonant frequency of the bar passes through the detector, the bar will become excited. The change in amplitude of the resonant mode,  $\Delta L$  is proportional to the dimensionless wave amplitude  $h \approx \Delta L/L$  where  $L$  is the length of the bar. The sensitive strain gauge is then used to measure the amplitude of the resonant mode.

This technique is still used today in more advanced bar detectors:

- The Allegro detector is a 2300 kg aluminium bar located in Louisiana, USA and has been operating since 1991. It is cooled to 4.2 K to reduce the effects of thermal noise due to random vibration of atoms.
- The Auriga detector is a 2230 kg aluminium bar located in Padova, Italy and has been operating since 1997. It is cooled to 200 mK.
- The Explorer detector is a 2270 kg aluminium bar located at CERN in Geneva, Switzerland and it has been operating since 1990. It is cooled to

2.6 K.

- The Nautilus detector is a 2260 kg aluminium bar located in Rome, Italy and it has been operating since 1995. It is cooled to 130 mK.
- The Niobe detector is a 1500 kg niobium bar located in Perth, Australia and has been operating since 1993. It is cooled to 5K. Niobium has been used for its high  $Q$  factor, which gives a longer ring down and enables increased signal to noise measurements.
- The MiniGRAIL detector is a 1150 kg CuAl(6%) sphere [15] being commissioned in the Netherlands. Spherical detectors are being investigated as they are omnidirectional, whereas the bar detectors are limited in this respect. This detector will be cooled to 20 mK.
- The Mario Schenberg detector is a 1150 kg CuAl(6%) sphere [16] being commissioned in Brazil. This detector will be cooled to 20 mK.

A review of the bar detector status in 2002 can be found in [17].

### Laser interferometric detectors

Resonant bar detectors are limited to monitoring very narrow frequency bands, dictated by their physical dimensions. This has led to the development of a different style of gravitational wave detector in which the physical material between the end faces of the bar detector is removed and interferometry is used as the readout technique. This has the advantage of allowing broad frequency ranges to be observed and also allowing much longer length antennae.

The ground-based network of laser interferometric gravitational wave detectors

is now well established and scientific results are already being harvested [18, 19, 20, 21, 22, 23, 24, 25, 26, 27, 28, 29, 30]. A thorough review of the ground based detectors in 2000 can be found in [8].

The sensitivity of detectors is usually stated in terms of  $h$ , the dimensionless strain amplitude of a gravitational wave. A strain in space caused by the passing of a gravitational wave of amplitude  $h$  would have the effect of changing the distance between two free masses. This occurs as

$$\frac{\Delta L}{L} = \frac{h}{2}, \quad (1.2)$$

where the masses are separated by a distance  $L$  and  $\Delta L$  is the induced change in separation. Thus we can see that increasing the armlength of the detector improves the sensitivity although it increases the resources needed to build a detector.

The current ground based laser interferometric detectors are:

- The Laser Interferometer Gravitational wave Observatory (LIGO) project consists of three interferometers: a 4 km and a 2 km armlength detector in Hanford, Washington and a 4 km armlength detector in Livingston, Louisiana. All three interferometers have Fabry-Perot cavities in the arms and power recycling schemes to increase light storage time (and hence phase shift due to gravitational wave interference). This detector network is currently the most sensitive gravitational wave detector in operation. The best reported strain sensitivity to date was seen during the second science run (S2) and was  $3 \times 10^{-22}/\sqrt{\text{Hz}}$  at 200 Hz [30]. The next generation of LIGO, Advanced LIGO, is already planned and will improve on LIGO's performance by an order of magnitude in strain sensitivity which should be enough to start making detections on reasonable time scales. One of the major upgrades to achieve this improvement will be the introduction of advanced suspension systems [31],

as demonstrated by GEO 600. Advanced LIGO should have a best sensitivity of  $\sim 2 \times 10^{-24}/\sqrt{\text{Hz}}$  at around 300 Hz [32].

- The VIRGO interferometer is a French-Italian collaboration based situated near Pisa, Italy. It is a 3 km armlength detector with power recycling and Fabry-Perot arm cavities. Commissioning is still in progress and the latest sensitivity curves show a best strain performance of  $\sim 10^{-20}/\sqrt{\text{Hz}}$  at 300 Hz [33]. The most notable distinction between VIRGO and the other detectors is the isolation system used to ensure the optical components act as ‘free’ test masses. The VIRGO detector uses an isolation system called the ‘*Superattenuator*’ designed to provide a factor of  $10^{12}$  reduction of seismic noise at a few Hz to enable to the detector to measure down these low frequencies.

- GEO 600 is a British-German collaboration located near Hannover, Germany. It has a 600 m armlength, although this is effectively doubled by having folded arms, with both signal and power recycling implemented. The philosophy of GEO 600 is to use advanced technology to compensate for the smaller scale arms in order to obtain sensitivities roughly comparable to the first generation longer baseline detectors over part of the frequency spectrum. This results in technology demonstration that can (and will) be implemented in the next generation of ground-based laser interferometric gravitational wave detectors. This includes the use of advanced suspension systems which form the baseline for Advanced LIGO. GEO 600 has a very high duty cycle and latest published strain sensitivity of  $\sim 3 \times 10^{-21}/\sqrt{\text{Hz}}$  at 1 kHz [25].

- TAMA300 is a Japanese detector located in Tokyo with 300 m armlength. It has Fabry-Perot cavities in the arms and the latest data taking run (DT9) produced a maximum strain sensitivity of  $2 \times 10^{-21}/\sqrt{\text{Hz}}$  at 1 kHz [34]. There are plans to build a 3 km armlength detector in Japan that will be cooled to cryogenic temperatures to reduce thermal noise, the Large-Scale Cryogenic

Gravitational wave Telescope (LIGO).

- AIGO is currently an 80 m test bed located near Perth, Australia. It is being used to investigate high power lasers for use in advanced laser interferometer gravitational wave detectors and Euler spring based suspensions [35]. There are plans to turn the facility into a  $\sim$  km armlength facility.

Having a global network of detectors will be essential when gravitational waves are detected on Earth to provide coincidence measurements and to infer the orientation of the source.

### 1.3.2 Detectors in space

Ground based detectors are prevented from measuring below approximately 10 Hz due to gravity gradient noise. This is the disturbance of the test masses by changes in the local mass distribution, *e.g.* seismic waves, turbulence in the atmosphere. This is a result of the inverse square law of gravitational attraction. Even birds flying past 100 m away will cause the test mass to move more than a gravitational wave passing through the system. It is possible to reduce these effects to some extent by building a detector in a gravitationally quieter environment (underground, for example), but only small improvements in the detector frequency range can be gained. These kind of effects are limited to low frequencies, however, as local mass distributions on Earth tend to be stable at frequencies greater than a few Hertz.

This noise source is a frustration for gravitational wave detection as there are many expected sources at lower frequencies, as indicated in Section 1.2. Thus to conduct gravitational wave detection and astronomy at low frequencies we move to a gravitationally quiet environment: space.

LISA (Laser Interferometer Space Antenna) [36] is the planned space-based gravitational wave detector, a triangular spaceborne detector with five million kilometer long arms, due for launch around 2015. The primary objective of LISA is to observe gravitational waves at low frequency ( $10^{-4}$  to  $10^{-1}$  Hz). A gravitational wave acting on LISA will change the length of one  $5 \times 10^9$  m arm relative to the other. This fluctuation will be measured with sub-Ångstrom accuracy allowing gravitational wave strains ( $\Delta l/l$ ) even of the order  $10^{-23}$  to be detected over one year with a signal to noise ratio of around five [37].

By looking at this frequency range LISA has the advantage of being guaranteed to detect gravitational radiation as there are abundant sources within the expected sensitivity range, such as massive black holes and galactic binaries. Space-based and ground-based detectors will be looking at different frequency regions allowing entirely complementary observations to be made (see Figure 1.2).

## Gravitational Wave Spectrum

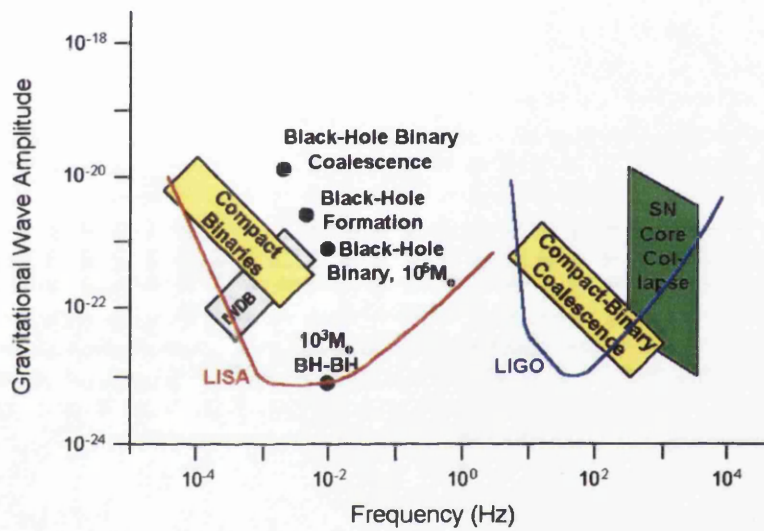


Figure 1.2: Graph showing how space based and ground based observations will complement each other by covering a different frequency range with similar sensitivities (Source [1]).

## Chapter 2

# Testing critical technologies for LISA

LISA is a large scale joint ESA/NASA mission which will combine many technologies, of which the concept of ‘drag free’ test masses (effectively the end mirrors of the interferometer) cannot be adequately tested in the 1g environment of Earth. To address this, and other critical technologies, a smaller scale mission is planned for launch in 2009. The mission is called LISA Pathfinder (previously called SMART-2) and is an intermediate step to reduce the technological risks faced in the LISA mission. One of the experiments aboard LISA Pathfinder is the LISA Technology Package [38] and it aims to demonstrate the thrusters, drag-free test mass concept [39] and ultra-stable interferometry to levels similar to those required for LISA. The noise sources and couplings will be characterised to give confidence that the LISA performance can be achieved. LISA Pathfinder will also contain NASA’s LISA technology demonstrator, the ST-7 experiment [40], which has recently been de-scoped.

In LISA gravitational waves will change the separation of inertial test masses,

the vector describing the change in separation depending on the amplitude, origin and polarisation of the wave. The movement of the test masses relative to each other will be measured and information about the gravitational wave deduced. Thus it is essential that we can trust that when no gravitational wave passes through the system no unexpected movement of the test mass occurs, as non-inertial movements of test masses can produce similar effects to those being sought.

The aim of the LTP experiment is to show the quality of drag-free performance to within an order of magnitude of LISA requirement, but to characterise noise sources to LISA levels.

LTP will consist of two test masses (one surface of each acting as a mirror in an interferometer) with an optical bench between them housed in a single spacecraft. Laser light will be coupled onto the optical bench and heterodyne interferometry used to measure the movement of the masses relative to the optical bench and to each other. The interferometer outputs will be read out by a phasemeter which provides low noise measurements of test mass positions and angles. These signals can also be used as inputs to the controllers.

Using the information gained from LTP, LISA will be constructed with confidence that the behaviour and performance of the test masses (which are optical components in the interferometer and the fundamental inertial reference) is well understood.

To obtain data of sufficiently high sensitivity from the LTP measurements the inherent noise within the interferometer has to be less than  $10 \text{ pm}/\sqrt{\text{Hz}}$  over the frequency range of interest (3 mHz to 30 mHz, relaxing as  $1/f^2$  at lower frequencies). The optical bench must also remain structurally sound and well aligned after the violent disturbance experienced during launch into orbit.

## 2.1 LTP interferometry

The baseline for the LTP is a non-polarising heterodyne Mach-Zender interferometer [41, 42]. This has been selected in favour of polarising interferometers as there were concerns that polarisation leakage could lead to cross-coupling between beam paths. A consequence of this is that the beams can no longer be perpendicularly incident on the test masses.

The concept of heterodyne interferometry is shown in Figure 2.1. The laser is split at point A into two equal beams that pass through two acousto-optic modulators (AOMs). The AOMs are driven at two frequencies separated by the heterodyne frequency,  $f_{\text{het}}$ , which is of order 1 kHz. The AOMs are not situated on the stable interferometer baseplate due to thermal considerations.

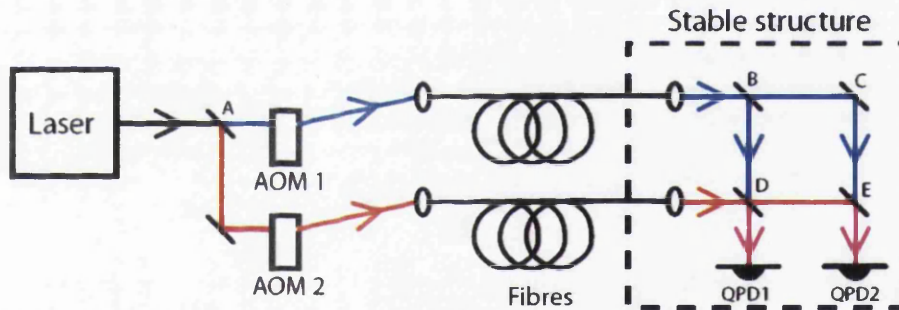


Figure 2.1: Schematic showing the principle of the heterodyne interferometry.

The beams pass through fibres (this is not a requirement of the interferometry but a practical means of coupling light onto a baseplate) and are recombined at point D. Half of the light travels a different route and is recombined at point E. The heterodyne signal from quadrant photodiode 1 (QPD1) is sent to the phase measurement system (PMS), as is the heterodyne signal from QPD2.

The phase at the QPDs depends on the difference in path length between the

blue and red beams. This includes the path length variations introduced by differential temperature changes in the fibres (the main source of path length noise in this system). Thus the phase at the QPDs is given by

$$\begin{aligned}\phi_{QPD1} &= (A \rightarrow D)_{blue} - (A \rightarrow D)_{red} \\ &= (A \rightarrow B)_{blue} + (B \rightarrow D)_{blue} - (A \rightarrow D)_{red},\end{aligned}\quad (2.1)$$

$$\begin{aligned}\phi_{QPD2} &= (A \rightarrow E)_{blue} - (A \rightarrow E)_{red} \\ &= (A \rightarrow B)_{blue} + (B \rightarrow E)_{blue} - (A \rightarrow D)_{red} - \\ &\quad - (D \rightarrow E)_{red}.\end{aligned}\quad (2.2)$$

So combining Equations 2.1 and 2.2

$$\begin{aligned}\implies \phi_{QPD2} &= \phi_{QPD1} - (B \rightarrow D)_{blue} + \\ &\quad + (B \rightarrow E)_{blue} - (D \rightarrow E)_{red},\end{aligned}\quad (2.3)$$

$$\implies \phi_{QPD1} + [(B \rightarrow E) \text{ via } C] = \phi_{QPD2} + [(B \rightarrow E) \text{ via } D]. \quad (2.4)$$

*i.e.* the phase at QPD2 is related to the phase at QPD1 by the difference in path lengths for the two different routes from point B to E: path length variations prior to the initial beamsplitters on the ultra-stable substrate should cancel out.

Thus the important measurement is the *phase change* of one interferometer output compared to the other as this is due to the path length variations on the optical bench. If we include the drag free test masses as components in the interferometer then the phase change becomes a measure of their motion.

There are four interferometers (used to measure the performance of the drag-free motion along the beam axis and also the alignment of the two test masses) in the LTP set-up:

- a reference interferometer (shown in Figure 2.2),
- an interferometer with large path length difference that measures the laser frequency noise as shown in Figure 2.3 (see Section 2.2.2),
- an interferometer called  $x_1$  that measures the position of one test mass in relation to the interferometer baseplate (shown in Figure 2.4) and
- an interferometer called  $x_1 - x_2$  that measures the distance between the two test masses (shown in Figure 2.5).

The complete LTP optical layout is shown in Figure 2.6. Much of the optical modeling for LTP has been carried out using OptoCad, a program written by Roland Schilling, as in these Figures. The optical layout was initially designed by Gerhard Heinzel and the design was further advanced by Felipe Guzmán Cervantes. The distance between the test masses is of order 300 mm and this must be monitored by the interferometer to  $10 \text{ pm}/\sqrt{\text{Hz}}$ , over a range of many microns. The light travels different distances in the two fibres to facilitate beam path length matching at the interference points.

The optical bench is located between the two test mass enclosures, at the heart of the LTP core assembly. The interferometer consists of a Zerodur® baseplate of dimensions  $212 \times 200 \times 45 \text{ mm}$  with 22 reflecting optical components hydroxide-catalysis bonded [43, 44] to one of the  $212 \times 200 \text{ mm}$  faces. Zerodur® is a glass ceramic chosen mainly for its ultra-low thermal coefficient of expansion [45]. The optical components are to be made of fused silica due to its excellent optical properties at 1064 nm. The light is coupled onto the optical bench using quasi-monolithic fibre injectors, custom designed and built for the application.

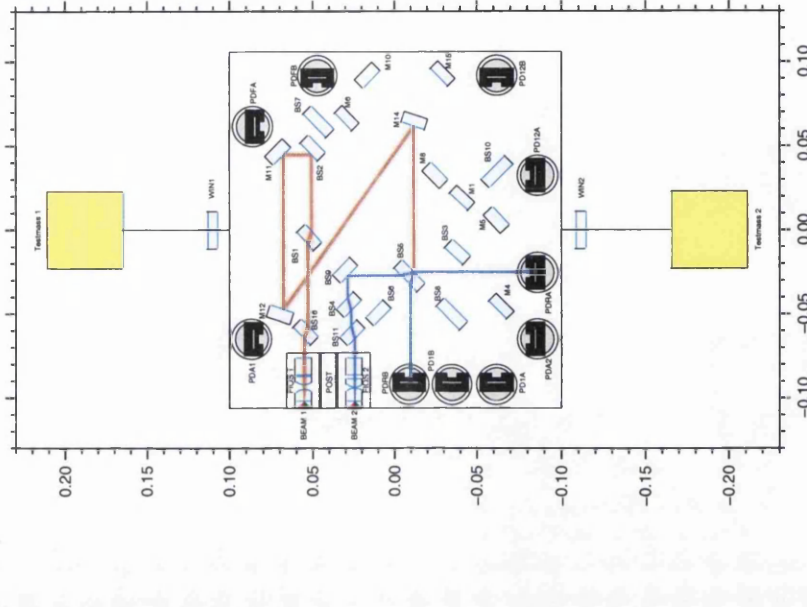


Figure 2.2: *Optical model of the LTP reference interferometer.*

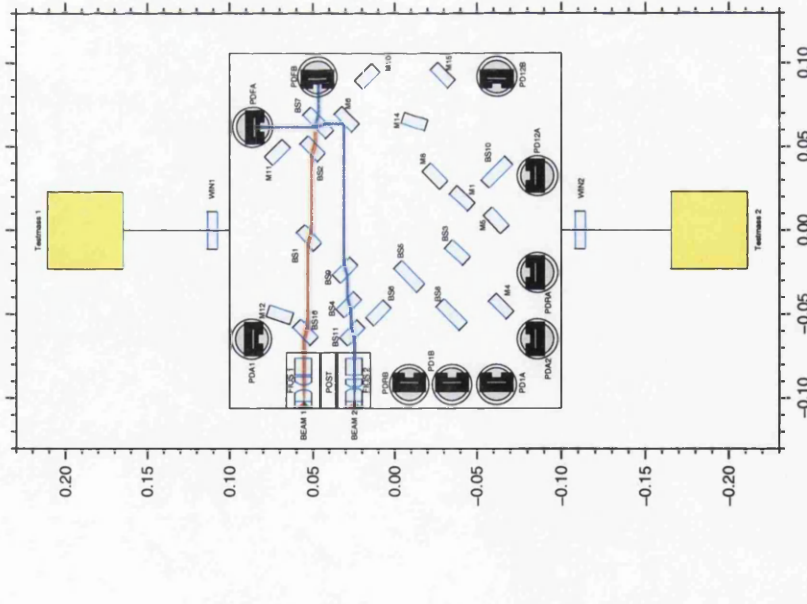


Figure 2.3: *Optical model of the LTP frequency noise interferometer.*

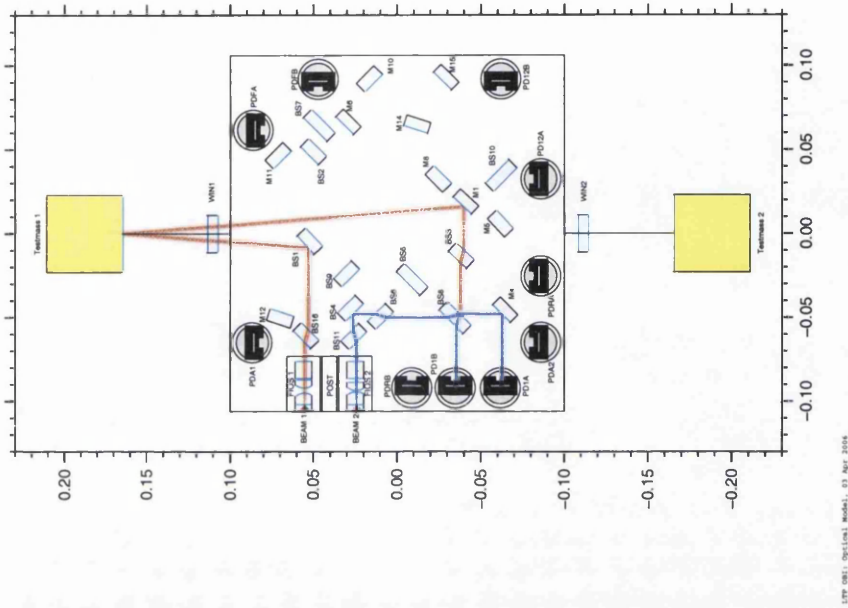


Figure 2.4: Optical model of the LTP  $x_1$  interferometer.

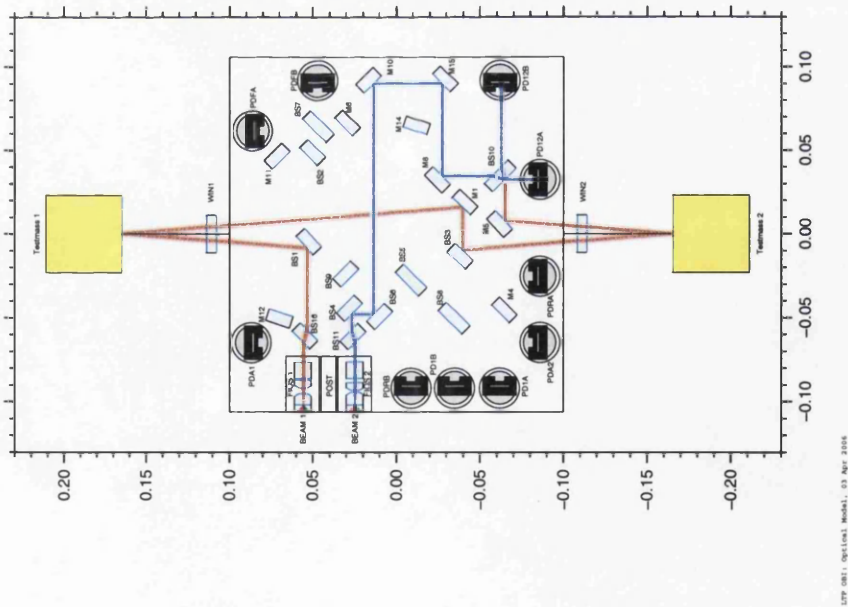
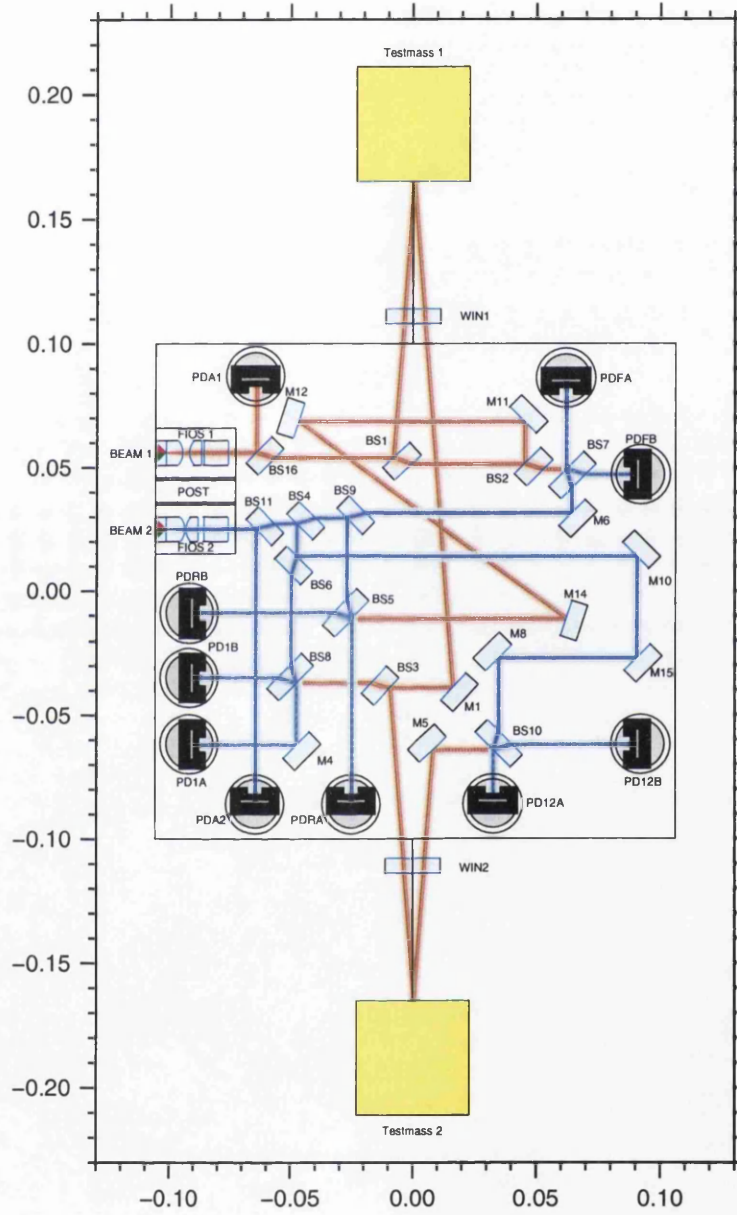


Figure 2.5: Optical model of the LTP  $x_1 - x_2$  interferometer.



Felipe Guzmán Cervantes, 23 Mar 2006

Figure 2.6: *Optical model of the LTP optical bench interferometer. Dimensions are in metres.*

## 2.2 LTP noise sources

The noise sources described in this Section are for well aligned interferometers. A discussion of alignment tolerances for similar interferometry is given in Section 3.1.5. Each interferometer noise source for LTP has to be kept a factor of 10 below the measurement goal of  $10 \text{ pm}/\sqrt{\text{Hz}}$ , *i.e.* each noise source is allocated a maximum noise budget of  $1 \text{ pm}/\sqrt{\text{Hz}}$  at 3 mHz. This is to avoid any correlated noise sources adding linearly and generating more noise than expected.

### 2.2.1 Laser power fluctuations

There are two frequency regimes where laser power noise matters for the LTP interferometer: adding noise into the phase measurement at the heterodyne frequency and adding radiation pressure noise at the test mass in the measurement band.

At the heterodyne frequency the laser power noise can couple into the measurement by producing a signal of randomly varying phase at the heterodyne frequency. The signal adds to the ‘real’ heterodyne signal producing apparent fluctuations in its phase.

If we consider a fractional variation in laser power,  $\delta P/P$ , where  $\delta P$  is the laser power variation and  $C \cdot P$  is the signal size at the heterodyne frequency (with  $C$  the contrast of the interference), then we can relate this to the maximum allowable noise contribution from this source:  $1 \text{ pm}/\sqrt{\text{Hz}}$ , or  $2\pi \times 10^{-6}$  radians in

terms of relative phase of heterodyne signal as (taking the worst case  $C = 80\%$ ):

$$\begin{aligned} \frac{\delta P}{C P} &\leq 2\pi \times 10^{-6} / \sqrt{\text{Hz}} \\ \Rightarrow \frac{\delta P}{P} &\lesssim 5 \times 10^{-6} / \sqrt{\text{Hz}} . \end{aligned}$$

This level of power variations is not expected to be a difficult requirement at the heterodyne frequency [46].

In the measurement band, where we are concerned about radiation pressure effects on the test masses, the laser power noise,  $\delta P$ , can be related to the induced displacement fluctuations,  $\delta x$ , by

$$\delta x = \frac{2 \delta P}{m c \omega^2} ,$$

where  $m$  is the mass of the test mass,  $c$  is the speed of light and  $\omega = 2\pi f$  and  $f$  is the frequency of the measurement.

The test masses will be cubes of side  $\sim 4.5$  cm and made of a gold/platinum alloy, having a density  $\sim 2 \times 10^4$  kg/m<sup>3</sup>. Thus  $m \approx 2$  kg.

Again looking at the fractional power variation and a maximum displacement fluctuation of 1 pm/ $\sqrt{\text{Hz}}$ :

$$\begin{aligned} \frac{\delta P}{P} &< \frac{m c \omega^2}{2P} \delta x \\ &\approx 3 \times 10^{-5} / \sqrt{\text{Hz}} . \end{aligned}$$

at 10 mHz and where  $P$  has been taken to be 1 mW, which is representative of the expected light power in the LTP interferometer arms.

Again this level of laser power noise is not expected, but the fibres may introduce additional power fluctuations to the beams on the optical bench. The laser power immediately after each fibre on the optical bench will be measured (using the pick-off beamsplitters labeled BS11 and BS16 in Figure 2.6) using

single element photodiodes. These signals can be used as part of a feedback loop to provide an error signal to the AOM drive signals to reduce the laser power noise.

### 2.2.2 Laser frequency noise

If there is a difference in the path lengths of an interferometer then it will be sensitive to laser frequency noise. In the case of LTP, even if the interferometers were constructed with equal paths optical components (the test masses) are required to move during some modes of operation. This results in the path lengths becoming unbalanced and laser frequency noise coupling into the measurement.

Laser frequency noise ( $\delta\nu$ ) couples to apparent path length change ( $\delta x$ ) as

$$\delta x = \Delta x \frac{\delta\nu}{\nu}, \quad (2.5)$$

where  $\nu$  is the laser frequency and  $\Delta x$  is the path length difference between the different arms of the interferometer. Taking the path length difference to be 1 mm (this is a reasonable manufacturing tolerance) and the noise contribution budget of  $1 \text{ pm}\sqrt{\text{Hz}}$  gives a requirement that the laser frequency noise is less than  $\sim 3 \times 10^5 \text{ Hz}/\sqrt{\text{Hz}}$ . This is around two orders of magnitude lower than expected for the LTP [46] laser, so some strategy is required to reduce its effect.

A common method of reducing laser frequency noise is to lock the laser frequency to a stable reference (usually a stable optical cavity or a molecular transition, *e.g.* an iodine cell). While either of these solutions could in principle be applied to LTP they would add mass and complexity and are therefore not attractive. For LTP the baseline solution is to have an additional interferometer to measure the laser frequency fluctuations. This interferometer

purposely has a large path length difference ( $\sim 40$  cm) to maximise the coupling of laser frequency noise. The measured signal can then be used either as part of a stabilisation loop or to correct the data *post-factum*.

### 2.2.3 Path length changes

There are two ways in which the optical bench can generate noise sources: physical path length changes between reflective components and changes in optical path length through transmissive components. Both of these are temperature driven. The expected temperature fluctuations experienced by the optical bench at the mechanical interfaces are  $< 10^{-4} \text{ K}/\sqrt{\text{Hz}}$ , from 1-30-mHz ([2], requirement OMS-7.2.5-3).

#### Physical path length changes

The physical expansion of the Zerodur® baseplate depends on the temperature fluctuation noise,  $\delta T$ , and the thermal coefficient of expansion,  $\alpha$  (which is  $2 \times 10^{-8} / \text{K}$  for expansion class 0 Zerodur® [45]). How this effects the apparent path length depends on the separation of the components. Taking the worst case situation (the longest path in the interferometer) the relevant path is from the reference signal recombination beamsplitter to the  $x_1 - x_2$  recombination beamsplitter. This beam path includes beams that reflect off the test masses, but even though the test masses are not attached to the baseplate, the test mass housings are attached to the baseplate *via* Zerodur® side-slabs and the test masses are relatively stationary with respect to them, meaning this path length can be considered the most prone to expansion of the Zerodur® baseplate.

The path length from BS5 to BS10 is (using the labeling of Figure 2.6):

BS5 → M14 (12 cm)  
 → M12 (18.5 cm)  
 → M11 (7 cm)  
 → BS2 (2 cm)  
 → BS1 (3 cm)  
 → TM1 (11 cm)  
 → BS3 (17 cm)  
 → M4 (2 cm)  
 → TM2 (17 cm)  
 → M5 (12 cm)  
 → BS10 (3 cm) .

This gives a total path length,  $l$ , of  $\sim 1.05$  m. From this we can calculate a worst case apparent path length change of

$$\begin{aligned}\delta l &= \alpha \times l \times \delta T \\ &= 2.1 \times 10^{-12} \text{ m} .\end{aligned}$$

This is a factor of  $\sim 2$  above the individual noise source budget, but this is very much a worst case analysis for the path length change due to the Zerodur® baseplate expansion. In practice the temperature changes across the optical bench will be very uniform. This will result in the observed effect being greatly reduced due to common mode expansion of the individual interferometer arms.

### Optical path length changes

The optical thickness of the beamsplitters varies with temperature due to the expansion of the material and change in refractive index. The beamsplitters

have a thickness of 7 mm but the beams are incident on the beamsplitters at  $45^\circ$  and consequently traverse the beamsplitter at  $\sim 29^\circ$ . This results in a beam path length in the beamsplitters of 8 mm. The maximum number of beamsplitters passed by any beam is three (in both of the frequency noise paths), giving a total optical path in the beamsplitter material,  $l$ , of 24 mm.

The beamsplitters will be made of fused silica which has a refractive index ( $n$ ) of 1.45, a coefficient of thermal expansion (CTE) of around  $0.51 \times 10^{-6}/\text{K}$  and a change of refractive index with temperature ( $dn/dT$ ) of  $\sim 9.7 \times 10^{-6}/\text{K}$ .

Knowing these values we can calculate the apparent path length variation due to this effect:

$$\begin{aligned} \delta l &= \left[ n \times \text{CTE} + \frac{dn}{dT} \right] \times l \times \delta T \\ &= 25 \times 10^{-12} \text{ m}/\sqrt{\text{Hz}} . \end{aligned}$$

This is significantly above the noise budget of  $1 \text{ pm}/\sqrt{\text{Hz}}$  but this is an extreme worst case calculation. Each interferometer has been designed such that both arms pass through the same number of beamsplitters, meaning that most of this noise is expected to be common to both arms and cancel out. The ground based tests that have been carried out endorse this (one of which is described in Chapter 4).

#### 2.2.4 Phase information lost at quadrant photodiodes

Quadrant photodiodes are needed on the LTP to give angular information of test mass position. These quadrant photodiodes have four quadrants separated by  $\sim 45 \mu\text{m}$  inactive strips. There are two ways in which light can be lost at the photodiodes: beam clipping at the extremities of the photodiodes and light lost at the inactive photodiode slits.

Beam clipping will be avoided by using photodiodes with suitably large active area compared to beam size but some light will obviously be lost at the inactive strips.

For the ideal case of overlapping, colinear, interfering beams with flat wavefronts, the information lost at the photodiode slits would not alter the phase measurements. All the interferometer arms have different lengths but use light from the same sources. It is not possible to match the wavefronts of all the beams at every photodiode as the only variables are the sizes and curvatures of the beams at the two fibre injectors and the distance from the fibre injectors. Thus, the wavefronts will have some curvature and there will be some mismatch of curvature at the photodiodes.

Beam jitter from the fibre injectors will be minimal and the photodiodes will be located on the optical bench baseplate, reducing the effects of beam jitter coupling into the phase measurement to an insignificant level. However, in some modes of operation the test masses will be moved from their nominal positions and thus one of the wavefronts will move with respect to the photodiode slits. This effect is described in more detail in Section 4.3.4.

### 2.2.5 Stray light

Stray light is the term used to describe light arising from, for example, back reflections from nominally transmissive surfaces. These beams can potentially reach the photodiodes and contribute to the measured phase. If all the surfaces involved in directing the stray beams to the photodiode are stable with respect to the optical bench and laser frequency noise is suppressed, then they will not cause additional noise.

The concern for these beams is that they can reflect from surfaces not rigid with respect to the optical bench and then influence the phase of the measured signals, adding spurious noise. This is discussed for the LTP case in [47]. The requirement on the stray light contribution for each beam is to be attenuated to at least  $10^{-6}$  of the signal amplitude ([2] requirement OMS-4.3.3-6).

To reduce the effect of stray light, optical modeling is used to predict the source of stray beams in order to place beam blocks in appropriate places. Figure 2.7 shows the stray light beams and Figure 2.8 shows the implementation of the beam dumps. This is discussed fully in [48].

The following conditions for the stray light analysis are set:

- stray beams are generated at the reflective surfaces with 0.5% of the incident power,
- stray beams with a relative amplitude of  $10^{-6}$  and above are shown,
- the optical windows (on the test mass housing) reflect the stray beams towards the optical bench baseplate at an angle of  $5^\circ$  to the incoming beam and
- the test mass tilts have a maximum of  $\pm 2$  mrad.

### 2.2.6 Measurement noise

Spurious noise must not be added to the measured signals at the signal processing stage. The style of phasemeter chosen for LTP uses a single-bin discrete Fourier transform method [46]. This involves converting each measured heterodyne frequency into a digital signal that is used to measure both longitudinal

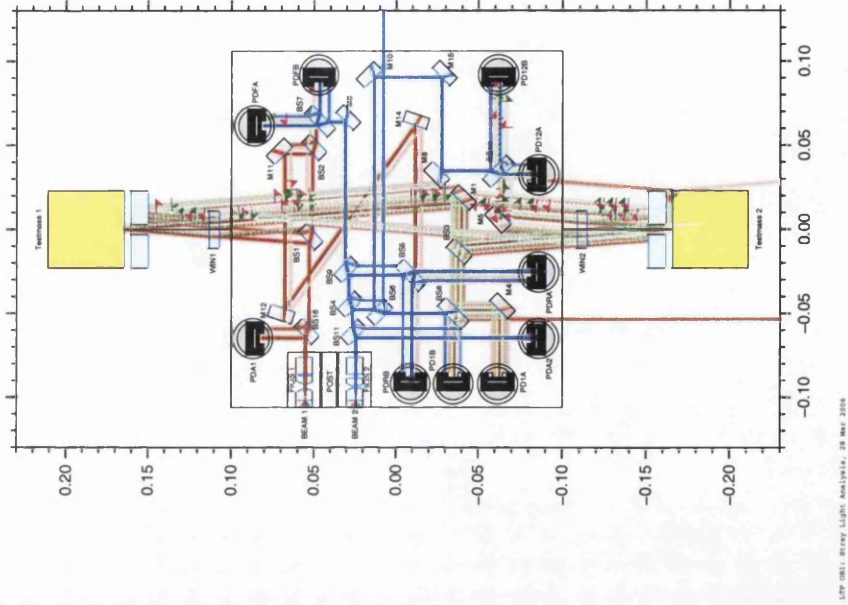


Figure 2.7: Optical model of the LTP interferometers showing all stray beams.

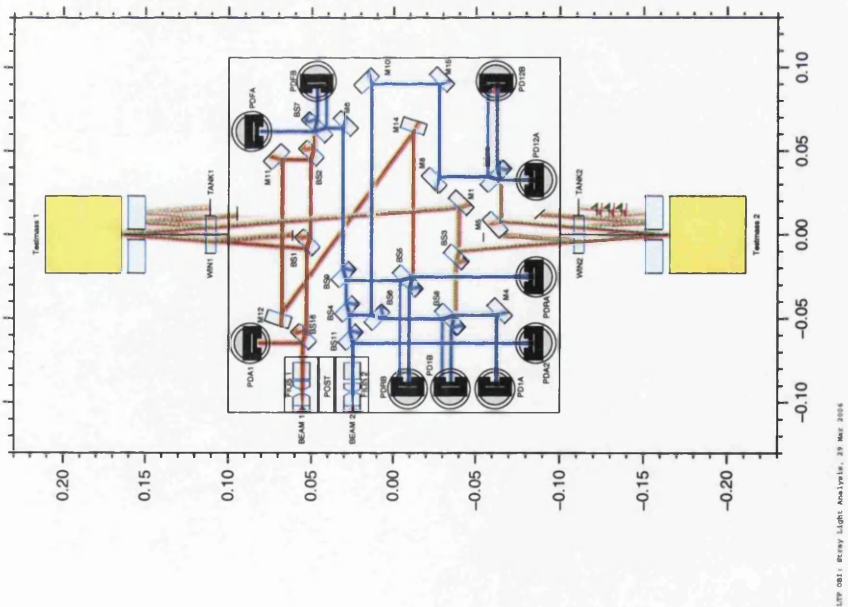


Figure 2.8: Optical model of the LTP interferometers showing the stray beam dumps.

test mass motion and angular shifts using differential wavefront sensing. These signals can be used as error signals as part of a feedback loop to stabilise the test mass position.

## **2.3 Validation of LTP style interferometry**

While the drag free test masses cannot be ground tested the interferometry can, by replacing the test masses with mirrors attached to the baseplate in the same way as the other mirrors and beamsplitters. One less interferometer is required in this case as there is no need for a measurement of two test masses' 'combined movement.'

Prototype tests have been conducted verifying the performance of LTP style interferometry and these are described in Chapters 3 and 4. This is also reported in [49].

## Chapter 3

# LISA Pathfinder prototype optical bench design and construction

LTP requires interferometry to measure the relative displacement of inertial test masses. The experimental programme described here was to design and construct a prototype optical bench and then to use heterodyne interferometry to determine its stability. The aims of this series of experiments were to develop and test the construction techniques required to build such a bench, demonstrate heterodyne interferometry at the desired sensitivity, demonstrate the required stability of the bench, and to investigate noise sources in the bench and interferometry.

## 3.1 Design of the prototype optical bench

### 3.1.1 Design considerations

The LTP measurement requirements were reviewed and an interferometer layout was devised to provide the simplest functional demonstration of the key LTP measurement principles using a representative optical bench.

This resulted in a prototype interferometer including the following features in common with the planned LTP interferometer:

- an optical bench (OB) baseplate made from material with a low coefficient of thermal expansion,
- optical components rigidly fixed to the baseplate,
- light fibre coupled onto the OB baseplate and
- heterodyne interferometry used to measure path length changes.

It differed significantly from the LTP interferometer by not having any optical components outwith the prototype OB baseplate. The aim of the LTP OB is to measure the displacement between the two test masses and also between the prototype OB and one test mass, thus the two inertial test masses are separate from the prototype OB. The prototype has no external components and the 'inertial test mass' mirrors can be considered as being replaced by mirrors on the bench itself *i.e.* it is a null test.

By having arm lengths of the order of a meter the prototype optical bench is similar LTP.

### 3.1.2 Choice of materials

#### Optical component material

The choice of optical component material is important both for mechanical stability and for the optical properties of the beamsplitters, which are the only transmissive elements in the system. One potentially significant noise source in the test interferometer is thermally driven optical path length changes in the bulk material of the beamsplitters. The combined effect of a change in temperature on the optical path length will depend on the refractive index ( $n$ ), the coefficient of thermal expansion ( $\alpha$ ) and the rate of change of refractive index with temperature ( $dn/dT$ ) of the material. We can construct a thermal coupling factor that combines these effects into a single measure and use this to compare the performance of different beamsplitter materials. We restricted the search to materials which had previously been successfully bonded using the hydroxide-catalysis bonding technique, and that had high transmission of light at  $\lambda = 1064$  nm. The data for the materials considered is shown in Table 3.1.

The properties of the various natural and synthetic fused silicas are very similar, and are better than the easily available alternatives. We therefore chose to have the beamsplitters and mirrors manufactured from Suprasil on the grounds of availability and cost. Suprasil has a refractive index of 1.45 at 1064 nm, a  $dn/dT$  of  $9.7 \times 10^{-6}$  per degree (measured at 644 nm) and coefficient of thermal expansion equal to  $0.51 \times 10^{-6}/K$ , giving a thermal coupling factor of  $\sim 8 \times 10^{-6}/K$ . For a total optical path in the material of 1.7 cm (three passes through beamsplitters) this corresponds to a temperature sensitivity of  $1.4 \times 10^{-7}$  m/K. For a target displacement noise of  $10 \text{ pm}/\sqrt{\text{Hz}}$  we will require a temperature stability of  $7 \times 10^{-5} \text{ K}/\sqrt{\text{Hz}}$ . In practice the amount of trans-

mission in each interferometer path is balanced so we expect largely common mode effects which will make this noise source less significant, as described in Section 4.3.9.

Table 3.1: Optical properties of potential beamsplitter substrates

Material	Refractive index (n)	Wavelength of refractive index measurement (nm)	dn/dT ( $\times 10^{-6}$ )	Wavelength of dn/dT measurement (nm)	$\alpha$ ( $\times 10^{-6}$ )	Thermal coupling factor $n \times \text{CTE} + \text{dn/dT}$ ( $\times 10^{-6}$ )
BK7	1.509	581	2.8	546	7	13
Fused silica	1.46	587	7.1	N/A	0.5	8
Zerodur®	1.54	587	13	650	0.02-0.1 depending on class	13 dominated by dn/dT
ULE®	1.48	N/A	11	N/A	0.03 depends on temperature	11 dominated by dn/dT
Suprasil	1.45	1064	9.7	644	0.51	10
Sapphire	1.75	1064	13	N/A	8	27
Spectrosil	1.45	N/A	~8	N/A	0.54	9

### Baseplate material

ULE®<sup>1</sup>, an ultra-low expansion titanium silicate glass<sup>1</sup> was chosen as the material for the baseplate due to its extremely low coefficient of thermal expansion ( $\leq \pm 0.03 \times 10^{-6}/\text{K}$  at 25°C [50]). Zerodur® (a glass ceramic) had been used in previous tests [51] and has very similar properties to ULE® but in this case ULE® was more readily available. A square of ULE® of side 400 mm, and 25 mm thick was decided on. This is approximately a factor of two larger than the final size of the LTP OB and was chosen to be representative of the scale of the LTP OB but to allow a less restricted working area for aligning and bonding the interferometers. The baseplate has holes along its edges for the mounting of Invar plates onto which fibre injectors and photodiodes may be attached. Invar is a controlled expansion iron/nickel alloy with thermal coefficient of expansion  $2 \times 10^{-6}/\text{K}$ .

### 3.1.3 Layout of interferometer

The optical layout of the interferometer consists of two beams forming three recombination points *via* six mirrors and nine beam splitters as labeled in Figure 3.1. The light is introduced onto the prototype OB using the two fibre couplers to the left of the diagram. One beam has been frequency shifted (by an acousto-optic modulator (AOM) prior to the fibre) by 80 MHz and the other (by a separate AOM) by 80.01 MHz. This results in a 10 kHz beat note when the beams are recombined.

There are three beam recombinations on the prototype OB (LTP will have four); giving the reference, measurement and frequency noise signals. The

---

<sup>1</sup>Trade name Corning 7971, composition 92.5% SiO<sub>2</sub>, 7.5% TiO<sub>2</sub>

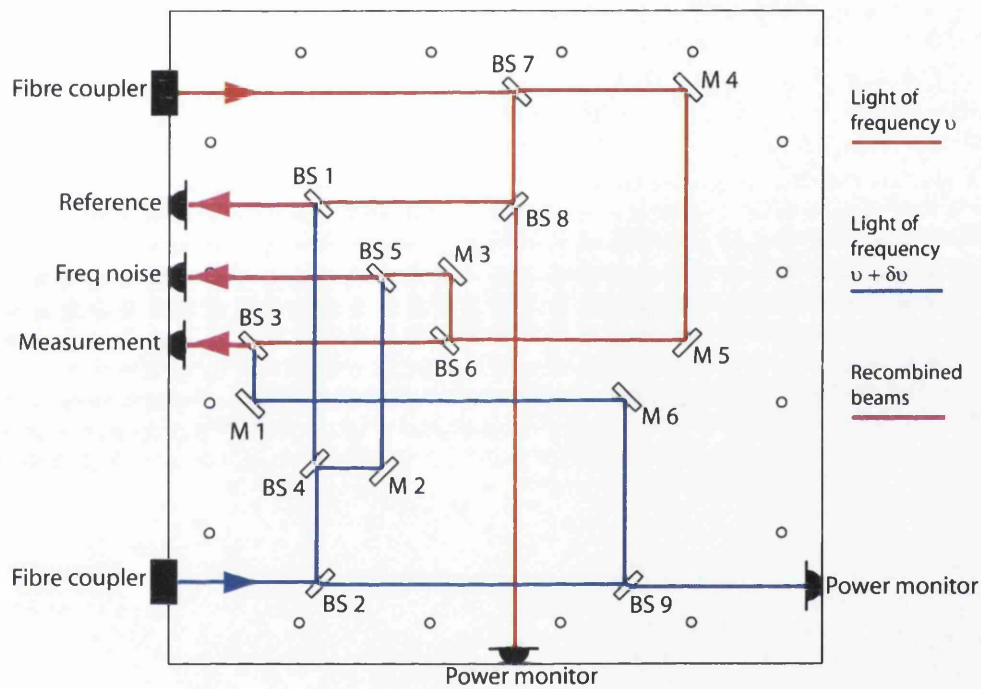


Figure 3.1: *Layout of optical paths on the prototype optical bench*

phase of the three outputs are monitored at the three named photodiodes on the left of Figure 3.1. The other two photodiodes are monitor photodiodes to measure the laser power injected onto the prototype OB by the two fibres.

Each pair of interferometer arms make the same number of passes through transmissive optics (*i.e.* reference paths through one per arm, measurement paths through three per arm and frequency noise paths through two per arm). As all the optical components are nominally at 45° incidence angle to the beams this means that each pair of arms has a balanced path length in the glass. This is to make the path length changes due to a thermally driven change in refractive index ( $dn/dT$ ) as common mode as possible.

The minimum requirement of the prototype OB is to provide an output optical signal whose phase can be measured with respect to a reference. The phase difference between two measured optical signals,  $\phi_{diff}$  is

$$\begin{aligned}\phi_{diff} &= \frac{2\pi d}{\lambda} \\ &= \frac{2\pi\nu d}{c}\end{aligned}\quad (3.1)$$

where  $\nu$  is the light frequency,  $\lambda$  is the wavelength of the light and  $d$  is the path length difference. The phase variation ( $\delta\phi$ ) between the two measured phases will change if the laser frequency changes (as  $\delta\nu$ ) or if the path length changes (as  $\delta d$ ):

$$\delta\phi = \frac{2\pi\nu}{c}\delta d + \frac{2\pi d}{c}\delta\nu. \quad (3.2)$$

The reference interferometer on the OB is used to remove the effects of path length changes on the laser injection bench and in the fibres. A third interferometer is also used on the OB to provide a measure of laser frequency noise, this interferometer purposely has a large path length difference (see Section 4.3.5).

### 3.1.4 Beam path lengths

Any interferometer with unbalanced optical path lengths in its two arms will be sensitive to laser frequency noise as described in Equation 3.2. In order to minimise this, the prototype optical bench interferometer was designed to have perfectly matched path lengths, but in practice an error of order a few millimetres can be expected during construction. To deal with this effect the laser frequency noise measuring interferometer is included in the optical set-up and is used as detailed in Section 4.3.5.

The beam path length differences were manipulated in the CAD model of the optical layout and the critical measurements are shown below (the number of significant figures reflects the CAD accuracy, not the alignment tolerances). All distances are quoted from the centre of the nominal reflection points.

#### *Measurement interferometer path length difference*

The critical distances for the paths making the measurement interferometer are:  $[(BS7 \text{ to } BS3) - (BS7 \text{ to } BS1)]$ , the difference between reference and measurement paths for light of frequency  $\nu$  and  $[(BS2 \text{ to } BS3) - (BS2 \text{ to } BS1)]$ , the difference between reference and measurement paths for light of frequency  $\nu + \delta\nu$ .

- The distance from BS7 to BS3 is:

$$5.7272 + 99.8077 + 153.1212 + 143.7574 + 5.7272 + 112.9291 = 521.0698 \text{ mm}$$

- The distance from BS7 to BS1 is:

$$66.8788 + 116.0501 + 5.7272 = 188.6561 \text{ mm}$$

- The distance from BS2 to BS3 is:

$$5.7272 + 182.9291 + 113.1212 + 226.8787 + 29.8079 + 5.7272 = 564.1913 \text{ mm}$$

- The distance from BS2 to BS1 is:

$$70 + 5.7272 + 156.0503 = 231.7775 \text{ mm}$$

- Giving:

$$\implies (\text{BS7 to BS3}) - (\text{BS7 to BS1}) = \underline{332.4137} \text{ mm}$$

and

$$\implies (\text{BS2 to BS3}) - (\text{BS2 to BS1}) = \underline{332.4138} \text{ mm}$$

as required.

#### *Frequency noise interferometer path length difference*

The critical distances for the frequency noise paths are:  $[(\text{BS7 to BS5}) - (\text{BS7 to BS1})]$ , the difference between reference and frequency noise paths for light of frequency  $\nu$  and  $[(\text{BS2 to BS5}) - (\text{BS2 to BS1})]$ , the difference between reference and frequency noise paths for light of frequency  $\nu + \delta\nu$ . These should be as different as possible to accentuate the frequency noise.

- The distance from BS7 to BS5 is:

$$5.7272 + 99.8077 + 153.1212 + 143.7574 + 40 + 40 = 489.4135 \text{ mm}$$

- The distance from BS7 to BS1 is:

$$66.8788 + 116.0501 + 5.7272 = 188.6561 \text{ mm}$$

- The distance from BS2 to BS5 is:

$$70 + 40 + 112.9289 + 5.7272 = 228.6570 \text{ mm}$$

- The distance from BS2 to BS1 is:

$$70 + 5.7272 + 156.0503 = 231.7775 \text{ mm}$$

- Giving:

$$\Rightarrow (\text{BS7 to BS5}) - (\text{BS7 to BS1}) = \underline{299.7574} \text{ mm}$$

and

$$\Rightarrow (\text{BS2 to BS5}) - (\text{BS2 to BS1}) = \underline{-3.1205} \text{ mm.}$$

This gives a frequency noise path length difference of 302.8779 mm

*Distance from fibre coupler to reference photodiode recombination point*

$$\text{Coupler to BS1 via BS7} = 240 + 66.8788 + 116.0501 + 5.7272 = \underline{428.6561} \text{ mm}$$

$$\text{Coupler to BS1 via BS2} = 120 + 70 + 5.7272 + 156.0503 = \underline{351.7775} \text{ mm.}$$

So, after input couplers the path *via* BS7 is 76.8786 mm longer than *via* BS2.

This difference is compensated before the fibre couplers (on the laser injection bench). While not strictly necessary this was implemented to keep common mode phase changes caused by laser frequency changes to a minimum.

*Cancellation of fibre noise*

Crucially, beam path variations from the laser injection bench (which is in air and a relatively unstable temperature environment compared to the OB in a vacuum enclosure) and the fibres are, in principle, canceled out in the phase measurement between the reference and measurement interferometers. These phase changes should produce purely common mode phase changes at the interferometer outputs. All the path variations prior to BS7 and BS2

should therefore, in principle, not enter into the measurements.

### 3.1.5 Tolerances

To achieve good fringe contrast at the output of the interferometers the two beams must be well matched in size and curvature and well aligned in angle and overlap. The two beams are launched onto the optical bench with a beam diameter of  $\sim 1$  mm which ensures very similar beam size and curvature at the interferometer output. There are four remaining degrees of freedom in alignment: two angles and two displacements. These can be broken down into two components for each alignment: vertical (the plane perpendicular to the beam paths) and horizontal (the plane parallel to the beam paths).

We set ourselves the target of a phase change across the beam diameter of less than  $\lambda/10$  due to angular misalignment. For a beam diameter of 1 mm and a wavelength of  $1 \mu\text{m}$  this is an alignment of  $100 \mu\text{radians}$  ( $\sim 22 \text{ arcsec}$ ).

We set ourselves a target of lateral beam displacement at 10% of the beam diameter,  $100 \mu\text{m}$  for a 1 mm diameter beam.

#### Vertical alignment tolerances

The bonding method used results in a bond thickness of the order of 100 nm [43]. Over a 5 mm bond the bonding layer has uniform thickness to a small fraction of this, resulting in the bond contributing negligible angular deviation to the component positioning. Hence alignment in the vertical direction can be achieved by the manufacture of the baseplate and components, in conjunction with introducing the beams parallel to the baseplate.

For the vertical beam alignment to be maintained the recombined beams have to make an angle less than  $\sim 22$  arcsec. This is the total error build up due to baseplate and component build up. This is the defining tolerance as a 22 arcsec angular deviation over the distances involved in the interferometers ( $\sim 0.5$  m) would cause a lateral beam displacement of  $\sim 50 \mu\text{m}$ .

The critical element of the reflective components is the perpendicularity of the bonding surface to the reflective surface - if the reflective surface is not at  $90^\circ$  to the incident beam then the beam will reflect at twice the deviation from  $90^\circ$ . This error can build up at each reflection point. The reference beams have a combined total of four reflections, the measurement beams six and the frequency noise beams eight. A tolerance of component perpendicularity of 3 arcsec was agreed with the manufacturer (this corresponds to a roll off of around 75 nm over a 5 mm flat and tighter tolerances would have proved difficult to manufacture). This would contribute a very worst case error of 24 arcsec (out of specification) but the risk of this was considered extremely minimal<sup>2</sup>.

The baseplate must be polished flat for bonding as well as to control vertical beam alignment. The constraint for bonding applies over length scales of order the size of the components to be bonded and requires a flatness of  $\lambda/10$  (this applies to the component surface to be bonded as well as the baseplate).

Deviations in flatness of the baseplate over large lengthscales ( $L$ ) will cause local variations in the gradient ( $\alpha$ ) of the baseplate with the maximum gradient being given by

$$\alpha_{max} = \frac{\pi d}{4L} \text{rad.} \quad (3.3)$$

---

<sup>2</sup>This would be a very extreme worst case situation of linear addition of all the errors in such a way as to maximise their effect. In practice there is very likely to be some cancellation of this error build up, even if there was a systematic error in the components.

The reasonably easily achieved polishing accuracy over lengthscales of 100 mm is  $\lambda/4$ , corresponding to  $\alpha_{max}$  of 0.4 arcsec. The surface polish of the bench was therefore specified as flat to an accuracy of  $\lambda/10$  or better over lengthscales of 30 mm and with a deviation of no more than  $\lambda/4$  per 100 mm.

These manufacturing constraints are sufficient to remove the need for vertical alignment of components.

### Horizontal alignment tolerances

The method of horizontal alignment must enable the components to be positioned and bonded within tolerance such that the interference quality at each of the three recombination points is within specification.

One possibility would be to use a fixed template (as described in 3.1.7) to position the mirrors and beamsplitters. The angular beam alignment tolerance of  $100 \mu\text{rad}$  and size of components (20 mm on the long side) result in an angular positioning of components at the  $\sim 1 \mu\text{m}$  level. This would be very difficult (if possible) to achieve using fixed mechanical references.

The preferred alternative was to incorporate a degree of adjustability into the construction process, allowing fine adjustment of some components using an optical readout to determine correct positioning of the components. This method involves placing the component on the baseplate and carrying out fine adjustment immediately prior to or during the bonding process and is described in Section 3.1.9.

There now follows a discussion of the resolution required for the fine adjustment of the horizontal beam angle and position, considering how a misalignment in component position would affect the output beam for both the reflected and

the transmitted beams.

### Factors effecting reflected beams

Angular misalignment occurs when the angle between the incoming beam and the reflecting surface is other than that intended. All beams on this OB are intended to make an angle of  $45^\circ$  with reflecting surfaces. If there is an angular misalignment of a component, there will be a corresponding angular shift of the beam. There will also be a lateral shift in beam position, although this is a small effect and we are less sensitive to it. For a component misalignment of  $\delta\theta$ , the beam path will be reflected at an angle  $2\delta\theta$  away from the intended angle. This misalignment would result in reduced contrast of the interference fringes when the beams are recombined. Thus the  $100\ \mu\text{rad}$  tolerance on angular position of beams means that  $50\ \mu\text{rad}$  resolution is required in component placement.

Lateral beam misalignment can also arise independently of angular alignment when the component is placed at a distance along the beam path other than that intended. If the component has the specified orientation with respect to the beam, but not the specified position, the reflected beams will be shifted laterally by the magnitude of misplacement. Assuming the component is bonded to the baseplate as defined by the template, any non-angular misalignment arises from the tolerance to which the template is engineered which, in our case, is less than  $\pm 0.05\ \text{mm}$ . Such an error reduces the overlap of the two recombined beams. This effect does not depend on distance traveled by the beam after deviation.

Although component thickness does not affect the reflected beams, it would result in an unplanned lateral offset error if the component was manufactured

to a thickness other than that for which the template was designed. Thus, the components must be of nominal thickness to within  $70\ \mu\text{m}$  ( $100\ \mu\text{m} \times \sin 45^\circ$ ).

### Factors effecting transmitted beams

Angular misalignment of the components would affect the transmitted beams as well as the reflected beams. The lateral shift due to transmission through a component has been calculated for  $45^\circ$  in the design of the OB. If the beam is not incident at this angle it will be following a different path to that intended. Figure 3.2 shows the magnitude of beam deviation with angle around the region of interest. The nominal beam shift ( $1.56\ \text{mm}$ ) has a tolerance of  $100\ \mu\text{m}$  associated with it (as it is purely a lateral shift) and it is clear that the entry angle can be more than a degree from nominal and still be within tolerance. This suggests that this alignment will not be a source of significant error.

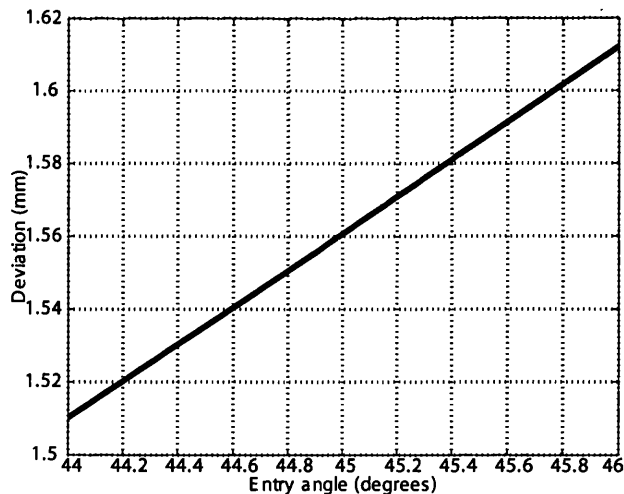


Figure 3.2: *Lateral beam shift on transmission with changing entry angle.*

If the components are not at the design thickness the beam will be laterally translated by a different amount than that assumed. This will alter the lateral shift as shown in Figure 3.3. It can be seen that this effect would be apparent

in the reflected beams first and is not significant in this context. A purely lateral shift on placement of component would not affect the transmitted beams significantly.

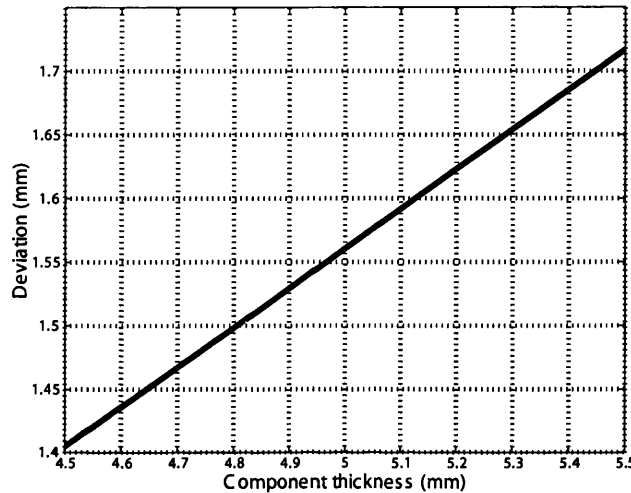


Figure 3.3: *Lateral beam shift on transmission with changing component thickness.*

### 3.1.6 Component Design

Other specifications were that the beamsplitter coating was specified to be  $50 \pm 1\%$  and the mirror coating to have  $> 95\%$  reflectance. The rear surface of both mirrors and beamsplitters was anti-reflection coated to reduce any problems that may be caused by stray beams. This coating was specified as having a reflectivity of  $< 0.2\%$ . The final specification was that none of the coating should contaminate the bonding surface as this could cause problems both with the bonding of the component and with the accuracy of the angle between the bonding surface and the mirror surface.

The mirrors and beamsplitter dimensions were chosen to be  $20 \times 20 \times 5$  mm, with one of the  $20 \times 5$  mm surfaces to be bonded to the optical bench, a mirror

or beamsplitter coating applied to one of the  $20 \times 20$  mm faces and an anti-reflection coating on the other. This is representative of the LTP components. The thickness of the beamsplitters is a compromise between reducing the path length of light in the beamsplitters, ease of manufacture, and ease of handling when bonding the interferometer. An aspect ratio of around four was the maximum that provided reasonable handling characteristics and was therefore chosen. The mirrors could, in principle, have had a lower aspect ratio as they do not require such precise handling, but using the same dimensions as the beamsplitters provided a modest cost saving without any performance penalty.

### 3.1.7 Method of construction

As a quasi-monolithic optical bench of this complexity had never been constructed previously a system was devised to locate the components with the required accuracy. The bonding technique has been verified several times [43, 44], although not for components requiring fine adjustment while bonding.

The fundamental principle was to locate two sides of each component in their nominal positions by placing them against a metal superstructure (in the form of a brass template). The template was designed so that the position and orientation of the component surfaces were defined by two machined, perpendicular surfaces. Small radii were removed from the critical corners between the perpendicular brass faces as it is not possible to machine an exact right angle, an example is shown in Figure 3.4.

The construction of the OB consisted of two phases: the bonding of the non-adjustable components and the bonding of the adjustable components.



Figure 3.4: *Close up of brass template showing locating surfaces and corners with radii removed.*

### 3.1.8 Non-adjustable components

The brass template alone was used to position the nine non-adjustable components. The template design was created from the CAD layout of the optical bench. The template was made from a piece of  $400 \times 400 \times 4$  mm brass with regions machined out corresponding to each component on the optical baseplate.

The template was to be placed above the baseplate prior to (and during) bonding. Fixing holes were drilled around the edge of the brass, matching the fixing holes on the ULE® baseplate. The fixing holes for the template were oversized so that it could be easily removed when the components had been bonded in place. The area around where a component was to be bonded was made large enough for easy access while bonding without being large enough to degrade the structural stability of the brass sheet, or interfere with the other features of the template.

The template was designed so that the beam height (12 mm above the baseplate) was above the brass. Marks were etched into the brass during machining to assist in determining mirror/beamsplitter locations and also which way the reflective side was to face. A photograph of the template is shown in Figure 3.5. This also shows the adjustable hinges described in Section 3.1.9.

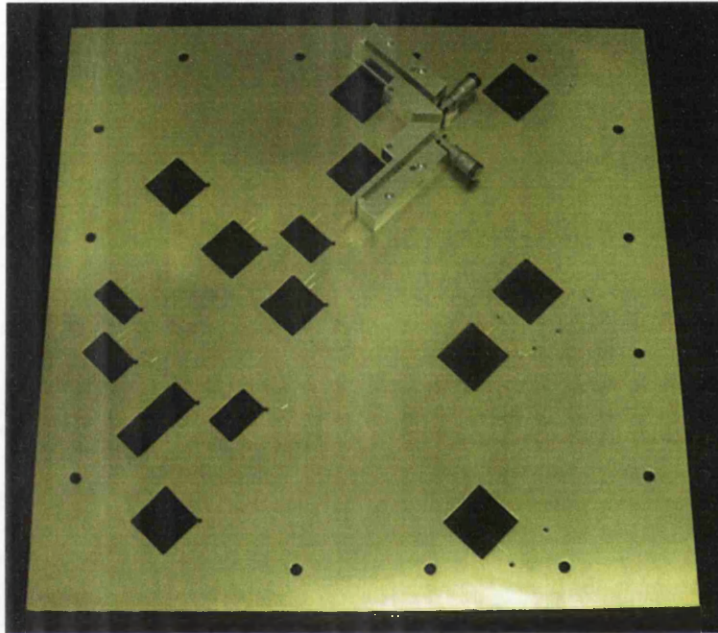


Figure 3.5: *The brass alignment template for bonding the prototype optical bench. The hinges for aligning adjustable components are shown attached to the template.*

To ensure that the components lay against the two defining template faces, in keeping with the principle of the template, the optical bench (and template) were inclined at  $\sim 5^\circ$  during bonding. This angle of inclination is enough to ensure that the components rest against the brass faces whilst not tilting off vertical. The template was designed such that all the components rest on the critical surfaces from the same direction, removing the need to reposition the template for each bond.

### 3.1.9 Adjustable components

When bonding the adjustable components in place adjusters were fixed to the template. In these cases adjusters take the place of the machined, perpendicular surfaces of the brass template.

For each recombination two degrees of freedom are required (two are fixed) to align the beams - angular and lateral position. The method chosen was to adjust the angle of two reflected beams to obtain the desired alignment. The optical beams were introduced to the interferometer for this procedure. This allowed the alignment to be judged by looking at the contrast of the interference. Using the final optical beams to optimise the alignment automatically compensates for any small misalignment due to machining tolerances of the template affecting the positioning of the non-adjustable components.

To control the positioning of the adjustable components, adjusters were designed and manufactured. The adjusters work on the same principle as the template: two defining faces are used to locate a component. A CAD drawing of a left-handed adjuster is shown in Figure 3.6 (the right handed adjuster is a mirror image). These are designed not to interfere with any optical beams so that they can be used in conjunction with the laser to align the critical components.

When using the adjusters the beams from the heterodyne injection bench were used to illuminate the quadrant photodiode. To obtain the required resolution of adjustment the mechanism consisted of a micrometer driving a lever arm. The micrometers used had a nominal resolution of  $10\ \mu\text{m}$  (with a more than ample  $\pm 5\ \text{mm}$  of travel) and the lever arm measured 72 mm from hinge to micrometer contact point. This translates to an angular resolution of 29.2 arcsec per adjuster.

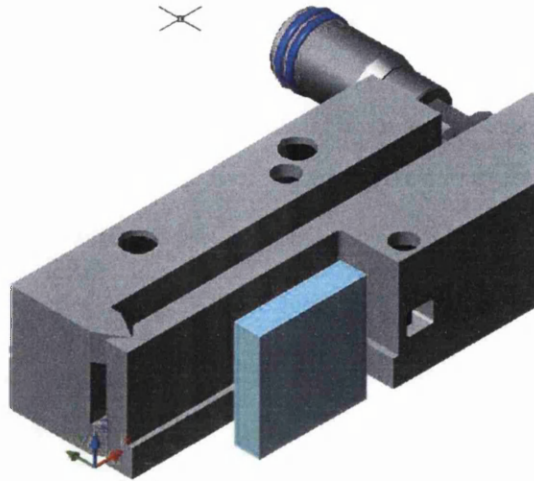


Figure 3.6: *CAD drawing of left handed fine adjuster. The light blue cuboid represents a mirror/beamsplitter component.*

Tapped holes were made in the brass template in the appropriate places to attach the adjusters in place next to each of the six components where adjustability was necessary.

### **Development of a technique to prevent optical contacting during alignment**

The adjustable technique described relies on being able to place the component on the baseplate close to the nominal position and then make fine adjustments. The component can then be removed, bonding fluid applied and the component replaced for the bonding to take place. The first problem with this procedure is that when two very flat and clean surfaces are brought into close proximity during the dry alignment phase they are very likely to optically contact. If this phase is omitted, then during the bonding phase there is a settling time of around 30 seconds from the component placement until the bond has started to form, but this does not provide sufficient time to align the interferometer.

In an attempt to avoid optical contacting whilst still allowing fine component positioning a series of tests were conducted during which a component was floated on a buffer fluid. For the buffer fluid to be a suitable candidate for this application it must have suitably low viscosity to allow component positioning and evaporate without leaving any residue that could interfere with the bonding process.

The alkanes octane, nonane and decane were investigated. Alkanes are hydrocarbons that contain only single bonds, the simplest being methane. These alkanes were chosen due to their low viscosity and their availability with low residue on evaporation properties (the tested products had a residue on evaporation of  $< 5$  ppm). The range of different alkanes were tested in order to identify the one with the most suitable rate of evaporation.

Octane was selected as having the most suitable evaporation rate and bonding tests were carried out on surfaces that had been prepared for bonding and then coated in octane. The octane was then allowed to evaporate (in a clean environment) and a bond was made with no further treatment or cleaning of the surfaces. This is an important aspect of the process as it was not possible to clean the baseplate area to be bonded after component positioning.

Approximately  $10\ \mu\text{l}$  of octane allowed three minutes of adjustment time for components of  $20 \times 5$  mm footprint without risk of optical contacting. The process is repeatable and so it is possible to align an interferometer with much reduced time pressure. It should be noted that the risk of scratching the surfaces increases with each removal and replacing of the components, which could result in inferior bond quality.

A feature of this method of alignment is that the buffer fluid does not necessarily form an even layer and this can result in misalignment of the two beams

in the vertical direction. This is seen as a phase difference between the heterodyne signals (measured using a quadrant photodiode) from the top quadrants and the lower quadrants. This effect reduces as the octane evaporates and is removed when the actual bonding fluid is used. The signals monitored during alignment are the contrast of the individual quadrants and the left to right quadrants' phase difference (or alternatively the summed contrast of all four quadrants, which depends on the contrast and phase of the four quadrants). Final small adjustments can be made after the application of the bonding fluid, although there is very limited scope for this during the rapid settling of the bond.

This technique for adjustable component bonding was successfully used in the prototype optical bench construction. This resulted in it later being used during the LTP optical bench engineering model (see Chapter 5) and it will also be used in the LTP optical bench flight model construction (see Chapter 6).

## 3.2 Construction

In the following account of the construction process the details of the bonding procedure have been omitted for clarity. They are found in [43, 44].

The baseplate, template and components were cleaned to a high degree using previously developed methods. The bonding was undertaken in a laminar flow cabinet, which was in a semi-clean laboratory. The components were cleaned in the semi-clean area and moved to the ultra-clean cabinet for the final cleaning stage. The particulate count inside the cabinet was measured using a particle counter, which registered zero counts over five minutes for 0.1, 1 and 10  $\mu\text{m}$  particles. This was a considered a satisfactory environment for the bonding.

### 3.2.1 Verification of component perpendicularity

Following delivery of the components, the perpendicularity of the reflecting face to the bonding face was tested. This was done by ‘water bonding’<sup>3</sup> the bonding surfaces of two mirrors together to create a composite  $40 \times 20 \times 5$  mm piece which is nominally flat as shown in Figure 3.7. Figure 3.8 shows the view through a water bond (looking along the long axis of a composite piece).

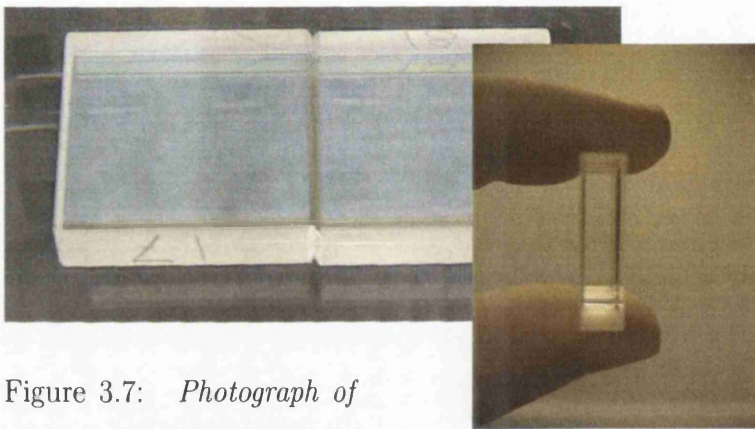


Figure 3.7: *Photograph of a ‘composite component’ - two normal components water bonded together*

Figure 3.8: *Photograph viewing through a water bond*

The flatness of the composite piece was then tested using a grazing incidence interferometer (Logitech GI20 Flatness Measurement System [52]), as indicated in Figure 3.9. In the case of a component having non-perpendicular bonding and reflection surfaces, the interferometer shows a departure from a nominal flat piece.

---

<sup>3</sup>This bonding procedure is virtually identical to the hydroxide-catalysis bonding used in the final interferometer, the only difference being that water rather than a hydroxide solution is used. This is a bond with similar properties to the hydroxide-catalysis bond but the bond can be unmade by soaking in deionised water and the process does not damage the surfaces.

The bonds are sufficiently strong (even after a short amount of time before the bond has fully set) to maintain the relative positions of the two components under small loads, *i.e.* moving and placing the composite structure on the interferometer.

The components were then de-bonded. One component was rotated through  $180^\circ$  about the bonding surface and they were re-bonded in this new orientation.

The composite mirror was measured in both orientations to remove the risk of imperfect components appearing within specification by having compensating errors. This could occur due to a chance matching of component error angles or by some systematic effect during manufacture causing matching error angles. An illustration of this effect is shown in Figure 3.9.

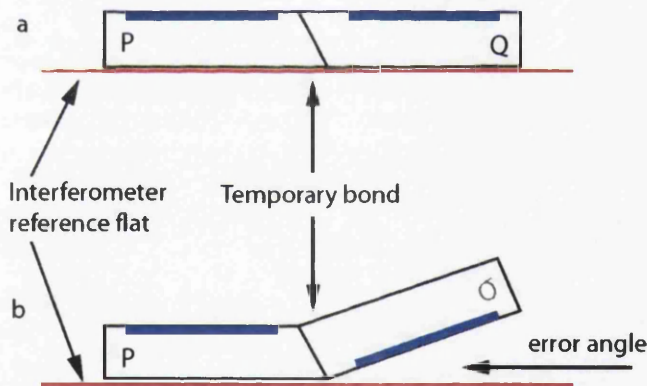


Figure 3.9: Diagrams showing 'composite' mirror (side view) of components 'P' and 'Q'. The blue rectangles indicate the mirror coating: a. showing cancellation of component error angles due to non-perpendicularity of bonding and reflecting surfaces, b. manifestation of error angle showing component imperfection.

### Measurement resolution

A complete fringe of the GI20 interferometer corresponds to a change of  $2\ \mu\text{m}$  in the distance from the interferometer reference flat to the measured piece [52]. It is possible to resolve to better than one fifth of a fringe which corresponds to  $\sim 20\ \mu\text{radians}$  ( $\sim 4\ \text{arcseconds}$ ) over 20 mm, which is suitable resolution for verification of component perpendicularity for this application.

This measurement is of a combined error and it is not possible to disentangle it to determine the absolute angular error between bonding and reflecting faces for each component unless one angle is already known.

### Bond thickness variations

A bond has finite thickness but it may also have some variation in thickness across its length. A variation in bond thickness would appear as a variation in error angle and in a worst case scenario could compensate for the error angle, making a defective component appear within tolerance as shown (greatly exaggerated) in Figure 3.10. Bond thickness varies with the concentration of bonding fluid used, becoming thicker with higher ratio of sodium silicate solution to water.

A variation across the bonding surface (5 mm) of 35 nm would appear as an error angle of  $\sim 1\ \text{arcsecond}$  ( $7\ \mu\text{radians}$ ). Measured bond thicknesses for bonds made using weak concentrations of bonding fluid (similar to those used for these tests and expected to be similar to that of a water bond) are  $81 \pm 3\ \text{nm}$  [43]. It is not expected that a variation as large as 35 nm will be present in a bond of thickness 81 nm, suggesting that the error angle contribution due to bond thickness variation should be smaller than the resolution required.

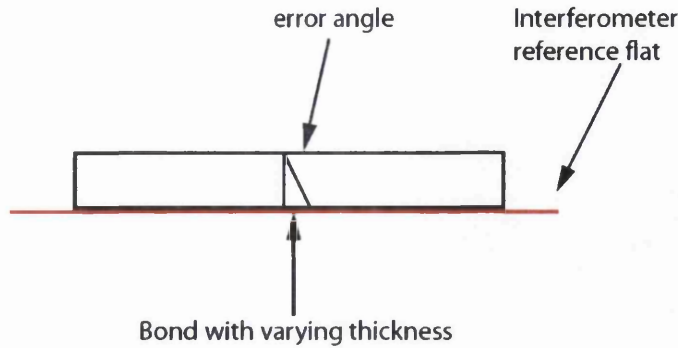


Figure 3.10: Diagram showing 'composite' mirror (side view) with variation of bond thickness negating component error angle

### Interpretation of combined error angle

The components were placed on the interferometer such that there was an air wedge between both mirrors and the reference flat, which generates fringes across both surfaces<sup>4</sup>. This results in a number of fringes,  $n$ , across one mirror and  $n + \delta$  across the other (where  $\delta$  is dictated by the error angle). The combined error angle for this orientation can then be calculated.

When one component is removed, rotated by  $180^\circ$  about the bonding surface and re-bonded, a different combined error angle will be seen (unless one or both pieces are square). For two components,  $a$  and  $b$ , with error angles  $EA_a$  and  $EA_b$ , then the largest combined error angle ( $CEA_1$ ) would be

$$CEA_1 = EA_a + EA_b$$

and the other possible combined error angle,  $CEA_2$  (for the other component orientation), would be

$$CEA_2 = EA_a - EA_b.$$

Measuring  $CEA_1$  and  $CEA_2$  allows the calculation of  $EA_a$  and  $EA_b$ , but not

<sup>4</sup>In practice this is usually unavoidable

the determination of which component contributed which error angle.

### Results of tests

The first pieces tested using this technique showed a deviation from flatness of  $\sim 60$  arcsec, well outside the expected 6 arcsec. An example measurement is shown in Figure 3.11, where the superimposed red line has been drawn to show the method used for fringe counting. The two mirrors show a difference in slope with respect to the interferometer flat of approximately 3.5 fringes, corresponding to an angle of  $\sim 70$  arcsec. Further inspection of the remaining pieces showed that in many cases the bonding surface was contaminated by spillage of the optical coatings.

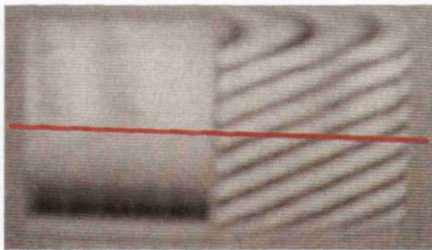


Figure 3.11: *Flatness measurement of two water bonded components before repolishing.*



Figure 3.12: *Flatness measurement of two water bonded components after repolishing.*

All the pieces were returned to the manufacturer and the fault in the manufacturing process was traced. A remedial repolishing technique was identified and the pieces were corrected and individually measured by the manufacturer. The pieces were again tested on return from the manufacturer and found to be within specification. Figure 3.12 shows an example of the flatness of the conjugate water bonded piece after repolishing. The fringe difference is less than one third of a fringe, corresponding to less than 6 arcsec.

### 3.2.2 Non-adjustable component bonding

The nine non-adjustable components were located and bonded using only the template as a reference. Only four bolts were used to attach the brass template to the ULE® baseplate. This allowed fast removal of the template in case of an unacceptable bond, thus giving full access to the bond and maximising the chances of successfully removing the bond with little or no damage to the component or baseplate.

Initially the template is located aligned to the baseplate using the fixing holes. When the first two components have been bonded they become the reference for locating the template. In this case the template can be removed and then realigned to these bonded components. This becomes important if the template has to be removed and replaced for some reason, *e.g.* re-cleaning. For this reason, two cubes with a long baseline between them were chosen to make replacement of the template as accurate as possible.

The components were bonded nearest to the bonding technician (who is ‘down wind’ of the baseplate) to minimise the risk of contaminating areas of the baseplate to be bonded to. In the case of any contamination that could not be removed with a jet of clean air, the removal of the template is necessary to re-clean the area.

It can be seen from Figure 3.1 that when nine of the components are bonded (relying on the accuracy of the template), namely BS1, BS2, BS3, M1, BS4, BS5, M2, M3 and BS6, the reference photodiode and the frequency noise photodiode can each be illuminated with one beam.

Figure 3.13 shows the brass template above the baseplate with the nine non-adjustable components in place. In the foreground of the photograph the

invar mounting bracket can be seen. This is for attaching the fibre injectors and quadrant photodiode for the adjustable component bonding.

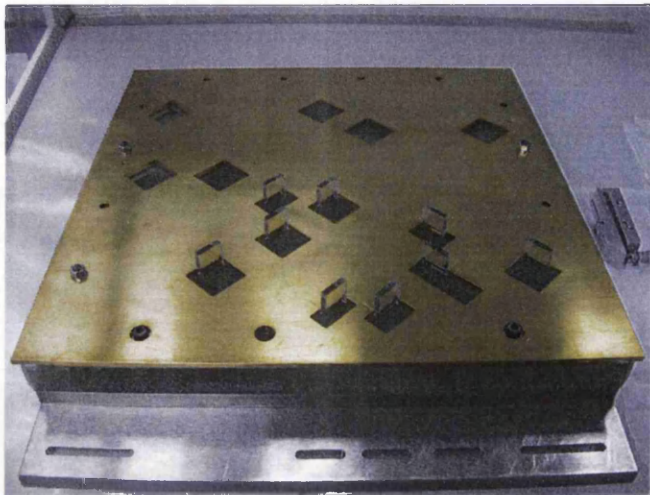


Figure 3.13: *OB after first nine components have been bonded, showing the brass alignment template in position above the baseplate*

### 3.2.3 Adjustable component bonding

With all the non-adjustable components in place the laser beams are introduced onto the OB. When BS7 and BS8 are correctly placed the reference recombination is completed. BS7 and BS8 are judged to be in the correct position when the alignment of the two beams hitting the reference photodiode are colinear and overlapping with the required precision, *i.e.* the required contrast of the heterodyne beatnote fringes is seen.

The same process was followed for the frequency noise photodiode using M4 and M5. With M4 and M5 in place we can see that the final recombination to the measurement photodiode is now illuminated by one beam, so the last two components (M6 and BS9) can be positioned using the same technique to

complete the measurement recombination.

A quadrant photodiode was used to monitor the alignment. The quadrant photodiode was centered on the beam from already bonded components and the two final components in the path positioned using the adjusters with a bonding technique that was developed specifically for this use.

Figure 3.14 shows the adjusters in position immediately after the final two components (M4 and M5) had been bonded. Figure 3.15 shows the completed optical bench with brass template removed.

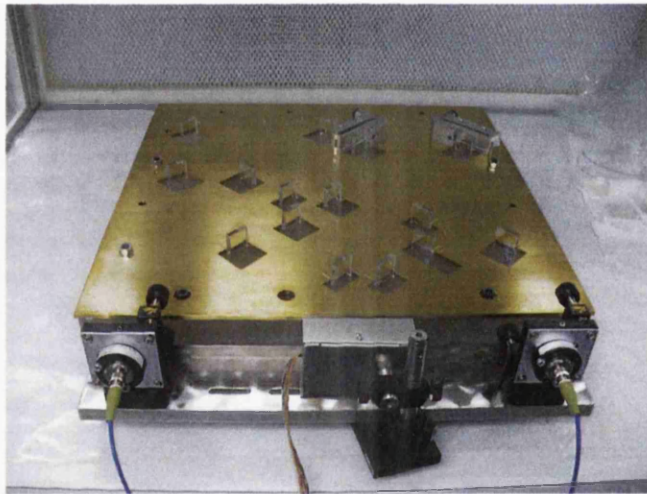


Figure 3.14: *Prototype optical bench during bonding showing fibre couplers and quadrant photodiode attached to invar mount (foreground) and adjusters (back right)*

### 3.3 Contrast of output signals

The contrast of the interference fringes at the interferometer output depends on collinearity, overlap, power matching and mode matching of the beams. It

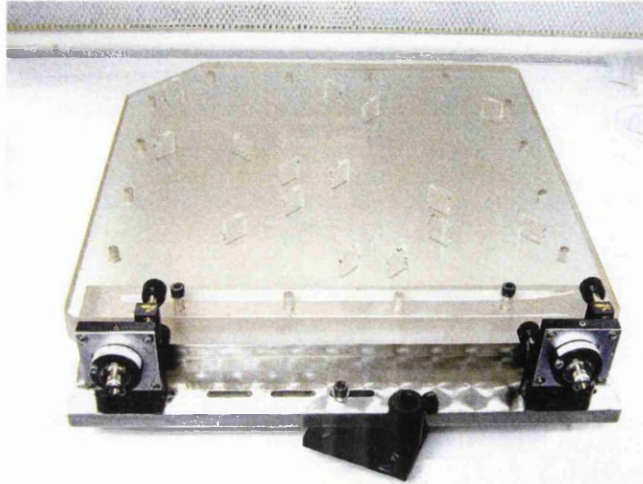


Figure 3.15: *Fully bonded optical bench with fibre couplers attached to invar mount*

should be noted that the contrast of the output signals from the prototype optical bench is not as critical as for the LTP optical bench as all beams are fixed and *d.c.* components can be removed by filtering. The contrast is calculated from measurements of the heterodyne signal by

$$\text{Contrast} = \frac{\text{Maximum signal} - \text{Minimum signal}}{\text{Maximum signal} + \text{Minimum signal}} \quad (3.4)$$

The heterodyne signals as measured upon installation of the OB in the clean facility after bonding are shown in Figure 3.16.

The contrast of the reference and measurement paths is  $\sim 58\%$  and  $\sim 55\%$  respectively, while that of the frequency noise signal is  $\sim 12\%$ . Clearly the beams interfering to give the frequency noise signal are significantly misaligned. The reference and measurement signals are acceptable. All of the signals show lower contrast than when initially bonded and the change in signal is attributed to movement of the fibre couplers relative to the optical bench. These couplers are bolted onto the invar shelf, which is bolted to the ULE® bench. The glass to metal fixings are thought to have shifted slightly during transit from the

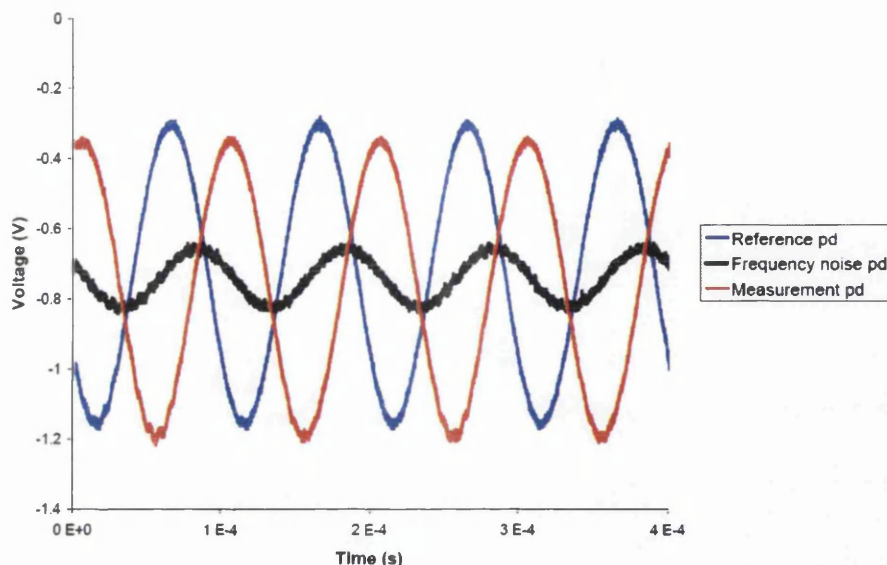


Figure 3.16: *Heterodyne signals at the output of the optical bench upon installation.*

bonding lab to the interferometry lab: the risk of cracking the ULE® limits the extent to which the bolts may be tightened<sup>5</sup>.

Investigation revealed that the frequency noise beams exhibited good relative angular alignment but had significant lateral misalignment. An additional beamsplitter was placed on the OB in one of the frequency noise arms (rotated at an angle less than 90° to the beam) to help reduce the lateral misalignment by acting as an inclined optical flat. This also introduces a power mismatch between the two interferometer arms and also a different number of transmissions through components, but these only have a second order effect on the contrast. This is the least critical interference and lower contrast here will not degrade the overall interferometer performance. The resulting (improved)

<sup>5</sup>This design of fibre injector is a simple solution with obvious limitations. The fibre injectors for the LTP engineering and flight models are bonded to the baseplate. This makes alignment significantly more difficult but fixes the beam location with respect to the interferometer rigidly.

signal is shown in Figure 3.17.

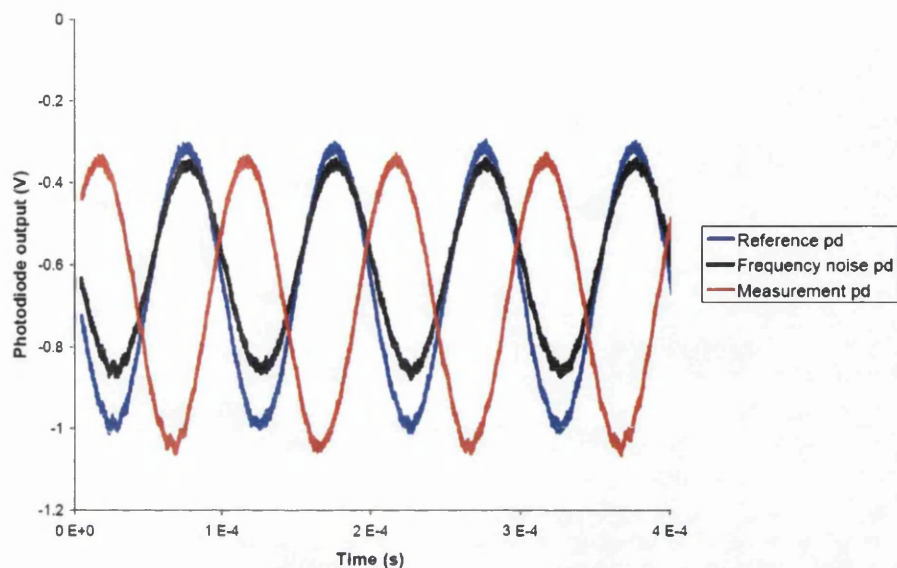


Figure 3.17: *Heterodyne signals at the output of the optical bench (with improved contrast in the frequency noise arm).*

The reference signal now has a contrast of  $\sim 52\%$  and the measurement signal a contrast of  $\sim 50\%$  while the frequency noise signal has an improved contrast of  $\sim 41\%$ .

The angles of the beams onto the optical bench were optimised using by adjusting the fibre couplers. This led to improved contrasts of  $\sim 69\%$  for the reference interference,  $\sim 68\%$  for the measurement interference and  $\sim 58\%$  for the frequency noise interference. These signals are perfectly adequate to drive the phasemeter inputs (after suitable filtering).

Returning the beam positions to their bonding alignments by repositioning of the fibre couplers would improve these signal contrasts further. This was not necessary and using the reduced contrast signals was considered preferable to risking useable signals in an effort to increase contrast by a few percent.

# Chapter 4

## LISA Pathfinder prototype optical bench interferometry

### 4.1 Experimental setup

A schematic of the overall setup is shown in Figure 4.1 and consists of three parts: beam preparation, optical bench (in vacuum tank) and phase measurement system.

The optical beams were prepared on an optical table (described in Section 4.1.1) next to the vacuum tank and supplied to the OB *via* single mode polarisation maintaining fibres and fibre feedthroughs. After circulation on the OB the recombined beams passed through a window and onto the measurement photodiodes (see Section 4.1.2). The photodiodes were mounted outside the vacuum chamber for convenience with the option of locating them on the invar shelf (bolted to the ULE® baseplate) if required. The fibre injectors' alignment to the OB is very critical and so these were always mounted on the invar shelf.

The signals from the photodiodes were fed into the phase measuring system (PMS) as described in Section 4.1.2.

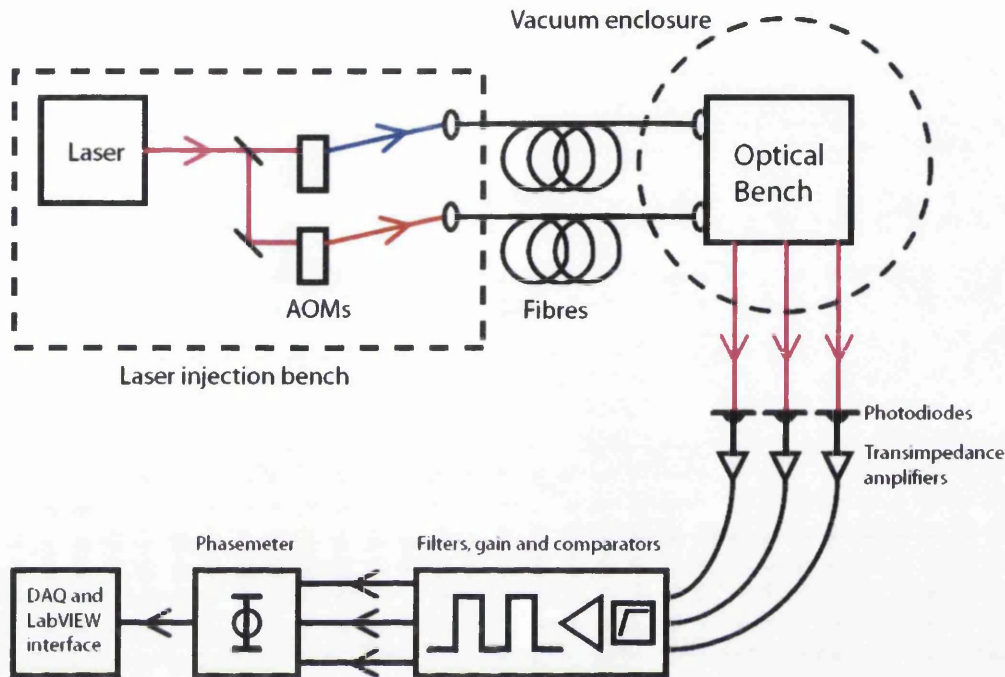


Figure 4.1: Schematic layout of laser injection bench, prototype optical bench, measurement photodiodes and phase measurement system. The optical beam colour key used in Figure 3.1 is also used here.

#### 4.1.1 Laser injection bench

A laser beam preparation bench was required to produce two frequency shifted, but otherwise identical, single mode laser beams to be fibre coupled onto the optical bench. This was achieved using light (of wavelength 1064 nm) from one laser split into two beams and frequency shifted using two independent acousto-optic modulators (AOMs), one operating at 80 MHz and the other at 80.01 MHz. A labeled photograph of the injection bench is shown in Figure 4.2.

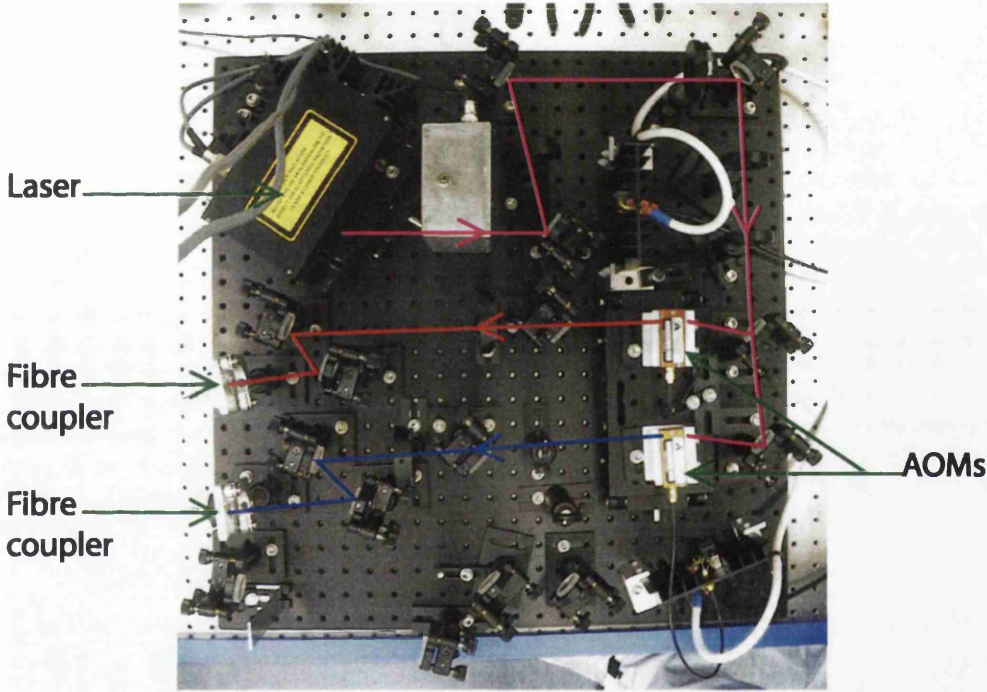


Figure 4.2: Photograph of the laser injection bench. Beam paths are shown using the same colour key as Figure 3.1.

To obtain light transmission through the fibres the beams must be mode matched to the fibre core diameter. To do this the beam parameters must be known and appropriate lenses must be chosen and positioned on the beam propagation axis to provide a beam of the correct diameter and curvature at the fibre.

The expansion of a Gaussian beam is given by

$$\omega(z) = \sqrt{\omega_0^2 + \frac{z^2 \lambda^2}{\pi^2 \omega_0^2}}, \quad (4.1)$$

where  $\omega(z)$  is the beam radius at a distance  $z$  from a waist of  $\omega_0$  and  $\lambda$  is the wavelength of the light [53]. Where the position of the waist ( $z = 0$ ) is not known we can replace  $z$  with  $z_1 - a$  and expect to get

$$[\omega(z_1)]^2 = \frac{\lambda^2}{\pi^2 \omega_0^2} z_1^2 - \frac{2\lambda^2 a}{\pi^2 \omega_0^2} z_1 + \frac{\lambda^2 a^2}{\pi^2 \omega_0^2} + \omega_0^2. \quad (4.2)$$

The laser beam diameter was measured at several locations along the beam propagation axis and the waist position and size calculated by plotting  $[\omega(z_1)]^2$  against  $z_1$  and fitting to a hyperbola using Matlab® [54], as shown in Figure 4.3. This yields the coefficients of  $z_1$  in Equation 4.2 from which the size of the laser waist and its position ( $\omega_0$  and  $a$ ) were calculated.

Once these parameters were known the evolution of the beam was mapped such that the beam size and curvature at the fibre were matched.

The laser used was an 800 mW Innolight Nd:YAG non planar ring oscillator with internal ‘noise eater’ [55]. The AOMs were made using TeO<sub>2</sub> cells by AA Opto-Electronique, model AA.MT.80/B20/A1@1.06  $\mu\text{m}$ . These were driven by two phase locked Agilent 8648A signal generators and Motorola CA2832C power amplifiers. The Motorola amplifiers were chosen for their low noise performance [56]. They provide wideband linear amplification: 35.5 dB of gain

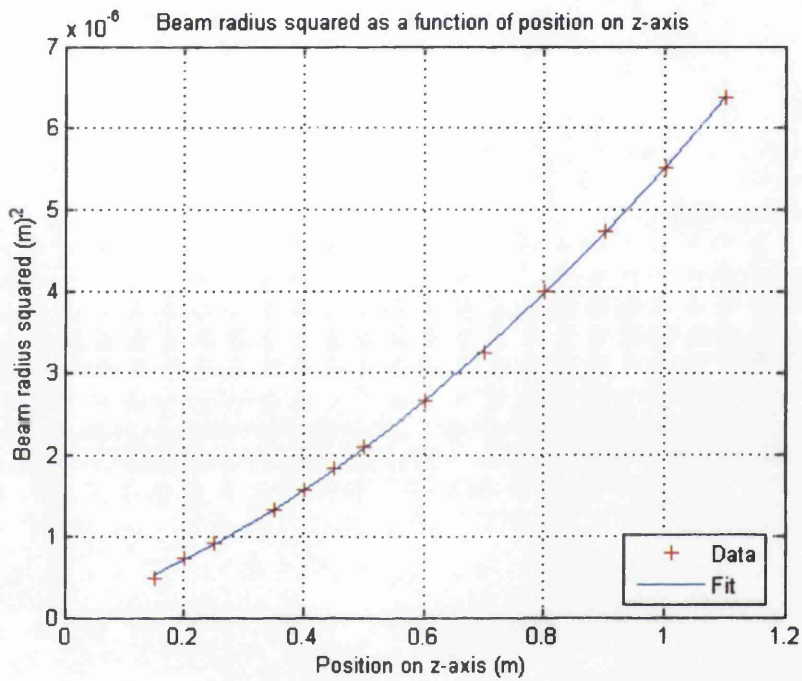


Figure 4.3: Plot showing beam parameter fitting. The red crosses are measured data points and the blue line is the fitted data.

from 1-200 MHz with 1.6 W maximum output power (ensuring they could not damage the AOMs which are rated to 2.5 W *rf* input power).

The optical fibres were manufactured by OZ Optics and were single mode polarisation maintaining fibres with FC connectors (model HPUC-23AF-1064-P-6.2AS-11).

This injection bench was used to provide the signals for alignment of the final OB components during the construction phase (Section 3.1.9) and for the stability tests described in this Section. For this reason it was constructed on a separate bench for transportability.

#### 4.1.2 Phase measurement system

The phase measuring system consisted of front end photodiodes, signal conditioning electronics and a digital phasemeter (read out using a data acquisition card with LabVIEW interface).

The principle of operation was to employ a ‘stopwatch’ style phasemeter that counted the number of fast clock cycles between consecutive rising edges of the heterodyne beatnotes, as shown in Figure 4.4. The phase difference between the waveforms is obtained by measuring  $t$ , the time interval between rising edges of the reference and measurement signals.

The time for one full reference cycle,  $T$ , is measured in order to scale the signal and therefore make the relative phase measurement insensitive to frequency drifts.

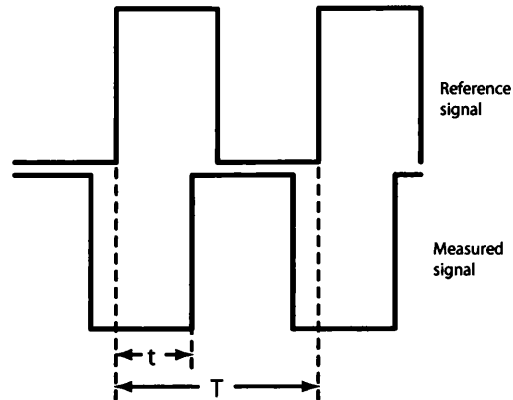


Figure 4.4: Principle of the 'stopwatch' style phasemeter.

### Photodiodes

The three 10 kHz measurement front ends used were silicon photodiodes with an active area of  $41.3 \text{ mm}^2$ , supplied by RS, stock number 651-995. The active area is square with side 6.4 mm. Each photodiode had a custom built transimpedance amplifier and 330 kHz filter. The circuit diagram is shown in Figure 4.5. The cases were connected to the circuit ground but isolated from the optical table using insulating posts. The opamps were LT 1028.

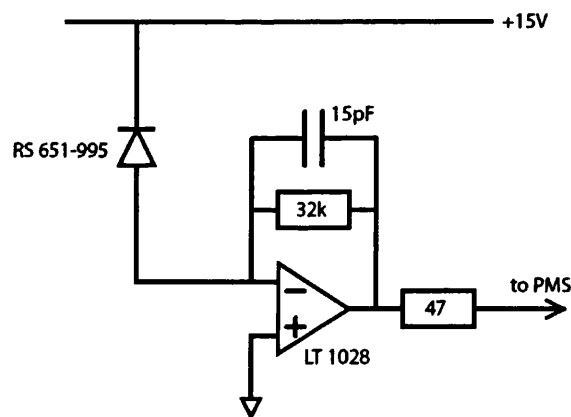


Figure 4.5: Circuit diagram of the 10 kHz measurement photodiodes.

### Signal conditioning

The phasemeter requires digital input signals, as shown in Figure 4.4. The original heterodyne signals are sine waves, however, and so some manipulation of the signals is required, without corrupting the phase information. Each signal was high pass filtered, amplified and fed into a comparator chip (AD790 [57]).

This made the switching point of the comparators insensitive to changes in the amplitude of the heterodyne signal. Also to this end, components with low temperature coefficients were used and corner frequencies were suitably far from the measurement frequency. Finally, the signals were converted to digital waveforms by the comparator.

### Digital phasemeter

The phasemeter used in these experiments was an enhanced version of that developed for the experiments described in [58].

The data is accumulated in two Altera® Flex® logic chips and read out (at a chosen rate) to a PC by a National Instruments Digital I/O card. LabVIEW software was used to record the data, which was later processed using Matlab. A photograph of the two Altera® chips on the printed circuit board is shown in Figure 4.6.

The phasemeter is capable of reading in five signals - one reference and the four measured channels (whose phase is compared to the common reference).

The fundamental limiting noise source for this phasemeter is quantisation noise, which is a function of the signal and fast clock frequencies.

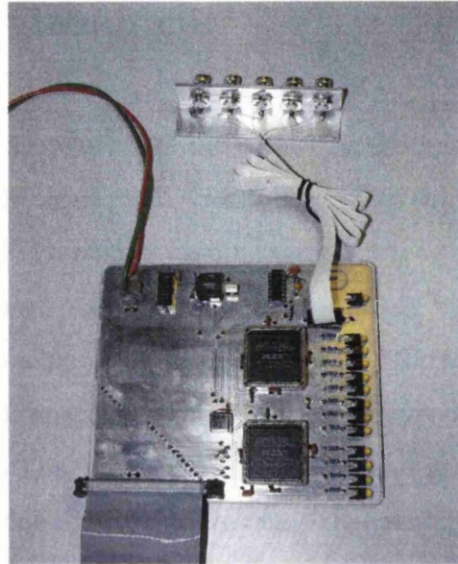


Figure 4.6: *Photograph of the logic chips in the 'stopwatch' style phasemeter.*

The phasemeter incorporated additional features (that are outwith the scope of this thesis) in order to measure down to the noise levels required. These include measuring two separate time intervals for each cycle and taking particular care of counting at cycle boundaries (required for multiple cycle phase shifts). On board averaging was also implemented and led the final output data rate to the controlling computer being adjustable up to  $\sim 100$  Hz.

The type of phasemeter selected for LTP uses a fast analogue to digital converter to digitise the heterodyne signals. The phase differences are then determined digitally by discrete Fourier transform [46]. A prototype phasemeter of this kind was tested with this OB as detailed in Section 4.3.7.

## 4.2 Test environment

The performance measurements of the prototype OB interferometer were conducted in a class 1000 clean room with temperature controlled clean air. The OB was housed in a 1 m diameter vacuum tank which could be evacuated using a magnetically levitated 1000 l/s turbo pump backed by a scroll pump. The system is designed to achieve pressures of order  $10^{-6}$  Torr. The air cleaning and conditioning system is specified to maintain the temperature in the laboratory to within  $1^\circ$  of  $20^\circ\text{C}$ . The temperature in the lab and in the vacuum tank was monitored and recorded during data taking. The pressure in the vacuum tank during experimental runs was  $\sim 2 \times 10^{-2}$  mbar, which is adequate to passively shield against local temperature variations and convection currents. Locating the OB in a closed tank also reduces optical path length changes due to air currents.

Figures 4.7 and 4.8 show typical temperature variations in the test facility. The vacuum tank provides a thermal environment more than two orders of magnitude quieter than the ambient laboratory in the mHz region.

## 4.3 Optical bench noise performance

On the prototype optical bench a reference signal is generated by splitting some of the light from each of the fibre couplers and combining them to form an interference (a 10 kHz beatnote). The measurement beatnote comes from light that has traveled a further distance around the optical bench and is then similarly combined. If one path changes differentially in length by one wavelength ( $1.06 \mu\text{m}$ ) with respect to the other then the phase difference between the two interferometer outputs would change by one cycle.

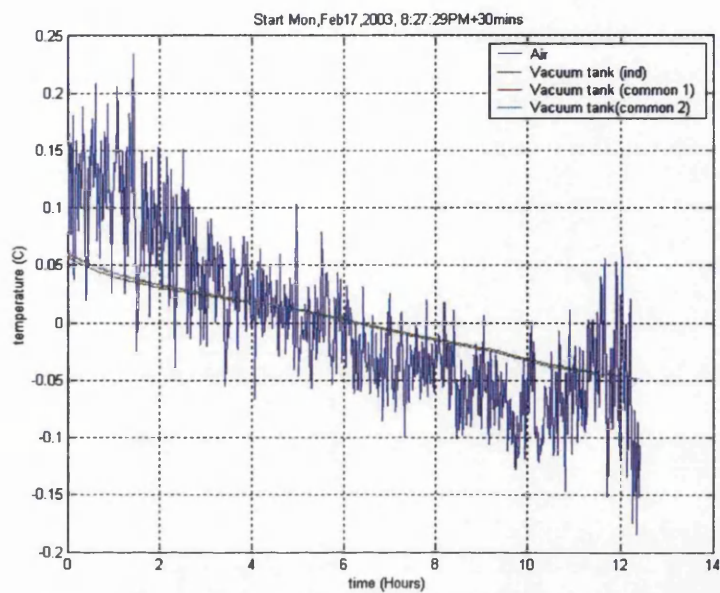


Figure 4.7: *Time series of temperature variations in the test facility.*

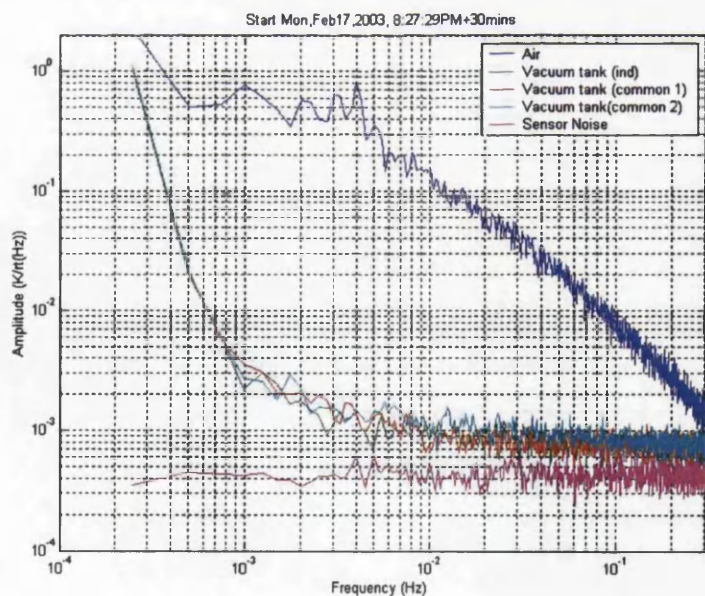


Figure 4.8: *Power spectral density of temperature variations in the test facility.*

A change in phase can be caused by a genuine change in relative optical path by movement of one of the mirrors/beamsplitters (for example due to differential expansion of the baseplate), by a refractive index change of one of the transmissive components (effectively changing the optical path length through the component) or by other, second order, effects that couple into the measurements.

The advantage of having the reference interferometer on the low expansion baseplate as well as the measurement interferometer is that all path length variations prior to the reference interferometer should be irrelevant. There are many such path length variations before the optical bench due to the laser injection bench being in air and the light traveling through fibres. This means that the phase of the interferometer outputs can be varying significantly with respect to the signals used to drive the AOMs. It could be expected that this would not be a source of degradation in performance but in practice this turned out not to be true, as described in Section 4.3.6.

### 4.3.1 Initial performance

Figures 4.9 (time series) and 4.10 (power spectral density (PSD)) show preliminary measurements of the path length stability on the optical bench compared to the LTP interferometry goal with the experimental set up shown in Figure 4.1. This data was taken with the OB in the vacuum enclosure but at atmospheric pressure.

Figures 4.11 (time series) and 4.12 (PSD) show the stability measurements with the vacuum enclosure evacuated to  $\sim 2 \times 10^{-2}$  mbar. The convection current reduction introduced by the vacuum significantly improved the stability measurement, although the noise level is clearly still above the LTP goal.

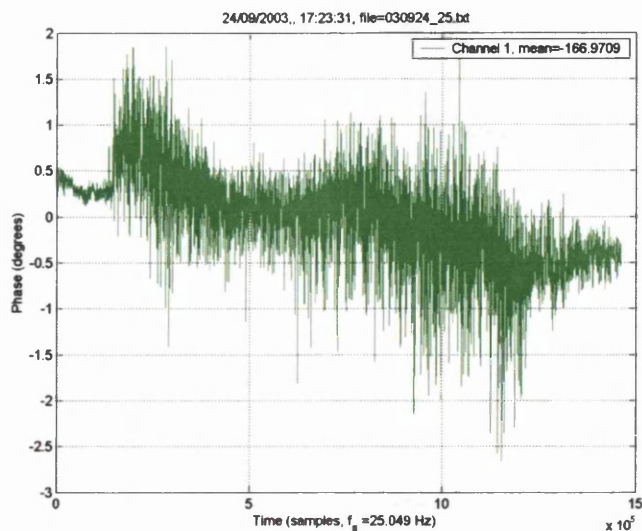


Figure 4.9: Time series showing initial noise performance of optical bench. The data was taken over 16 hours.

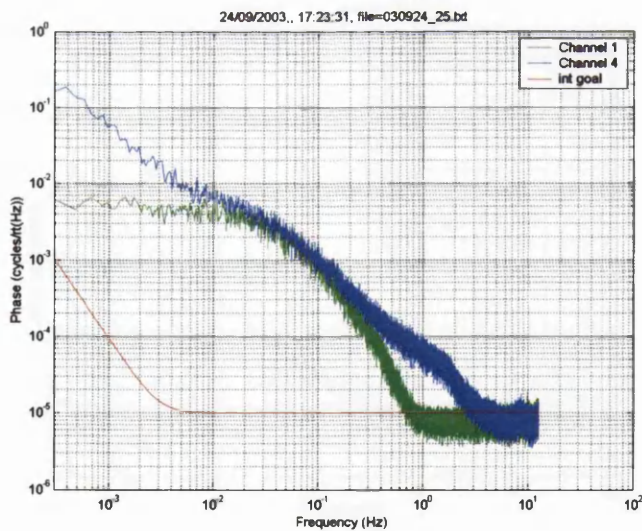


Figure 4.10: PSD showing initial noise performance of optical bench. The green curve is the measurement channel and the blue curve is the frequency noise channel. The red line is the LTP interferometry goal.

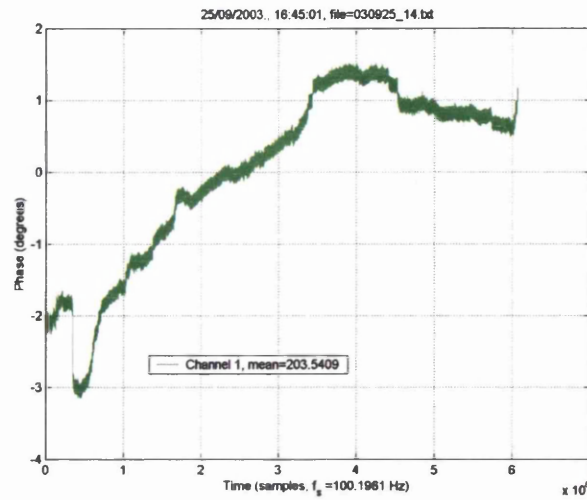


Figure 4.11: *Time series showing noise performance of optical bench under vacuum. The data was taken over 17 hours.*

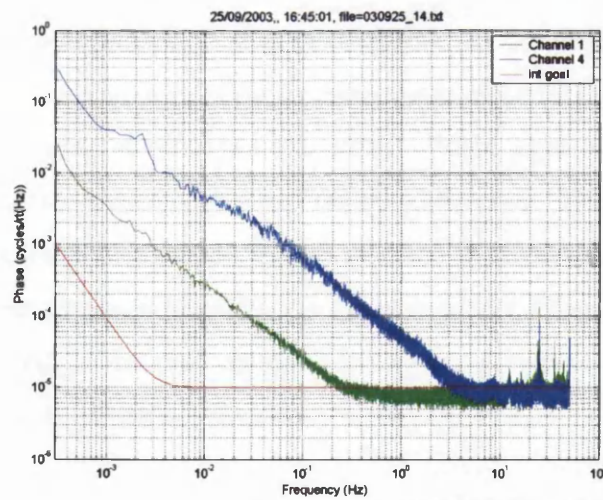


Figure 4.12: *PSD showing noise performance of optical bench under vacuum. The green curve is the measurement channel and the blue curve is the frequency noise channel. The red line is the LTP interferometry goal.*

This Section describes the investigations undertaken to identify the sources of excess noise and the experimental implementation of their removal.

### 4.3.2 Amplitude stabilisation

The laser power level in each arm of the interferometer varies due to fluctuations in laser output and variations in the transmission through the system (for example in the fibres). The prototype optical bench was designed such that the light power of the two different frequency beams can be monitored using the transmitted beams through BS8 and BS9 (as shown in Figure 3.1). In practice the beams were directed by mirrors separate to the OB to power monitor photodiodes sited outside the vacuum tank.

This light was used to stabilise the light in each arm to investigate if low frequency laser power variations were coupling into the measurement. The drive power to the AOMs was used as the actuator. AOMs work by propagating an acoustic wave through a suitable, acousto-optic, material ( $\text{TeO}_2$  in this case) resulting in an index of refraction variation. When light is incident at the Bragg angle on this ‘acoustic grating’ light is diffracted. The 1st order beam will have been frequency shifted by the  $rf$  drive frequency and the power of the shifted beam is proportional to the  $rf$  drive power. Thus, the  $rf$  drive to these modulators can be used as the actuator for power stabilisation of the light on the OB, as shown schematically in Figure 4.13.

No difference in the noise performance was seen when the amplitude stabilisation servo was in use with a gain  $> 100$  and a bandwidth of 20 kHz.

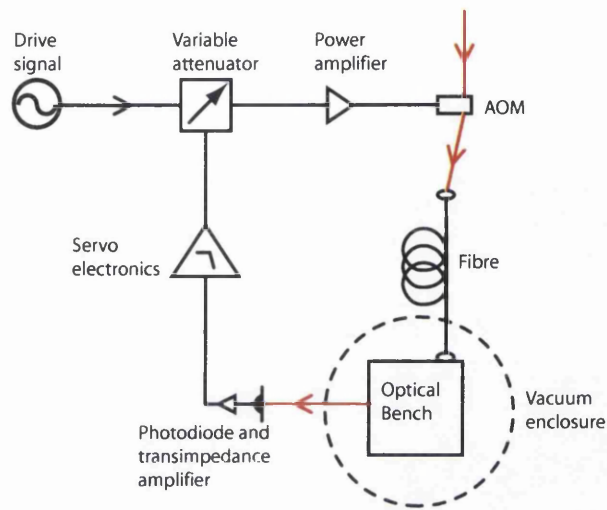


Figure 4.13: *Layout of the power stabilisation servo. Wires are denoted by black lines and laser light (of all frequencies) by red lines. Only one AOM and feedback path is shown for clarity.*

### 4.3.3 Reducing *rf* pickup

Systems handling high frequency signals can emit some of the signals if the system is not perfectly impedance matched. These signals can be picked up elsewhere in the system and mixed with other signals at any non-linear junction (for example a photodiode).

Of concern in this instance are the 80 MHz and 80.01 MHz drive signals to the AOMs. These signals are of order 1.5 W each. The mixing of one of these signals with some of the other would cause a 10 kHz signal and could appear at the measurement photodiodes. The phase of this electrical pickup 10 kHz signal may not be locked to the phase of the optical 10 kHz signal, causing an apparent phase change. This was found to be the case in the initial system and considerable effort was put into improving the *rf* shielding and impedance

matching.

One of the main improvements was the introduction of high quality cabling for all *rf* carrying signal lines, terminated with SMA connectors. The cable used was Filotex® Quickform® 86 which has a silver plated copper covered steel inner conductor separated from the outer conductor of tin soaked copper braid by a PTFE dielectric spacer. This was used as it has screening properties close to that of semi-rigid cables whilst having greater flexibility. The high power amplifiers were placed in conductive sealed tins which were grounded to reduce their radiation and reception of *rf* signals. Particular care was taken to shield the amplifiers due to the relatively large size of the signals at these points. The level of unwanted *rf* signal was reduced to  $\sim 80$  dB below that of the main signals.

#### 4.3.4 Beam size and position investigations

Investigations were undertaken to ensure that a combination of factors including beam size were not coupling into the phase measurements. Each interfering beam carries phase information and by monitoring the change in ‘net’ phase from the two beams we deduce path length changes on the optical bench. Thus if some of this information is lost there is a risk that a spurious path length change will be recorded.

If a beam is large compared with the photodiode, a significant proportion of the light may be lost off the active area of the photodiode (clipped)<sup>1</sup>. With

---

<sup>1</sup>For the prototype OB experiments single element photodiodes were used, so clipping can only occur at the photodiode active area edge. For the LTP interferometers quadrant photodiodes will be used to extract relative beam angle data. This means that this loss of information at the photodiode slits must be considered as well as edge effects.

this lost light there is an associated loss of phase information. If there was no motion in the system then this would not affect the measurement as the phase *difference* is always being measured.

For the prototype optical bench experiments the photodiodes were not rigidly mounted with respect to the optical bench, potentially resulting in large jitter of the interfering beams with respect to the edge of the photodiode.

For the ideal case of perfectly overlapping beams whose wavefronts are matched, beam clipping and jitter could occur with no effect on the net phase. However, if we take the example of flat interfering wavefronts but with an angle between them, then this is not the case. Figure 4.14 shows two beams with plane wavefronts (wavefront 1 and wavefront 2) viewed orthogonally to the direction of propagation. If both wavefronts were in the same orientation as wavefront 1 (which has been arbitrarily designated 'zero' phase) then it is clear that the clipping due to beam jitter would have no effect on the measured phase. However, with this angular tilt between the two beams as shown the phase does change with beam jitter: with the photodiode active area clipping in position 1 the net phase is 'negative' but when the beam moves across the photodiode to position 2 the net phase is zero.

The magnitude of beam jitter was measured using a scanning knife edge beam analyser in place of the photodiodes. The measurement precision was limited by the analyser noise but placed a conservative upper limit to the spectral density of beam jitter of  $< 20 \mu\text{m}/\sqrt{\text{Hz}}$ .

Whilst some care was taken to achieve well matched beams with good alignment and overlap, the main defence against beam jitter and beam size coupling into the noise measurement was to use large area photodiodes. The idea being that provided all the light stayed on the photodiodes then relative beam tilts,

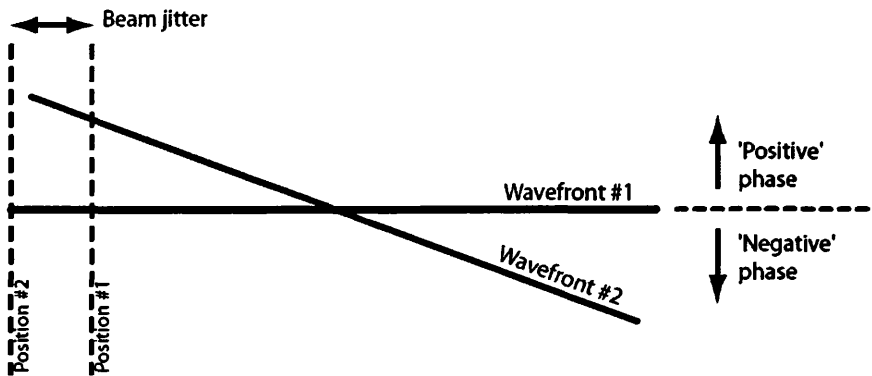


Figure 4.14: *Diagram showing effect of beam jitter on measured phase at photodiode.*

curvatures and overlap would become irrelevant.

The design of the bench allowed for a maximum misalignment of the two interfering wavefronts of  $\frac{\lambda}{10}$  over the beam at the recombination point (where the beam radii were  $\sim 1.5$  mm). This gives an angular misalignment of the two phase fronts of  $67 \mu\text{rad}$ .

The photodiodes used had square active areas of side 6.4 mm. The beam diameters at the photodiodes are shown in Table 4.1, where the beam diameter is defined as beam width at  $\frac{1}{e^2}$  of the maximum intensity. Beam 1 and 2 refer to the two different frequency interfering beams.

Table 4.1: Beam diameters (in  $\mu\text{m}$ ) at output photodiodes.

	Reference	Measurement	Frequency noise
Beam 1	1560	1800	1580
Beam 2	1940	2270	2325

The apparent longitudinal motion induced by the clipping shown in the sim-

plified 1-D case shown in Figure 4.14, assuming uniform beam intensity, is the product of the photodiode radius (3.2 mm), the angle between the wavefronts ( $67 \mu\text{rad}$ ) and the ratio of beam displacement to photodiode size. This also assumes that the beam jitter acts completely in the measurement band. This results in a worst case expected spurious longitudinal signal of  $6.7 \times 10^{-10}$  m, which is significantly above the desired noise contribution of  $1 \times 10^{-12}$  m.

The assumption that the beams have uniform intensity profiles is far from realistic. The beams will have a Gaussian profile which will have low intensity at the beam wings, resulting in the clipping of the phase fronts having less of an impact than calculated above. From [59] we know that an ideal Gaussian beam of radius  $w$  passing through an aperture of radius  $a$  has a normalised transmitted power of

$$P = 1 - e^{-(2a^2/w^2)} . \quad (4.3)$$

So, an active area three times the beam diameter would give a fractional power loss  $e^{-18}$ . An active area of only twice the beam diameter would give a fractional power loss of  $e^{-8}$ . This is, of course, provided the beam is well centered.

The largest beam diameter is 2.33 mm and so a results in a minimum fractional power loss of  $\sim e^{-15}$ . This can be factored into the calculation of spurious longitudinal signal, giving a factor  $\sim 10^{-7}$  reduction of the effect for this more realistic model, suggesting that if the beam is well centered on the photodiode then the magnitude of jitter seen will not add excess noise to the measurement.

The approach adopted was to mount the photodiodes on translation stages with  $10 \mu\text{m}$  resolution in both axes orthogonal to the direction of beam propagation. This allowed very accurate centering of the beams on the photodiodes.

The stability was also measured with lenses in each of the output beams (im-

mediately before the photodiodes), despite this introducing the possibility of multiple reflection stray light induced noise. The advantage was that the beam sizes were much smaller than the photodiodes with the lenses in place. No difference was seen with or without the lenses and consequently all subsequent tests were conducted without lenses.

To further investigate the effect of the  $< 20 \mu\text{m}/\sqrt{\text{Hz}}$  jitter on the phase of the heterodyne signal one output beam was split onto two photodiodes. This guarantees a common optical signal on the two photodiodes and the phase difference measurement will be one of the phase measuring system noise floor. Using one photodiode signal as a reference, the other photodiode was moved across the beam in  $\sim 130 \mu\text{m}$  steps every five seconds. These scans were taken in both directions orthogonal to beam propagation and a typical result is shown in Figure 4.15.

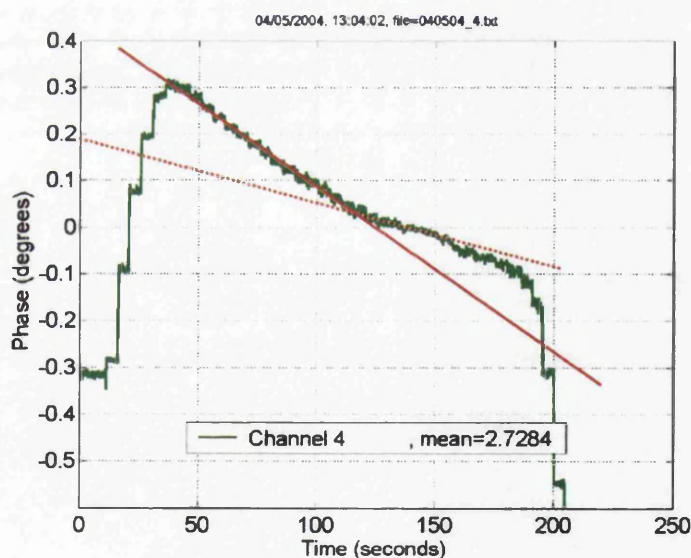


Figure 4.15: *Apparent phase change as a photodiode is moved across an output beam.*

The effect of beam clipping can be seen at the extremes of the plotted data

(the green line). The superimposed lines drawn on the graph correspond to gradients (ratio of apparent path length change to beam movement on the photodiode) of  $0.42 \text{ pm}/\mu\text{m}$  (solid line) and  $0.15 \text{ pm}/\mu\text{m}$  (dashed line). If we assume a typical gradient over the photodiode of  $0.3 \text{ pm}/\mu\text{m}$  then the beam jitter would have to be at least  $30 \mu\text{m}/\sqrt{\text{Hz}}$  (at the measurement frequency) to bring the noise floor to the  $10 \text{ pm}/\sqrt{\text{Hz}}$  target level. This indicates that this is not a limiting noise source.

### 4.3.5 Frequency noise

Frequency (or phase) noise arises due to variations in the ‘absolute’ frequency of the laser. This can couple into the phase of the interferometer output if the path lengths are not matched, as described in Section 2.2.2.

The pathlengths of the measurement interferometer were designed to be equal but build tolerances might result in a path length difference of a few mm. A third interferometer was also included on the OB with large path length difference: the frequency noise interferometer has a path length difference of  $\sim 300 \text{ mm}$ . Laser frequency noise dominates the output of this interferometer and so it can be used to measure the frequency noise. This signal can be used either to subtract the effects of laser frequency noise from the data or as the error signal for a laser frequency stabilisation servo.

#### Path length difference calibration

In order to subtract the effects of laser frequency noise we need to measure the path length difference in the reference interferometer. To do this the laser frequency was modulated at  $1 \text{ Hz}$  by applying a voltage to the piezo-electric

crystal glued to the laser crystal. This produced a signal at the modulation frequency in the measurement and frequency noise interferometer outputs according to Equation 2.5, as shown in Figures 4.16 (time series) and 4.17 (PSD).

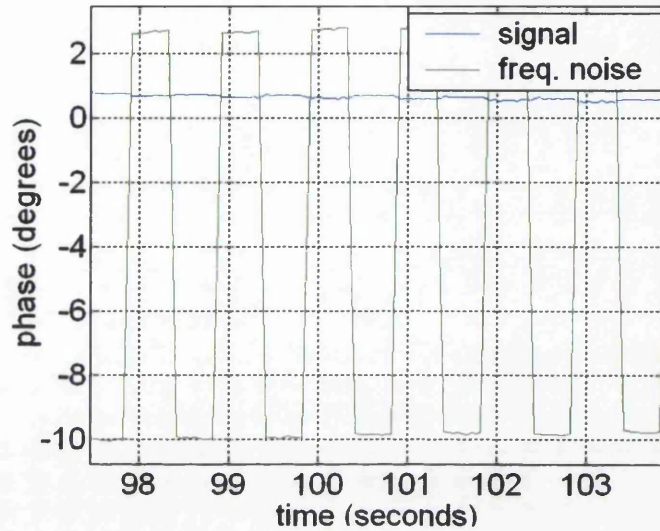


Figure 4.16: *Times series plot showing effect of 1 Hz modulation of laser frequency on measurement and frequency noise output signals.*

From Equation 2.5, the relative size of these signals gives the ratio of frequency noise coupling between the two channels as

$$\frac{\Delta x_{meas}}{\Delta x_{fnoise}} = \frac{\delta x_{meas}}{\delta x_{fnoise}}, \quad (4.4)$$

where  $\Delta x$  is again the path length difference and  $\delta x$  the apparent path length change due to laser frequency variation. The subscript 'meas' refers to the measurement paths and the subscript 'fnoise' refers to the frequency noise paths.

From the PSD shown in Figure 4.17 we have the ratio

$$\frac{\Delta x_{meas}}{\Delta x_{fnoise}} = \frac{0.4}{60} \quad (4.5)$$

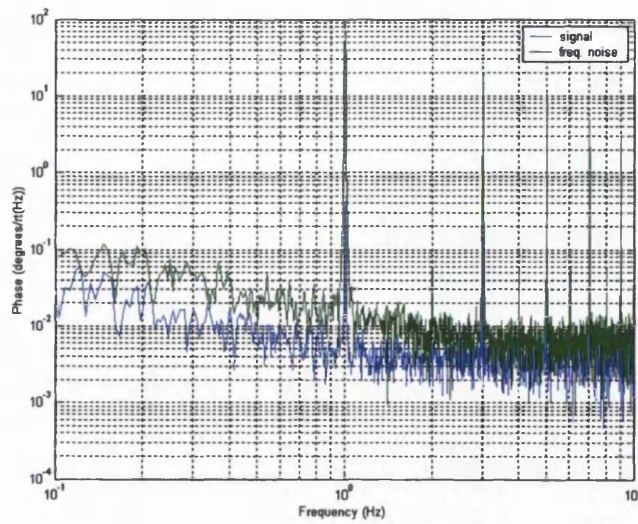


Figure 4.17: Phase spectral density plot showing effect of 1 Hz modulation of laser frequency on measurement and frequency noise output signals.

and as we know that  $\Delta x_{f_{noise}}$  is 0.3 m, we can calculate  $\Delta x_{meas}$  as 2 mm. This is a realistic value for construction of an interferometer using the techniques described in Chapter 3.

### Laser frequency noise subtraction

We can now use the knowledge of  $\Delta x_{meas}$  to subtract the effect of laser frequency noise from the measurement data. The result of processing the data in this way is shown in Figure 4.18.

The measurement of laser frequency noise can also be used to stabilise the laser frequency. This approach was implemented using the phase difference between the reference and frequency noise signals as an error signal. The error signal (after amplification and filtering) was fed back to the laser piezo-electric crystal (for the higher frequencies) and laser crystal temperature control (for low

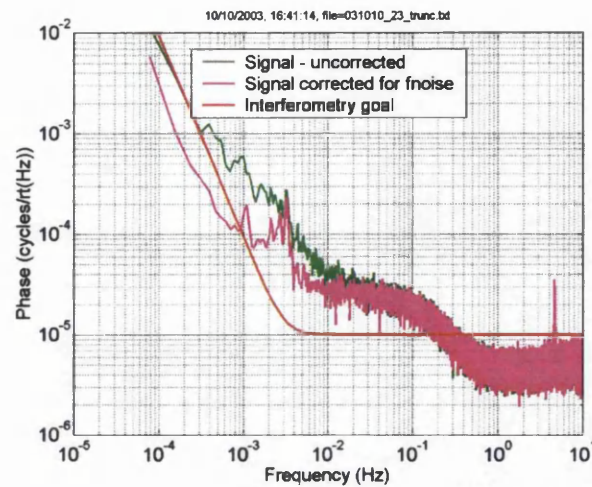


Figure 4.18: *Phase spectral density plot showing noise performance of the prototype optical bench with and without frequency noise correction. The red line is the LTP interferometry goal. The residual noise bulge above the interferometry goal is due to noise sources that had not been identified at that time.*

frequencies) to stabilise the laser frequency. The servo system had a bandwidth of 800 Hz and a gain of  $\sim 10^3$  at 1 Hz.

Figure 4.19 shows the apparent path length stability of the prototype optical bench showing very similar performance to that obtained using laser frequency noise subtraction. Note that in this test a frequency modulation applied to the laser at 0.8 Hz. The 0.8 Hz modulation signal with its sidebands is apparent in the plot of the frequency stabilised noise performance. Frequency noise subtraction of this data removes these spikes but does not change the rest of the noise curve. This shows that either system could be implemented to remove laser frequency noise effects and that the system is now limited by something other than laser frequency noise.

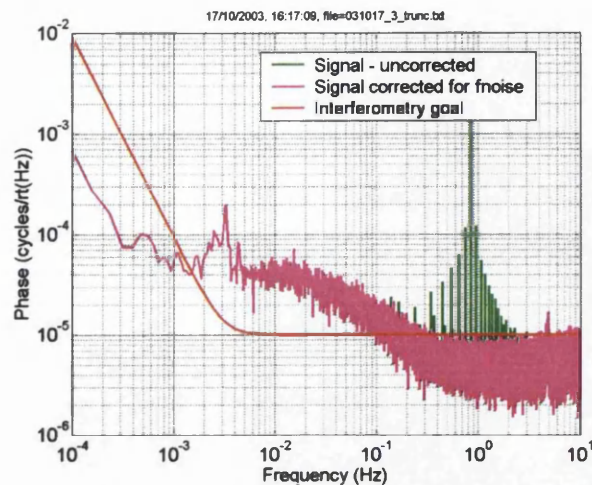


Figure 4.19: *Phase spectral density plot showing noise performance of the prototype optical bench with frequency stabilisation servo implemented. The green curve exhibits the frequency modulation spikes, which are removed by frequency noise subtraction (magenta curve). The red line is the LTP interferometry goal.*

#### 4.3.6 Fibre noise investigations

The phase difference of interest from a distance measurement perspective is between the outputs of the measurement interferometer and the reference interferometer. The signals that generate the 10 kHz beatnotes originate from two phase locked signal generators at 80 MHz and 80.01 MHz. These drive (*via* power amplifiers) the AOMs on the injection bench that frequency shift the light. An additional 10 kHz signal is generated by another phase locked oscillator.

The phase variation between the optical outputs and this electrical 10 kHz is large. This is expected as the free space beams are subjected to differential path length changes caused by traveling through different AOMs, having different paths through air and traveling through different fibres before they get

to the stable optical bench. All of these effects will now be referred to as 'fibre noise.'

The phase difference between signals of optical and of electrical origin was anticipated but was expected to be common mode between the reference and other interferometers (due to the reference interferometer also being on the stable OB). To try and identify the remaining excess noise in the stability performance this phase difference was reduced.

#### Path length stabilisation by piezo actuator

The initial method of locking the electrical phase to the optical phase was to place a mirror before one of the fibres (between injection bench and optical bench) on a piezo actuator. The actuator had a range of  $100\ \mu\text{m}$  and is shown in Figure 4.20. The other beam remained unchanged as the piezo actuator has sufficient range to stabilise the path lengths. The error signal for the feedback loop was the phase difference between the electrical and reference optical heterodyne signals.

The noise performance of the optical bench with laser frequency and path length stabilisation servos operating is shown in Figure 4.21. The noise now meets the LTP interferometry goal over the whole frequency band of interest apart from some remaining excess noise in the mHz region. This noise has the same spectral shape as the temperature fluctuations in the laboratory at the time of data taking (shown in Figure 4.22). Further data runs were taken and different temperature variations were seen but the excess noise in the performance measurement always followed the temperature variations (this is discussed further in Section 4.3.9). The peak in temperature variations around the mHz region is due to the laboratory temperature control having a

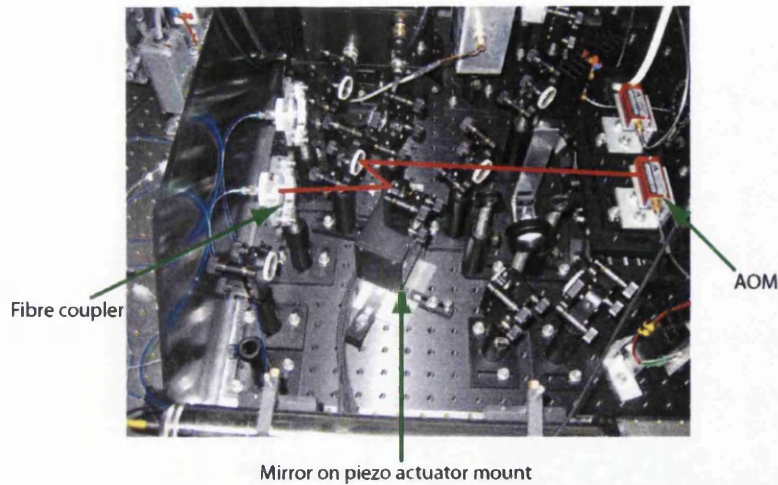


Figure 4.20: *Photograph of the piezo mounted mirror for path length stabilisation. The beam path is indicated by a red line.*

heating/cooling cycle of  $\sim 5$  minutes.

### Why path length stabilisation is needed

By measuring the measurement optical heterodyne signal with respect to the reference optical heterodyne signal it was thought that the intrinsic optical bench stability would be seen - even though both signals would be varying with respect to the electrical signals that drive the AOMs. In practice this was only the case when the optical signal was stabilised with respect to the electrical signals.

For the effect seen to occur there must be a signal with the phase of the electrically generated signal present on the light at the measurement photodiodes. This results in a signal (at the heterodyne frequency) whose phase is uncorrelated with the phase of the optical signals. This can be considered as a small vector with varying phase dragging the phase of the 'stationary' optical signal,

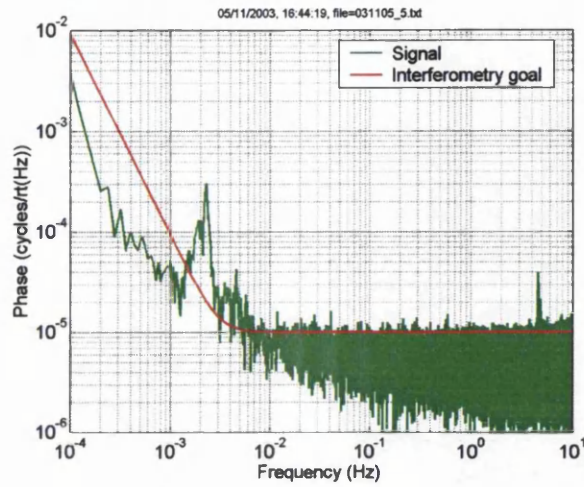


Figure 4.21: PSD showing noise performance of the optical bench with the piezo mount path length servo in operation. The red line is the LTP interferometry goal.

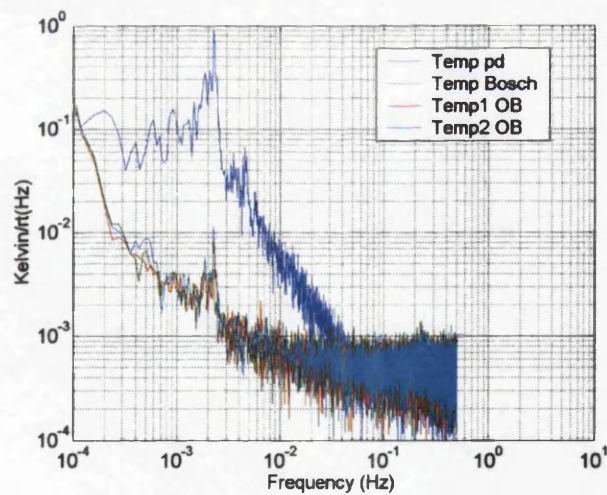


Figure 4.22: Temperature spectrum during the data run shown in Figure 4.21. The larger variations are from a sensor mounted on a measurement photodiode and the other three curves are from sensors mounted inside the vacuum tank.

as shown in Figure 4.23.

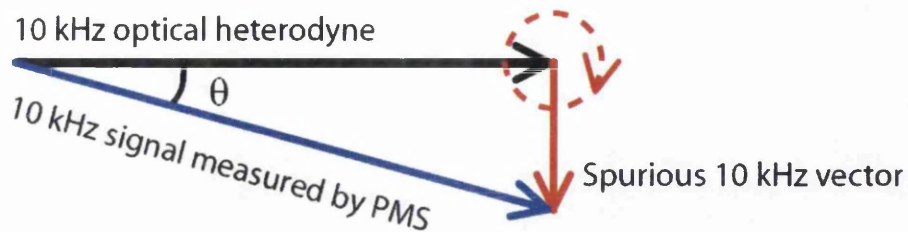


Figure 4.23: Diagram showing how a small vector at the heterodyne frequency of varying phase can influence the optical phase measurement.

Here the vector is shown  $\pi/2$  out of phase with the optical signal. This would not effect the noise measurement as the phase measurements are not against an absolute reference, *i.e.* a static phase offset is innocuous. When the phase of this vector changes, however, there will be a resulting signal coupled into the measurement leading to changes in the apparent phase of the optical heterodyne signal and the potential for excess noise in the final measurement.

Thus, by locking the optical signal to the electrical signal the phase measurement includes the offset due to the small spurious vector but the noise performance will not be affected by it.

#### Possible origins of the spurious 10 kHz vector

Direct electrical interference into the photodiode front ends was excluded after careful investigation. However, electrical cross-talk of *rf* signals resulted in each AOM being driven by a small amount of *rf* signal intended for the other AOM. This manifested as a 10 kHz beat in the light from a single AOM that was  $\sim 90$  dB below the main heterodyne signal size. Despite considerable effort it did not seem to be possible to reduce this coupling significantly in our experimental configuration.

We observed amplitude modulation of the diffracted light at the AOM drive frequency and multiples thereof. While in principle these signals should not produce a 10 kHz beat signal, undesired non-linearities in the photodiode front ends could allow the generation of spurious 10 kHz components.

Following the Glasgow experiments it became obvious that active fibre path length stabilisation would have to be incorporated into LTP. However it was felt that further study of the small vector problem was also warranted and this has since been undertaken in a study led by colleagues at the Albert Einstein Institute in Hannover. As part of these further investigations a study of beatnote production as a function of amplitude of *rf* signals at an AOM was carried out; this is presented in Appendix C. A report on the overall study can be found in [60].

### Path length stabilisation by fibre heaters

Whilst the piezo actuation method for path length stabilisation worked well, it was unclear at the time that a piezo could be flown on board LTP. Consequently a different method of varying the path length in the fibres was investigated.

Both fibres had 30 cm of Nichrome heater wire coiled around them and were heated above ambient temperature (so that they could be driven differentially). Figure 4.24 shows a section of one of the fibres.

A similar control system to that employed for the piezo feedback loop was used to stabilise the path lengths using the fibre heaters. The noise performance was similar to that for the piezo actuated path length stabilisation, even though the bandwidth and gain of the fibre heater servo are lower than for the piezo mounted mirror. The noise sensitivity is shown in Figure 4.25 with the tem-

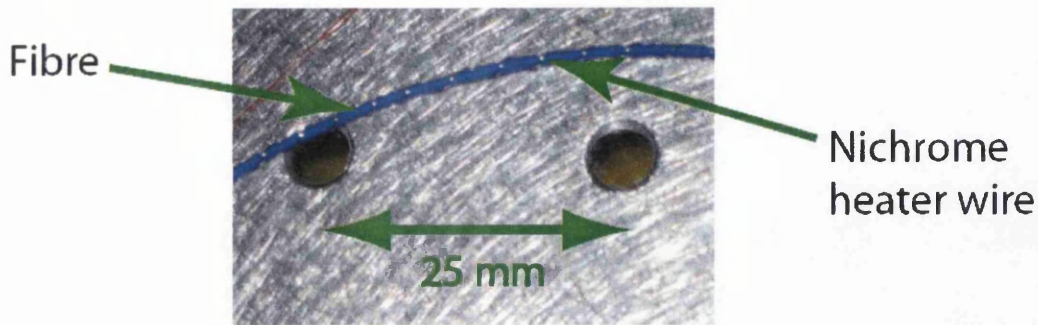


Figure 4.24: Photograph of a section of fibre with heater wire. The wire is insulated from the optical table by a sheet of acetate.

perature variation during the run shown in Figure 4.26, showing that either stabilisation system is suitable for mitigating the effects of the ‘little vector’ noise source.

### 4.3.7 Tests with a prototype LTP style phasemeter

The prototype optical bench stability was also measured using a prototype LTP AOM unit (developed by Contraves) and an LTP style phasemeter (developed by AEI, Hannover). This equipment is described in [46].

The performance with the LTP style phasemeter is shown in Figure 4.27. The performance is similar at low frequencies where the performance of the optical bench is the limiting factor and better in the 0.1 to 3 Hz range due to the lower quantisation noise of this phasemeter.

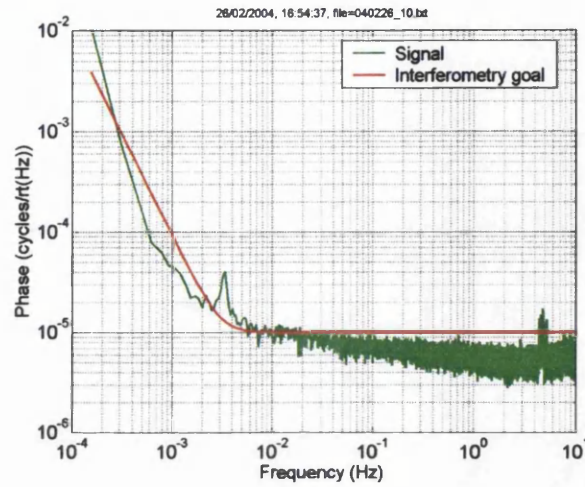


Figure 4.25: PSD showing noise performance of the optical bench with the fibre heater path length servo in operation. The red line is the LTP interferometry goal.

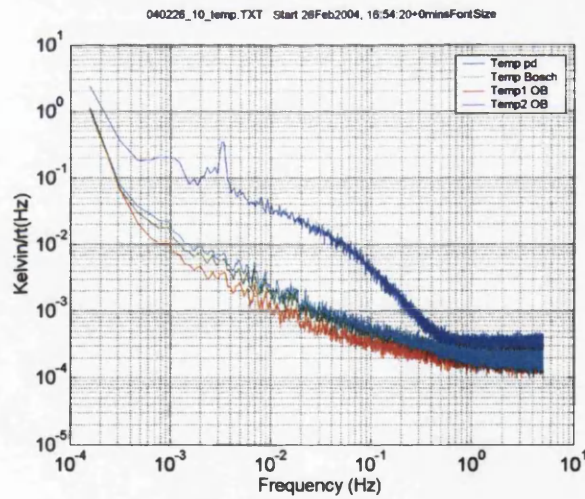


Figure 4.26: Temperature spectrum during the data run shown in Figure 4.25. The larger variations are from a sensor mounted on a measurement photodiode and the other three curves are from sensors mounted inside the vacuum tank.

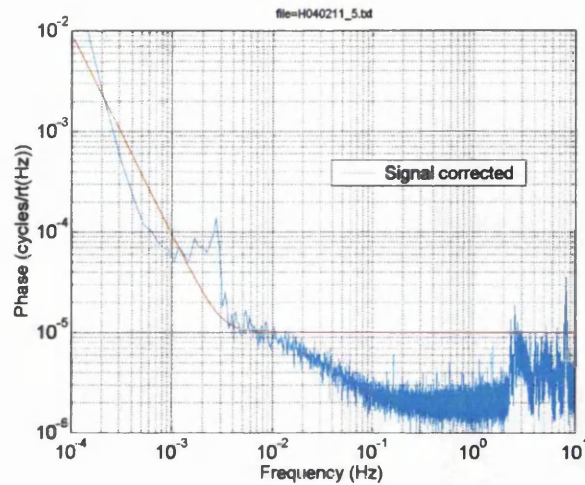


Figure 4.27: PSD showing noise performance of the optical bench with the piezo mounted mirror path length servo in operation, the LTP prototype AOM unit and LTP style phasemeter. The red line is the LTP interferometry goal.

#### 4.3.8 Noise performance using quadrant photodiodes

The measurement photodiodes for LTP will be quadrant photodiodes to allow simultaneous readout of test mass angular position. However this means that some of the phase information is lost due to the presence of the thin strips between the quadrants. This can have a similar effect to beam clipping in coupling beam jitter to apparent path length noise, as described in Section 4.3.4.

The performance of the prototype optical bench was tested using a quadrant photodiode in place of the single element photodiode for the reference measurement. The four quadrants were summed to act as a single element photodiode.

The noise level achieved was  $\sim 100 \text{ pm}/\sqrt{\text{Hz}}$ , much worse than for the single element diode. This is probably due to a combination of beam jitter and the lost phase information from the unmeasured area between the quadrants. In this case the quadrant photodiodes are mounted outside the vacuum tank and

the prototype optical bench is inside, so there will be much greater beam jitter than in LTP where the photodiodes are mounted on the optical bench.

#### 4.3.9 Identifying temperature dependency

The apparent strong correlation between temperature and phase around 3 mHz was investigated. The experiments on the prototype optical bench were conducted with the optical bench in a temperature stabilised environment, but the temperature stability on LTP is expected to be at least two orders of magnitude quieter than in the test facility [2].

In order to track down the thermally sensitive apparatus a series of tests was carried out. The first items eliminated were the phasemeter and associated filters and comparators which were tested and found to be suitably temperature stable.

Three other main areas were tested for thermal sensitivity: the photodiodes, fibre injectors and optical bench. This was done by heating the local area (using a resistor for the photodiodes and small lamp bulbs for the photodiodes and optical bench) at a known modulation frequency (suitably low such that thermal time constants did not prevent significant temperature change of the device under test). The performance of the system was then measured and inspected for a change in apparent path length stability at the modulation frequency.

While the heating elements and temperature monitors were as closely coupled to the device under test as possible, there remains an unquantified error in the actual component temperature variations. As a result of this these results should be taken as estimates.

### Photodiode thermal sensitivity

The photodiodes are subjected to the largest temperature variations of the investigated components as they are situated outside the vacuum enclosure and so do not benefit from the passive thermal isolation of the vacuum tank.

Figure 4.28 shows the apparent path length stability when the reference photodiode was heated using a  $33\ \Omega$  resistor driven by a  $5\ V_{p-p}$  square wave at 3 mHz. The temperature spectrum is shown in Figure 4.29. The blue curve (monitoring the temperature of the photodiode) clearly shows the temperature modulation.

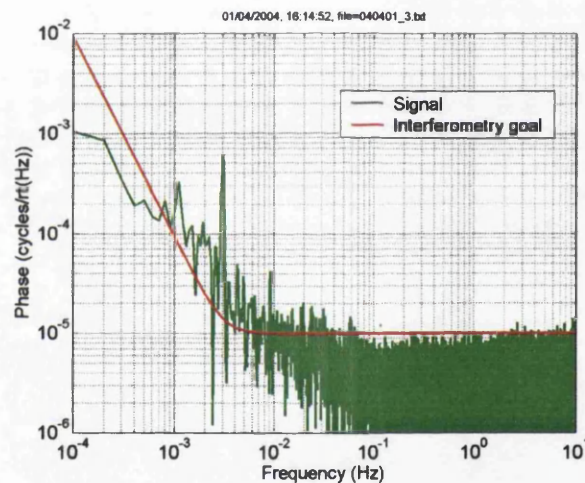


Figure 4.28: *PSD showing apparent path length stability of optical bench with reference photodiode being heated at 3 mHz.*

The measured coupling of apparent path length change to thermal variation was  $\sim 3 \times 10^2$  pm/K. This is likely to be a significant over estimate, though, as all three photodiodes are situated close together and therefore experience very similar temperature environments resulting in some of the temperature response being common mode.

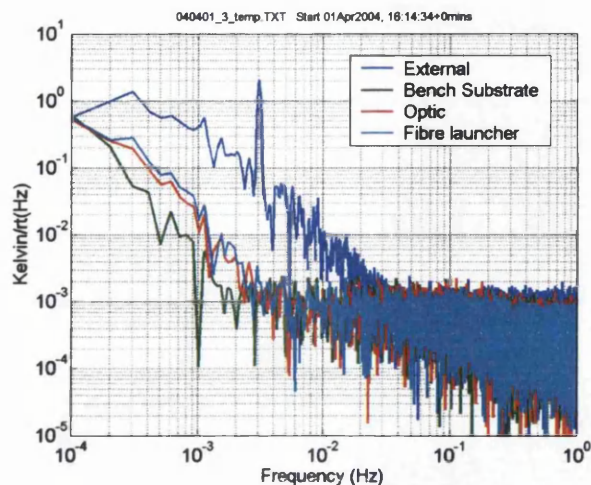


Figure 4.29: *Temperature spectrum during the data run shown in Figure 4.28. The blue (top) curve shows the temperature spectrum as measured at the reference photodiode.*

This was repeated at 1 mHz and the coupling factor was found to be similar.

### Fibre injector thermal sensitivity

The fibre injectors could couple temperature variations into the apparent path length measurement by imparting an angular movement on the beam. Small filament bulbs were placed close to the fibre injector mounts to test the thermal sensitivity, a photograph of the set up is shown in Figure 4.30 and the result of the thermal modulation are shown in Figures 4.31 (PSD) and 4.32 (measured thermal spectrum). These plots show three different modulation frequencies from three independent sets of heaters, heating different areas of the optical bench.

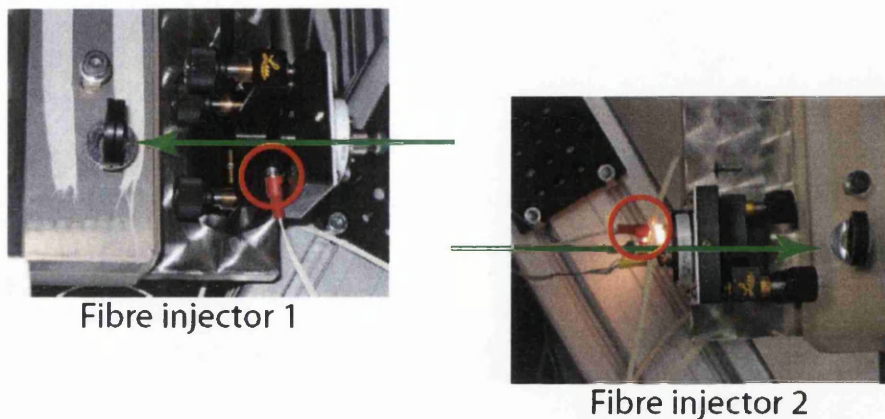


Figure 4.30: Photograph of the fibre injector heaters. The superimposed green arrows indicate direction of light through the fibres onto the optical bench and the heaters are circled in red.

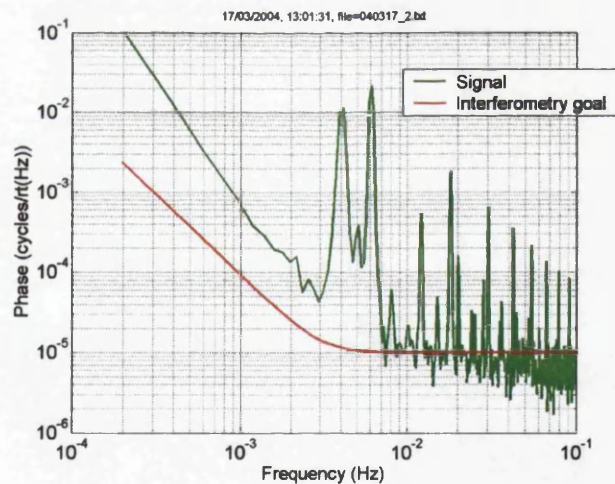


Figure 4.31: PSD of apparent path length difference whilst temperature modulating areas of the optical bench. The main bench was heated at 4 mHz, fibre injector mount 1 at 5 mHz and BS7 at 6 mHz.

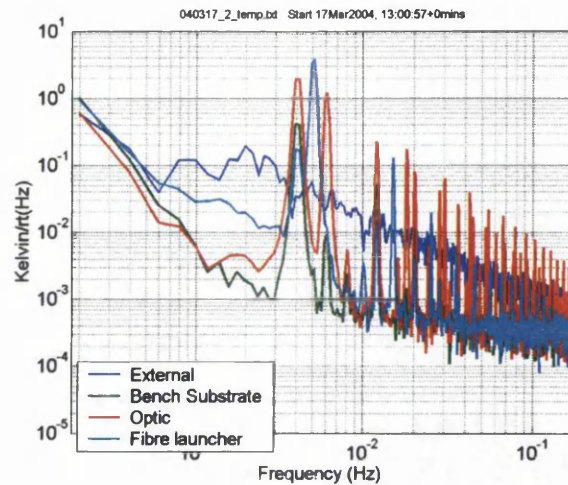


Figure 4.32: *PSD of measured temperature variations during temperature modulation of the optical bench during the run shown in Figure 4.31.*

#### Optical bench thermal sensitivity

Thermal variations on the optical bench itself could couple into the apparent path length measurement in two ways: physical expansion of the ULE® baseplate material altering component separation and changes in optical path length in transmissive components (a combination of both physical length changes and change in refractive index).

For these effects to couple in to the path length measurement they would have to act differentially between the interferometer paths and so in practice we would expect the impact to be significantly reduced by their common mode nature.

A photograph of the heater positions on the optical bench is shown in Figure 4.33. The nine heaters above the optical bench substrate are  $\sim 5$  cm above the ULE® surface. A PSD of the apparent path length stability of the optical bench when just the nine substrate heaters were in operation (at 8 mHz)

is shown in Figure 4.34 with the measured temperature spectrum shown in Figure 4.35.

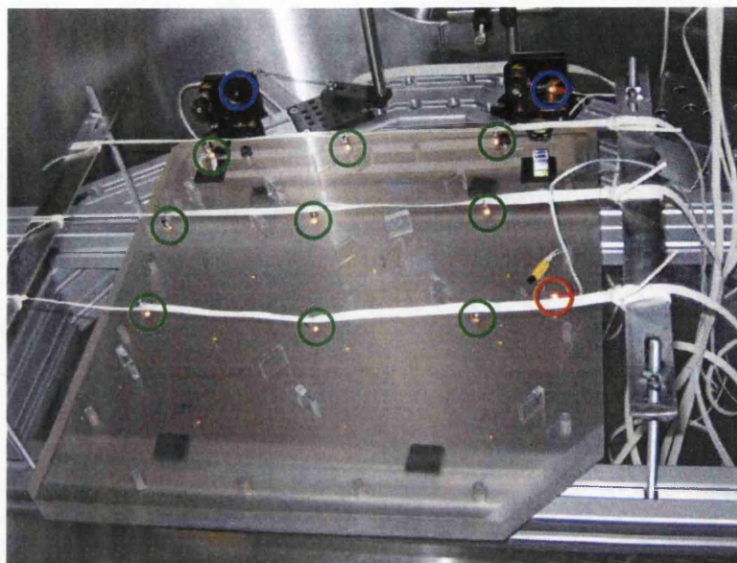


Figure 4.33: *Photograph of the prototype optical bench in the vacuum enclosure with heaters. The bulk optical bench heaters are circled in green, the fibre injector heaters in blue and the individual component heater in red.*

#### Discussion of thermal sensitivity investigations

The first thing to note from the temperature and phase measurements is that there is significant cross coupling between thermal modulation of different areas of the bench. This is due to difficulties in locally heating individual areas and also in measuring the temperatures accurately. This reinforces the caveat that these results are indicative only.

From Figures 4.31 and 4.32 the effect on apparent path length stability due to thermal variations of various components can be estimated:

- Substrate  $\sim 2.5 \times 10^4$  pm/K,

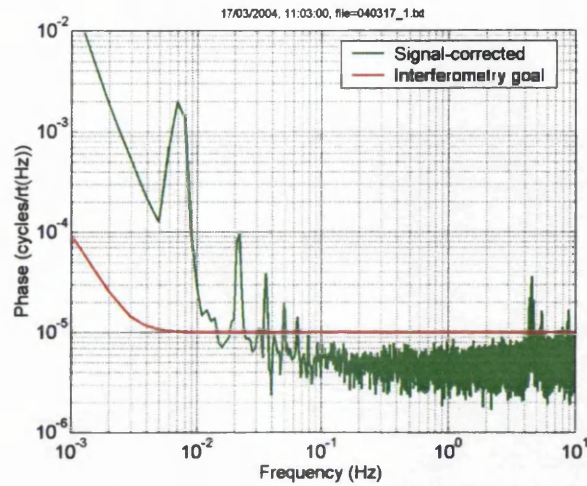


Figure 4.34: *PSD of apparent path length difference whilst temperature modulating the optical bench 'uniformly' at 8 mHz.*

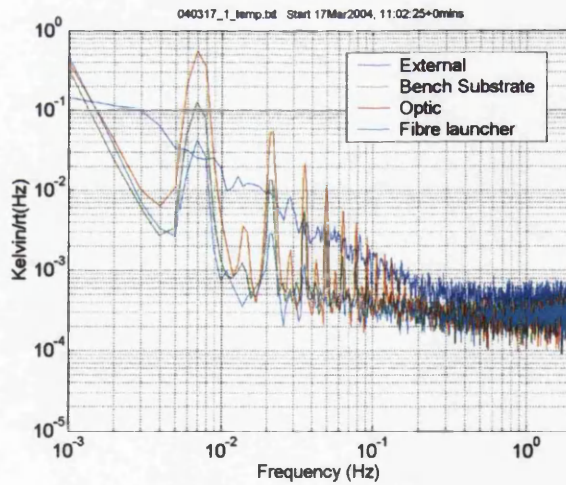


Figure 4.35: *PSD of measured temperature variations during temperature modulation of the optical bench during the run shown in Figure 4.34.*

- Fibre coupler  $\sim 100$  pm/K,
- Individual transmissive component  $\sim 2 \times 10^4$  pm/K.

Figures 4.34 and 4.35 also suggest a coupling of around  $2 \times 10^4$  pm/K for the substrate.

From these results we estimate that a temperature stability of  $\sim 5 \times 10^{-4}$  K/ $\sqrt{\text{Hz}}$  would easily allow the target path length stability of 10 pm/ $\sqrt{\text{Hz}}$  to be achieved. The expected temperature fluctuations experienced by the optical bench at the mechanical interfaces are  $< 10^{-4}$  K/ $\sqrt{\text{Hz}}$ , from 1-30- mHz ([2], requirement OMS-7.2.5-3) and as such are more than compatible with this upper limit.

The evidence that temperature variations can affect the apparent path length stability provide an explanation of the residual noise in the sensitivity curves (such as Figure 4.21), whose spectral features coincide with those of the temperature variations during measurements. The most likely route by which the thermal variations couple in to the apparent path length stability is *via* a combination of the substrate and optical components of the optical bench and the measurement photodiodes. The substrate and optical components have similar levels of coupling to temperature noise while the photodiodes have a much weaker coupling. However the photodiodes are in a less stable thermal environment. The net result is that both have similar effects on system performance.

## Chapter 5

# LISA Pathfinder engineering model optical bench construction

The lessons learned in designing, constructing and testing the prototype optical bench were applied in the building of the LTP engineering model (EM) optical bench. This bench was built at the Rutherford Appleton Laboratory in Oxford with on-site support from the University of Glasgow and the Albert Einstein Institute, Hannover.

This chapter looks at the progression from prototype optical bench to EM construction, with reference to the links between the two.

## 5.1 Design goals

The prototype optical bench was built to prove the intrinsic stability of quasi-monolithic optical benches. The EM was built to demonstrate the applicability of this type of optical bench for the LTP mission.

The major differences for the LTP OB are that light leaves the baseplate to reflect off external mirrors and that it includes an extra interferometer. This leads to a more complicated layout, but the principles of construction and operation are the same as for the prototype optical bench.

The optical design of the LTP OB has four interferometers: a reference, a frequency noise, one that measures one test mass position with respect to the OB and one that measures the position of the test mass separation. The nominal beam paths are the same as for the planned flight model shown in Figure 2.6. The specific EM optical prescription is described in [61].

The LTP interferometer is to measure the position of the test masses to  $10 \text{ pm}/\sqrt{\text{Hz}}$  but first it must withstand launch vibrations and eventually operate in the LTP Core Assembly (LCA) environment.

The EM OB was similar in design to the planned LTP flight model but there were aspects that will not be seen in the final version. These were not constructed in a representative manner due to time constraints. Further studies prior to the flight model construction were planned in order to develop the technological shortfalls (described in Chapter 6).

## 5.2 Size and component density

The baseplate face on which the mirrors and beamsplitters are bonded is smaller than the prototype optical bench area and the components are more densely populated. This raises issues that were dealt with in the design phase, namely an increased danger of beam clipping and a more restricted working volume for component placement. One consequence of this was the design of the adjusters used for component placement, shown in Figure 5.1. It can be seen that these adjusters are significantly different to those used in the construction of the POB and this is discussed in Section 5.4.

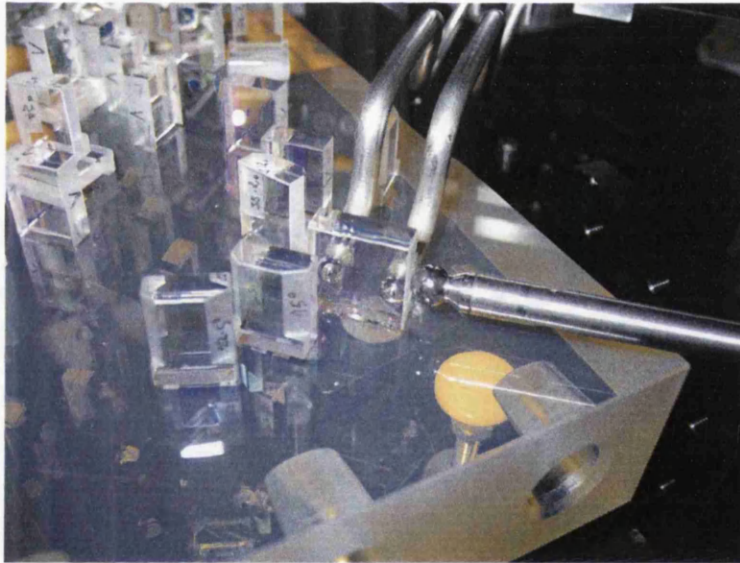


Figure 5.1: *The adjustable arms used to position components prior to bonding (photograph courtesy of CCLRC Rutherford Appleton Laboratory).*

The smaller area in which the components can be placed is a consequence of mass and volume restrictions in the spacecraft. The baseplate is thicker than the prototype optical bench baseplate due to the added strength needed for launch and to allow for the inserts which join the OB to the rest of the experiment.

## 5.3 Fibre injectors

The fibre injectors for the EM needed to be attached to the Zerodur® baseplate in order for the interferometers to remain aligned after shake testing. The solution adopted was to use common off the shelf parts. These were not flight qualified but had the potential to become so with qualification testing and any resulting redesign.

The fibre injectors were off the shelf Shaeffer and Kirchoff model 60FC-4-A6.2-03 [62], shown in Figure 5.2. A base was glued to the Zerodur® onto which the fibre injectors were clamped. The alignment strategy was to use shims between the fibre injectors and the baseplate to adjust the height and angle of the optical beams. The shims were iteratively machined to achieve the desired alignment. This proved to be a relatively course alignment procedure with the limited level of development possible in the time restricted programme. Measurements taken after construction of the OB was complete indicated that positioning and alignment to within  $100\ \mu\text{m}$  and  $100\ \mu\text{rad}$  of the nominal values was achieved.

Another issue with the EM fibre injectors was the materials used in their construction. There are strict limits on the magnitude of magnetic moment generated by the materials on LTP in order to avoid the test masses being disturbed by magnetic fields. Items in close proximity to the test masses have to be particularly magnetically clean. Thus the EM fibre injectors are not allowable for the flight model, but custom injectors to a similar design could have been made using non-magnetic materials (such as titanium).

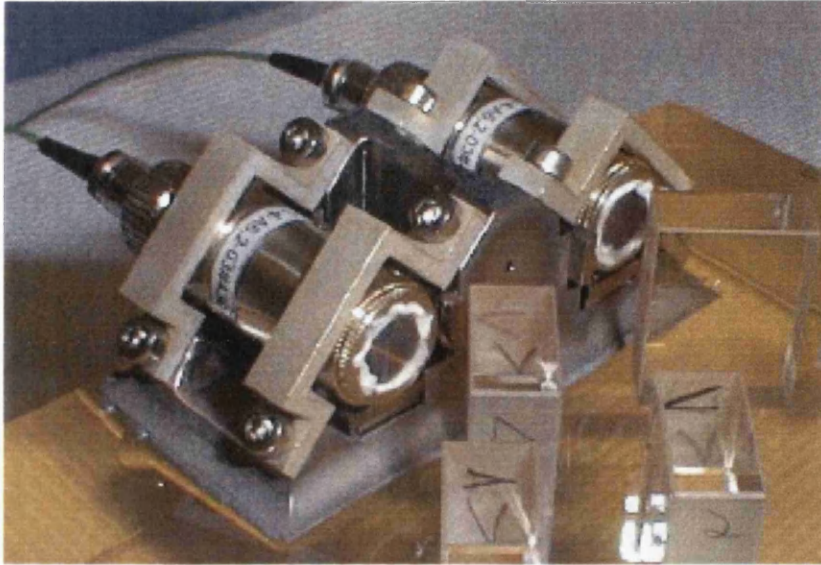


Figure 5.2: *The engineering model fibre injectors (photograph courtesy of CCLRC Rutherford Appleton Laboratory).*

## 5.4 Alignment strategy

To optimise the quality of the interference at the output of each interferometer two degrees of freedom have to be adjusted, as seen in Section 3.1.9. In the construction of the prototype optical bench, these two degrees of freedom were controlled using angle adjusters on two consecutive components simultaneously. This was a very difficult process and as a result was changed for the EM construction.

During the EM all the adjustable alignment was carried out by manipulating a single component in both translation normal to the reflective surface and angular adjustment, thus giving the two degrees of freedom required. This is achieved by using two micrometers with extended metal rods attached. The rods end in tooling balls which contact the back surface of the component to be adjusted. The component can then be pushed and steered into the correct

position by adjusting the micrometers. Figure 5.3 shows a schematic of this principle.

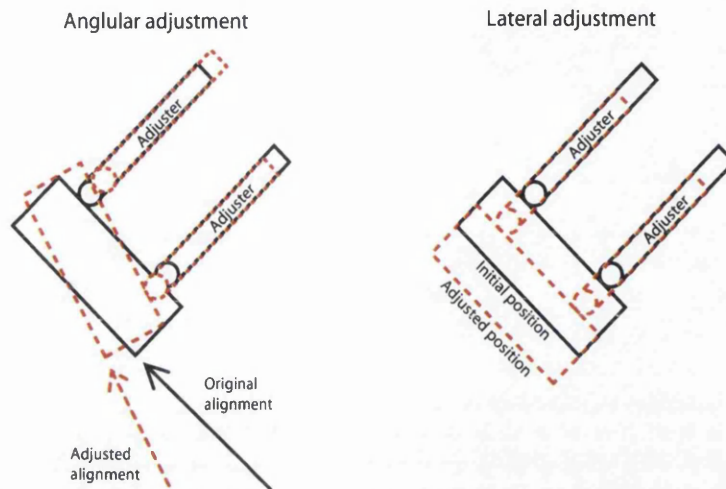


Figure 5.3: *The principle of adjustable component manipulation for the engineering model optical bench construction. The black (solid) lines indicate initial adjuster and component position and the red (dashed) lines after adjustment*

The correct component position is determined using an optical readout of the interference contrast between the two beams: one that is practically stationary while the component is moved and a second that is aligned to the first, as described in Section 3.1.9.

This method was found to be more convenient than the two component adjustment method and contrasts in excess of 80% were obtained for all the interferometers.

## 5.5 Photodiodes

Quadrant photodiodes were used for the EM. Quadrant photodiodes are needed (even though they show worse performance than single element photodiodes) for the differential wavefront sensing [63]. They were glued to the Zerodur® baseplate to ensure stability.

## 5.6 Repairing broken components

During the build phase three components were inadvertently snapped off. They had been bonded for more than a week, allowing the bonds to reach near full strength. The components failed in the bulk material (either the fused silica or the Zerodur®) giving an indication of how strong the bonding technique is. This left an uneven surface in the place where components needed to be, with no possibility of bonding a replacement component.

The solution adopted was to bond adaptor plates over the broken areas. These took the form of two parallel feet ( $\sim 20 \times 4$  mm area) supporting a raised flat platform to which the spare components were bonded. These can be seen in the photograph of the completed optical bench (Figure 5.4).

While this situation was less than ideal it provides a valuable emergency recovery for this kind of incident. The repairs survived all the environmental tests and did not degrade the noise performance.

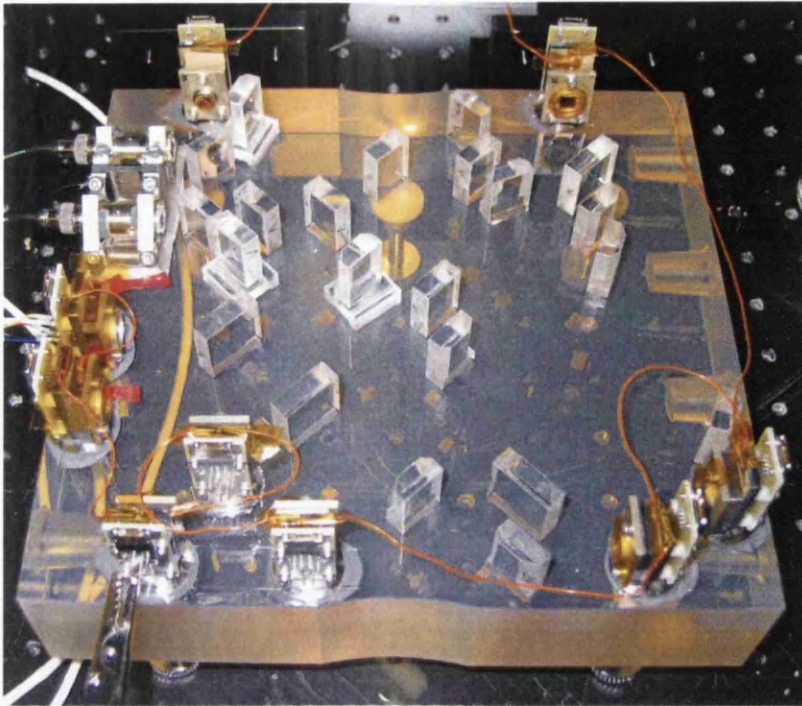


Figure 5.4: *The completed engineering model optical bench (photograph courtesy of CCLRC Rutherford Appleton Laboratory).*

## 5.7 Test results

The EM OB was tested at at the Netherlands Institute for Applied Geoscience (TNO) by staff from TNO, the Albert Einstein Institute, Hannover and Astrium GmbH.

The EM optical bench was integrated into a larger subassembly for qualification testing. The results are discussed fully in [63]. The environmental testing (involving thermal cycling between 0°C to 40°C and vibrational tests up to 25g at the struts) showed that no components had moved a significant amount (if at all). The functional tests were all as expected. The performance tests showed a large thermally driven variation due to the test mass dummy mirrors

being mounted in metal mounts. When the linear drift was compensated for (in post processing of the data) the performance met the LTP mission goal nearly everywhere.

# Chapter 6

## LISA Technology Package optical bench developments

The LTP proto-flight model (PFM) optical bench interferometer is currently in the final stages of design, and construction is due to start in Glasgow shortly. The PFM closely resembles the EM and has the same functions. The main differences are tighter alignment tolerances, new design of fibre injectors, light-weighting of the baseplate, increased fracture control planning, redesigned photodiode mounts and a more rigorous testing regime.

This chapter discusses some of the changes from EM to PFM and outlines the changes to hardware and construction methods.

### 6.1 Fibre injectors

There was not sufficient time available during the EM project to sufficiently develop the fibre injectors or the alignment method into a viable flight solution.

This left the PFM program with the options of either developing the EM design into suitable PFM hardware or to develop a new fibre injector and alignment strategy.

The EM injectors could have been manufactured using non-magnetic materials but the components would still have to be successfully thermal vacuum and vibration cycled (in sufficient numbers to provide reliable statistics) to prove flight worthiness. With the items being manufactured by a third party there was limited scope to redesign any undesirable features of the injectors. Also, the alignment technique (using shims machined to the correct height and tilt by iterations) had not been proven to reach the required alignment accuracy needed for the PFM. In the light of these required developments it was decided to design, test and construct a new fibre injector system specifically for the PFM.

This is perhaps the most significant change from EM construction to PFM construction as it, unusually, involves the creation of novel equipment at an advanced stage in the mission programme.

### 6.1.1 New fibre injector design

The new design for the fibre injectors is to use a quasi-monolithic fused silica assembly. This removes concerns over magnetic materials and means that components can be joined using hydroxide-catalysis bonding, as is used to attach the mirror/beamsplitter components to the baseplate. Figure 6.1 shows a sketch of the design of the fibre injector.

The welded pellet is a fused silica cylinder that is laser welded to the single mode polarisation maintaining fibre core. The fibre used is Fujikura Europe

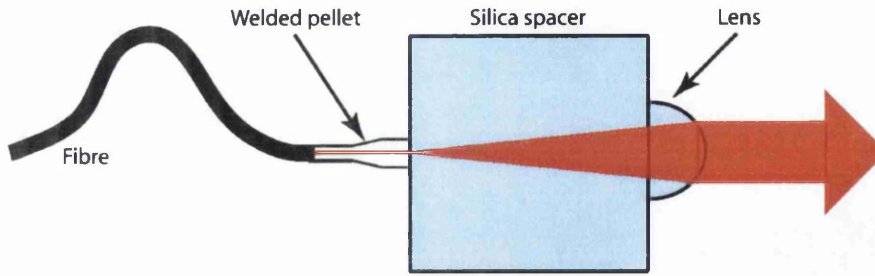


Figure 6.1: Sketch showing the new fibre injector design. The laser beam is indicated in red.

Ltd model SM-98-P-6/125 UV/UV-400. The welding technology was developed by LightPath® Technologies Inc. [64] for optical communication purposes and is chosen for use in this case as there is effectively no join and no free space between fibre end and fibre injector. The fibres have had the pellets welded in place and Figure 6.2 shows a photograph of one of the fibres with welded pellet clamped in an aluminium V-groove. Figure 6.3 shows a reconstructed Gaussian beam profile from the data used to measure the beam parameters.

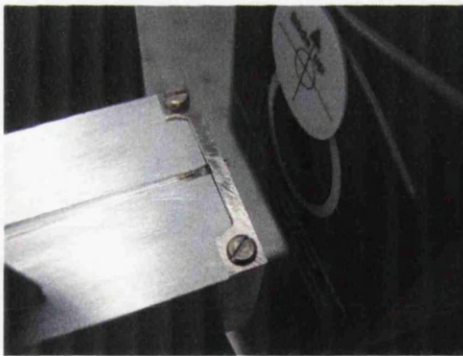


Figure 6.2: Photograph of a fibre with welded pellet (clamped in a metal V-groove).

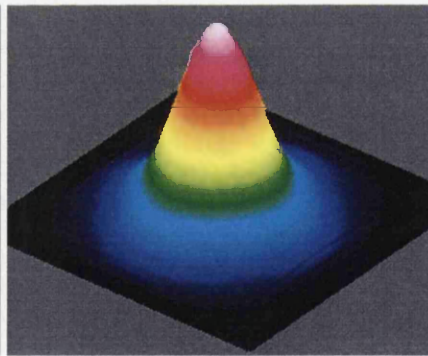


Figure 6.3: Screen capture of reconstructed 3-D profile of beam a short distance from pellet end.

The fused silica spacer is needed as the supplier does not manufacture the welded pellets with an output beam diameter large enough to fulfil the inter-

ferometry needs. The fused silica spacer enables the beam to expand further and also provides a convenient block of material to attach the fibre injector to a super-structure. Finally, the last element in the optical chain is a lens used to collimate the beam.

While it is advantageous to have the fibre injectors made in a monolithic manner to increase mechanical stability and avoid misalignment after assembly, this also requires that the manufacture of the components and the construction of the injector must be carried out to high precision, as the fibre injector output beam is tightly specified.

A driver behind the specification of beam parameters at the fibre injector outputs is the contrast of the output signals. The interferometers have a difference in path length of the two arms from fibre injector to photodiode of  $\sim 350$  mm (except the frequency noise interferometer which is roughly matched). The parameters controlled by fibre injector geometries are the wavefront curvature matching and the beam radii. The current design has the beam waist at the fibre injector outputs with radii of 0.7 mm.

### 6.1.2 Fibre injector construction

The pellet ends are not certified flat on delivery (as is needed for bonding) and the beam axis relative to the output face is toleranced to only  $3^\circ$ . Consequently the pellets will be soft waxed into a square glass V-groove and the whole front face (including pellet front face) polished to  $\lambda/10$ . The beam direction with respect to the V-block (and pellet) front face will then be measured and the V-block re-polished so that the beam exits the pellet normally.

The beam from the pellet will then be characterised. Figure 6.4 shows the

beam profile measurements of one fibre injector (prior to polishing). This was used to determine the beam waist radius and position with respect to the pellet face (as described in Section 4.1.1 using equation 4.2). This generated values for the beam waist of  $3.81\ \mu\text{m}$  a distance of  $3.3\ \text{mm}$  behind the pellet face. This is in agreement with the expected values: the fibre mode field diameter is nominally  $6.6 \pm 1\ \mu\text{m}$  and the pellet length is specified as  $3.3\ \text{mm}$ .

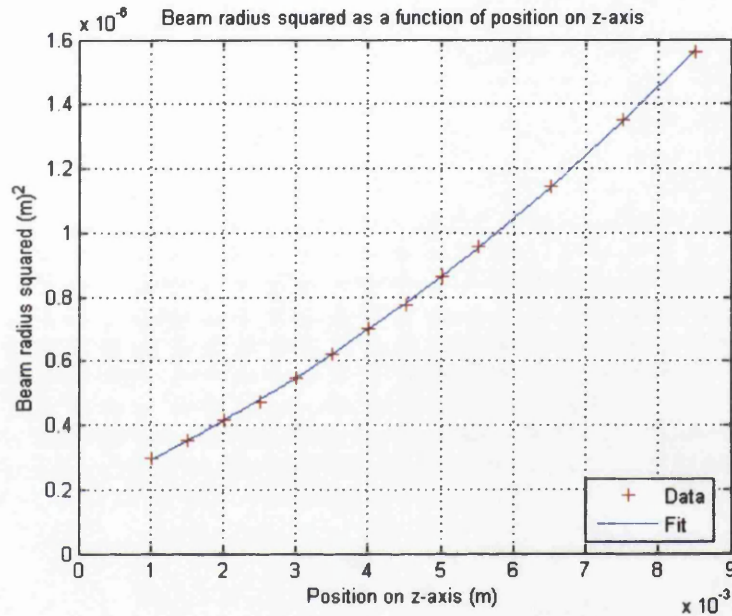


Figure 6.4: Plot of the beam radius squared as a function of distance from the pellet end. Red crosses show measured data points and the blue line shows the fitted hyperbola from which the beam parameters were extracted.

The beam profile parameters were also determined using Gnuplot [65] to fit to the data. The result is shown in Figure 6.5 (with the inverse plot also shown) with the extrapolated fit representing the expansion of the beam. This method yielded a beam waist of  $3.59\ \mu\text{m}$  a distance of  $4.8\ \text{mm}$  behind the pellet face, in reasonable agreement with the Matlab® prediction.

This information leads to the specification of the collimating lens focal length.

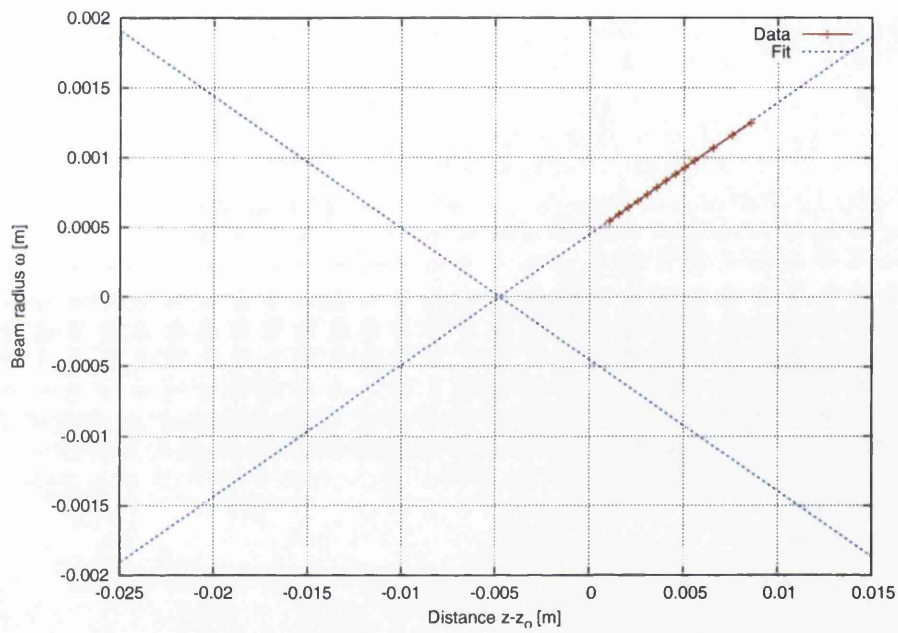


Figure 6.5: Plot of the beam radius as a function of distance from the pellet end. Red crosses show measured data points and the blue dashed line shows the fitted hyperbola.

The next stage will be to have spherical lenses of the appropriate focal length manufactured. The pellet and lens will then be positioned so as to provide the nominal beam at the lens output, but with a free space gap between them. This air gap will be measured<sup>1</sup> to determine the length of fused silica spacer required (taking into account the refractive index difference), which will then be manufactured.

Once the pellet, spacer and lens are manufactured they will be bonded together, using the optical beam to verify correct alignment of pellet to lens whilst positioning.

The light coupled onto the optical bench must be of fixed, linear polarisation. To meet this requirement a polarising beamsplitter cube (PBS) will be fixed onto a rectangular fused silica block using epoxy and the fibre injector bonded so that the light from its output travels through the PBS. This group of components is known as the fibre injector optical subassembly (FIOS).

### 6.1.3 Fibre injector optical subassembly alignment

The coordinate system used in the LTP Optical Metrology Subassembly Requirement Specification document [2] is adopted here, and is shown in Figure 6.6.

One of the changes from the EM to the PFM is the tighter tolerance for beam position at the test masses (see Section 6.2). There are two critical degrees of freedom that are dictated by the FIOS alignment (assuming the mirror and beamsplitter faces are perpendicular to the flat baseplate): the z-axis

---

<sup>1</sup>A coordinate measuring machine (as described in Section 6.11) will be used to measure this distance to an accuracy of  $\sim 1 \mu\text{m}$ .

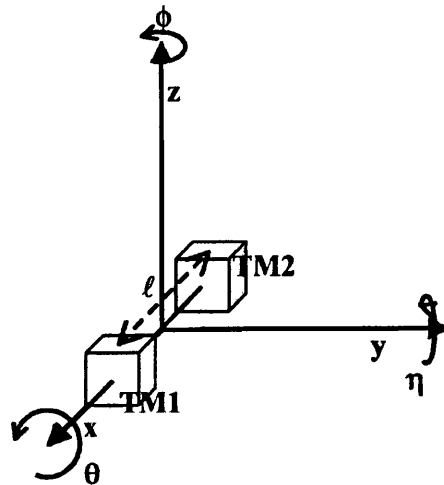


Figure 6.6: *Diagram showing the coordinate system for the optical bench interferometer. Taken from the LTP Optical Metrology Subassembly Requirement Specification [2].*

alignment (*i.e.* the vertical height above the optical bench) and the rotational  $\theta$ -axis (*i.e.* the rotation about the x-axis or equivalently tilt out of the plane of the optical bench). Alignments in other axes alignment are not as critical for the FIOS positioning as the succeeding components can be used for the fine adjustment of the ‘horizontal’ alignments.

The beam position at the test masses must be within a  $\pm 50 \mu\text{m}$  error box and an angle of  $100 \mu\text{radians}$  to the nominal. The concept of alignment that will be used to align these is illustrated in Figure 6.7, where the FIOS is indicated by a rectangular cuboid for simplicity.

A silica block (shown as a post with a flat here) will be bonded to the baseplate with an alignment tolerance of  $\sim 100 \mu\text{m}$  and this will dictate the FIOS alignment along the x-axis and provide a guide for the y-axis alignment. The reference flat on the FIOS fused silica spacer will provide a bonding area to attach the FIOS to the post (and hence the baseplate) and also provides the

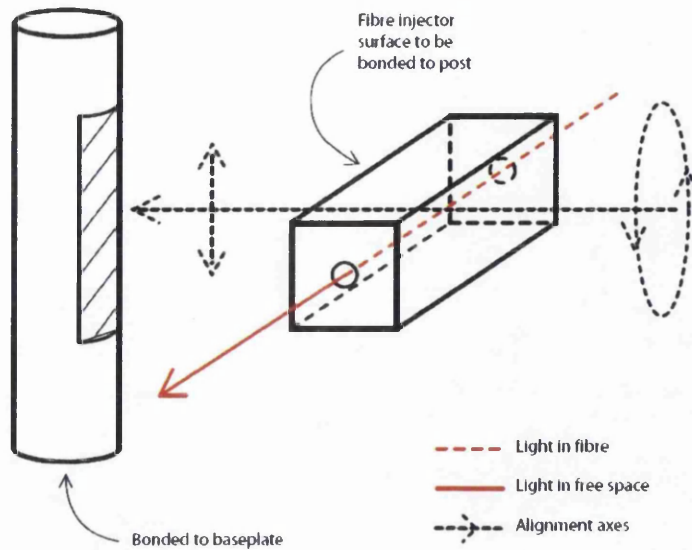


Figure 6.7: Diagram showing the concept of fibre injector alignment with respect to the baseplate.

$\phi$  and  $\eta$  rotational alignment. A CAD drawing of the current fibre injector design, showing both fibre injectors, is shown in Figure 6.8.

## 6.2 Alignment tolerances

The PFM requires tighter alignment tolerances than for the EM for path length matching and beam position at the test masses (and as a consequence fibre injector alignment). The details of alignment tolerances can be found in the Technical Note [66].

The alignment of the fibre injectors has been discussed in Section 6.1.3. The positioning of the beam combining beamsplitters for the PFM will be done using a strategy similar to that used for the EM, as described in Section 5.4. More components will also be positioned in this way for the PFM to match the

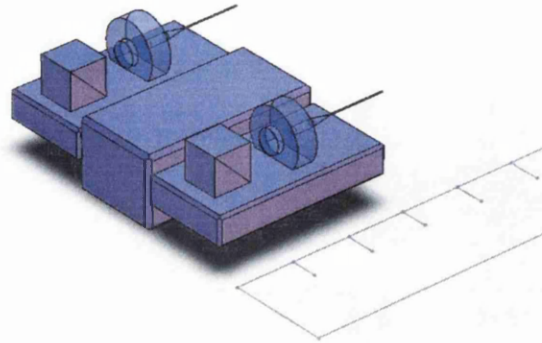


Figure 6.8: CAD drawing showing the fibre injector optical subassemblies in place. The ruler has 10 mm graduations for reference.

path lengths in the interferometers, namely M1 (path length compensator for the  $x_1$  measurement path) and M5 (path length compensator for the  $x_1 - x_2$  measurement path).

The  $z$ -axis and  $\theta$  (which translates to  $\eta$  after reflection at BS1) rotational alignment of the beam at the test masses is set by the FIOS alignment (and the error build up from off-perpendicular components and/or uneven baseplate). The other degrees of freedom (which can be considered as ‘horizontal’ to the  $z$ -axis ‘vertical’) must be controlled by reflective component placement: BS1 for test mass 1 and M4 for test mass 2. Figure 6.9 shows a diagram of the positioning strategy for aligning the beam reflected from M4 to test mass 2 (which has a longer lever arm than BS1 to test mass 2 and thus requires more sensitive alignment).

For the beam to hit the  $\pm 50 \mu\text{m}$  target in the  $y$ -direction the angle  $2a$  is  $250 \mu\text{rad}$ , giving  $a = 125 \mu\text{rad}$  (this is the required angular movement of component M4). This angle corresponds to a movement of one actuator of  $1.25 \mu\text{m}$ , which is a factor of around 100 greater than the minimum resolution of the

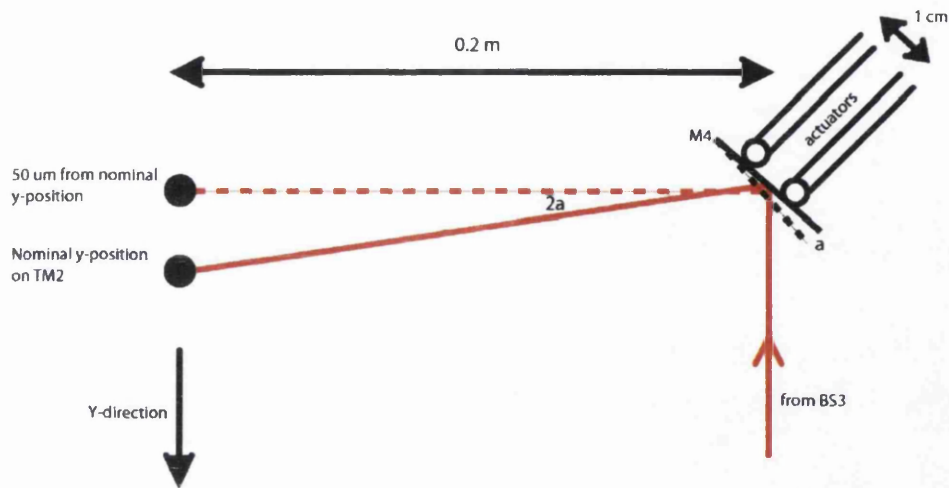


Figure 6.9: Schematic showing alignment of the beam to test mass 2 using mirror  $M_4$ . The distance of 0.2 m is exaggerated slightly as a precaution so as not to underestimate the required sensitivity.

actuators acquired for the task. Tests will be conducted to ensure that other effects, such as repeatability of positioning components, do not prevent this requirement being met.

## 6.3 Alignment strategy

### 6.3.1 Beam measurement

In order to align the beam to the PFM requirements the centre of the beam must be defined to at least as high a precision, including measurement error.

It is possible to centre a beam's optical centre on a quadrant photodiode (QPD) to within a few microns. If the centre of the photodiode can be determined in relation to some physical reference then that reference can be positioned with

respect to the optical bench and thus the QPD used as a target to monitor beam position.

This is the key technique in the alignment plan for the PFM. In order to realise it a calibrated QPD (*i.e.* one whose centre position is known with respect to its casing) and the ability to measure physical distances to a few microns over tens of centimetres is required.

One possible flaw in this strategy arises if the beam being measured has an irregular shape such that the optical centre (the median point of intensity) is different to the geometrical centre (the median point as defined by distance from the beam 'edge'). This should not be a problem here as the beams will be good quality Gaussian beams with  $> 95\%$  roundness, as shown in Figure 6.3. The beam centre will be defined as the optical centre, as this is what the QPD measures. The QPDs will be mounted in a cubic aluminium casing of side  $\sim 5$  cm, as shown in Figure 6.10.

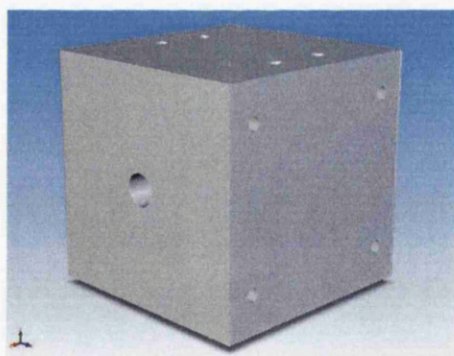


Figure 6.10: *CAD drawing of quadrant photodiode mount. The hole visible at the centre of the left side face is the photodiode location.*

### 6.3.2 Precision metrology

A coordinate measuring machine (CMM) will be used to measure the relative positions of the baseplate, optical components and the calibrated QPD. The CMM operates using a contact probe attached to an arm that can be moved in three dimensions by a gantry. The probe can also rotate to many angles covering a hemisphere. The stylus at the probe tip touches the surface being measured and can either take series of points or an analogue scan. A photograph of the CMM is shown on the left hand side of Figure 6.11 with a close up on the right hand side, showing one of the  $\sim 21 \times 20 \times 4.5$  cm baseplate blanks (before machining and polishing) being measured and the QPD mount on an xyz translation stage.

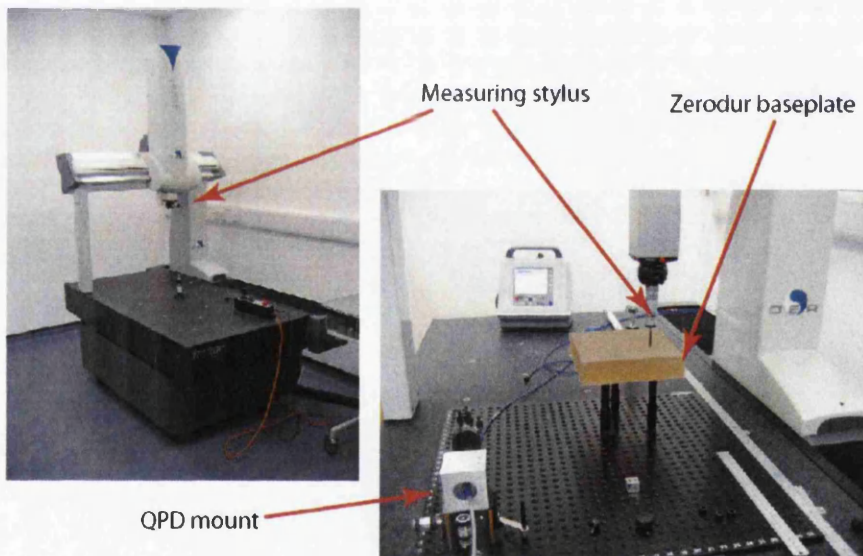


Figure 6.11: *Photograph of the coordinate measuring machine used for precision metrology (left) and one of the Zerodur® baseplate blanks being measured (right).*

The CMM will be used to calibrate the QPD. The photodiode mount will be characterised: the top, front and two side faces will be measured to give a

model of the individual machined mount. A beam will be centered on the photodiode (by translating the beam and monitoring the *d.c.* level of the four quadrant signals), with the beam normal to the front face of the photodiode.

The QPD will then be rotated through  $180^\circ$  around the beam axis and centered to the beam (the beam will remain unmoved) and remeasured. An example illustration is shown in Figure 6.12. The photodiode offsets  $X$  and  $Y$  are initially unknown, but they are likely to be of order 1 mm due to machining tolerances. Knowledge of the photodiode position is required at the micron level, so tighter tolerances would not be advantageous as calibration would still be required.

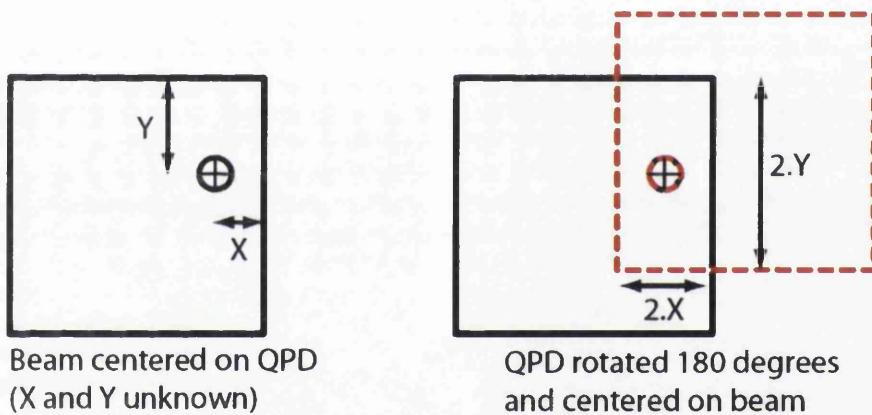


Figure 6.12: *Diagram showing quadrant photodiode calibration, viewing along beam axis. In the right hand diagram the mount has been rotated  $180^\circ$  and is indicated using red dashed lines.*

Using the measured mount positions the values  $2.X$  and  $2.Y$  can be found and the QPD position relative to the mount is known. The QPD can then be centered on a beam and by measuring the mount position the beam position can be inferred. By moving the QPD to another position along the beam axis and measuring the beam position again, the beam direction can also be obtained. The distance between measurements should be as large as practically

possible to increase the lever arm effect and achieve higher accuracy.

The calibrated quadrant photodiode can then be used to monitor all beams in sequence as the optical bench is constructed. In this mode of operation the knowledge of the photodiode centre position will be used to position the QPD where the beam should nominally pass, using the CMM to measure the relative positions of the baseplate and the QPD. This method will be used to align the fibre injector subassembly to the baseplate and then the mirrors and beamsplitters.

It will also be used as a target in place of the test mass to ensure that the beam hits the required error cube on the test mass when the optical bench is assembled.

Using these tools the PFM alignment tolerances can be met and also provide an as-built optical model of the interferometer. Monitoring of the beam alignments (transferring coordinates between mechanical and optical models) will allow any minor adjustments to component position to be made during the construction, removing the error build up that can occur when relying on template positioning of components.

## 6.4 Alternative adjustable bonding technique

Bonding components that require fine adjustment is difficult due to the short settling time available between placing the component and the bond starting to set. As both surfaces are very flat and clean it is not possible to place one against the other without fluid between them as optical contacting occurs. For this reason a technique was developed during the prototype optical bench construction (Section 3.2.3) to enable fine adjustment of critical component

positions. This technique was subsequently used in the engineering model construction.

The technique involves using a buffer fluid to float the component while it is manipulated into position (monitored using an optical readout). The fluid gradually evaporates and so the component must be removed periodically ( $\sim$  every three minutes), more fluid applied and the component replaced. When the alignment position has been determined by the adjuster positions and repeatability of replacement has been shown the component is removed and the buffer fluid allowed to evaporate.

The component is then replaced using bonding fluid. While this technique has been proven to offer the alignment resolution and ultimate bond strength required for the PFM, it is a difficult procedure and has some risks associated with it: repeated removal and replacing of the component can lead to scratches on the surfaces that result in an inferior bond. Also, the buffer fluid has higher viscosity than bonding fluid it forms a thicker layer and introduces a vertical tilt to the component. This results in the QPD top and bottom quadrants not being in phase during alignment until the bonding fluid is used instead of buffer fluid, which leaves approximately 30 seconds for the final fine adjustment (if required).

These risks can be reduced, though. The current plan for the PFM construction involves suspending the next mirror/beamsplitter in the sequence above the baseplate prior to bonding, using an adjustable gantry system. In this way the reflective plane of the component will be manoeuvred into the nominal position and orientation. The adjusters will then be brought up to the component surface, thus removing all the course alignment using buffer fluid and the number of placing/removal cycles required. However, it would still be preferable to have no time constraints involved in the bonding process.

A bonding technique is being developed at Glasgow University (not solely for use on the PFM construction) where one of the bonding surfaces is lightly ground. This involves initially polishing the surfaces to the required  $\lambda/10$  and then grinding one of the surfaces with a fine paste to increase the local surface roughness. A photograph of a  $20 \times 20 \times 5$  mm fused silica component with a ground bonding surface is shown in Figure 6.13. This has the benefit of preventing optical contacting when the two surfaces are placed in contact. Bonding fluid can then be introduced to the join by a wicking process: this would be ideal for alignment of optical components as the nominal component position can be found and the component does not have to be moved for bonding.



Figure 6.13: *Photograph of a ground surface on a representative fused silica component.*

Preliminary tests were conducted to investigate the effect of manually grinding the surface of representative LTP mirror components on the perpendicularity of their reflective face to their bonding face (based on similar techniques to those described in Section 3.2.1). The grind (which was as light as possible to prevent optical contacting) was found to change the surface figure significantly, resulting in the angle between the two relevant surfaces changing by 33 arcseconds after grinding. This rules the ground surface bonding method out for aligning of the mirrors and beam splitters, although it is likely that with additional effort a method of grinding the surface could be found that

does not alter the component perpendicularity.

There is an application for the ground surface bonding during the PFM construction that does not depend on maintaining the perpendicularity of the component: attaching the FIOS to the fused silica post (which is bonded to the baseplate). Careful alignment of the FIOS is required and the tolerance for alignment of the rotation that would be altered by grinding the bonding surface is large (of order  $1^\circ$ ). For the technique to be used in this instance the strength of the ground bonds would need to be verified: polished-polished surface bonding is a well established and verified method but ground-polished surface bonding is a new development.

To this end a series of tests were conducted on representative test components. The force required to break the bond was measured after varying amounts of time since bonding. The test plan is detailed in [67] and the full report on the tests in [68]. The test pieces were  $20 \times 15 \times 7$  mm fused silica blanks (chosen to be representative of the PFM mirrors and beamsplitters) whose bonding surface was lightly ground by hand then bonded to 25 mm fused silica flats. These had a 'peeling' force applied by holding the flat and applying a force at the top of the component. Figure 6.14 shows nine of the 12 bonded pieces tested and Figure 6.15 shows one of the pieces in the strength testing apparatus.

The required force these components must withstand to qualify this technique for flight is 80g. Normally a bond would be left for in excess of a week to reach full strength but in this case they were tested (in groups of three) at varying time intervals. This was to try and gain an insight into the curing behaviour of ground bonding as this was a completely new process. The results of these investigations are shown in Figure 6.16.



Figure 6.14: *Photograph of nine of the 12 ground bonding strength test pieces.*

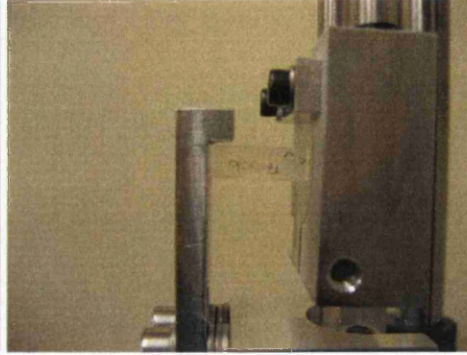


Figure 6.15: *Photograph of a test piece (TM006) in the strength testing machine.*

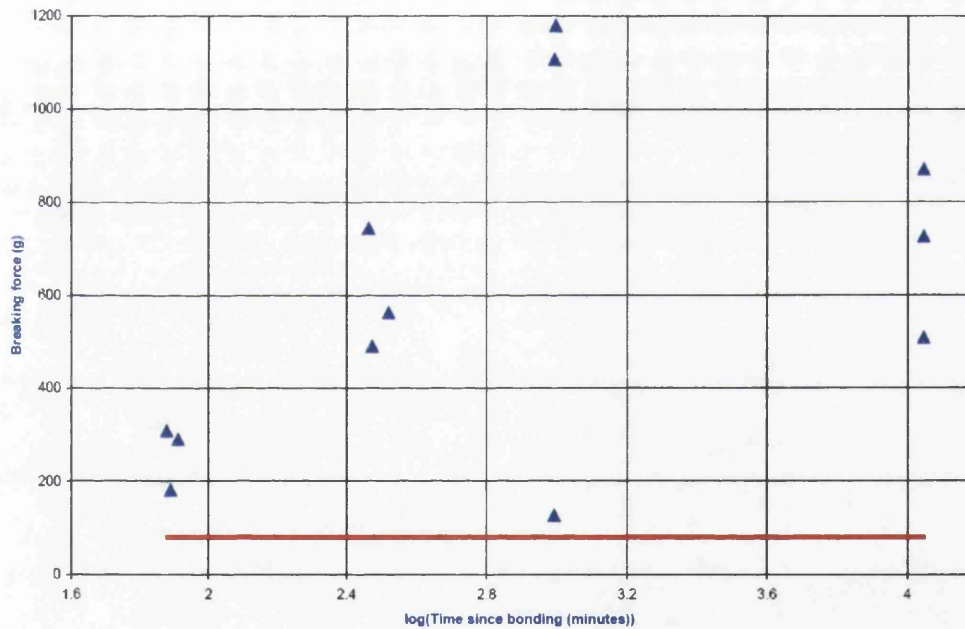


Figure 6.16: *Plot showing the force required to break the ground bonds (in terms of equivalent number of g) against the time since bonding. The blue triangles are data points and the red line is the 80g static load qualification threshold. The four batches of three components shown were tested after approximately one hour, five hours, 16 hours and seven days.*

The components have a mass of  $\sim 5$  g and so a force of 1g is equivalent to 0.0491 N. In this test the force was applied to the point of the component furthest from the bond. The requirement for flight qualification defines a static force acting at the centre of mass of the component, therefore a factor of two has been included in the plot (the actual breaking force is twice the breaking force required acting at the centre of mass).

In general the technique appears to produce bonds considerably stronger than required - all bonds tested comfortably exceeded the 80g threshold before breaking and many were nearly an order of magnitude above this. There is, however, one rogue point from the third batch of tests that broke under an equivalent load of 127g. This point causes concern as it is so far from the position of the other tested bonds with the same time since bonding. There are a number of features of these tests that *could* account for this but there is no known reason and the bond did not visually appear any different to the others.

Further tests of this method will follow to improve the statistics of the analysis, although the immediate tests will concentrate on components that have been bonded for in excess of a week as this is all that will be relevant to the PFM construction.

# Chapter 7

## Weak light phase locking for LISA

### 7.1 Introduction

The space based gravitational wave detector LISA requires high precision interferometric measurements to be made with very low detected light powers. This is a consequence of having limited laser power, limited emitter and receiver diameter and a large separation between emitter and receiver. This results in a beam emitted from one spacecraft with a waist of 40 cm diameter expanding to a diameter of around 17 km after having traveled the  $5 \times 10^9$  m between spacecraft. The equation giving the beam radius is:

$$\omega(z) = \sqrt{\omega_0^2 + \frac{z^2 \lambda^2}{\pi^2 \omega_0^2}}, \quad (7.1)$$

where  $\omega(z)$  is the beam radius at a distance  $z$  from a waist of  $\omega_0$  and  $\lambda$  is the wavelength of the light [53].

It is clear that only a very small fraction of the emitted light will fall within reach of the receiving telescope. The received light power ( $P_r$ ) is related to the emitted light power ( $P_t$ ) by

$$P_r = \frac{d^4}{2\lambda^2 L^2} P_t \quad (7.2)$$

for the case of a Gaussian beam with its waist at the transmitting mirror of diameter  $d$ , at a distance  $L$  from the receiver. For current designs [36] this yields a received power of  $\sim 400$  pW. This is the source of the most dominant noise in the round trip distance measurement as we cannot measure the phase below the shot noise limit set by the detected photocurrent:

$$\phi \simeq \frac{1}{2\pi} \sqrt{\frac{e}{i}} \text{ cycles}/\sqrt{\text{Hz}} \quad (7.3)$$

where  $e$  is the charge of an electron and  $i$  is the photocurrent due to the weak light, assumed significantly smaller than that of the local oscillator light. Thus the limit to which the received light phase can be known is a few  $\mu\text{cycles}/\sqrt{\text{Hz}}$  and any operational mode of LISA must be able to measure the phase to near this limit. One possible mode of operation involves locking the local laser light to the incoming, weak light.

Doppler shifts between LISA spacecraft will change the frequency of the beat-note between lasers on separate spacecraft by up to 15 MHz. A successful locking scheme for LISA must have sufficient range to accommodate this shift.

This chapter describes a programme of work to demonstrate phase locking at LISA power and performance levels in a laboratory experiment.

## 7.2 Concept

To test the idea of locking the light emitted from a LISA spacecraft to the incoming weak light, the phase locking loop between two LISA spacecraft can be considered as depicted in Figure 7.1. In this model one spacecraft acts as the master and the other as the slave.

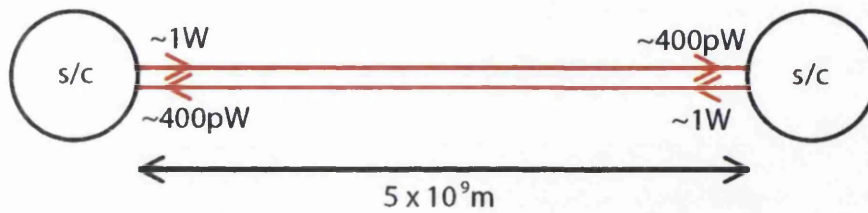


Figure 7.1: *Conceptual schematic of the phase locking loop between two LISA spacecraft showing incoming weak light and outgoing phase locked light. Laser beams are indicated by red lines.*

We can simplify a single LISA spacecraft to the relevant components as shown in Figure 7.2. At the slave spacecraft the master light (with very low intensity) is mixed with some of the slave light ( $\sim 1$  mW) to generate a beatnote at a specific offset frequency at the photodiode.

The beatnote is used to offset lock the slave laser to the master laser at the chosen offset frequency using a feedback servo to the laser crystal temperature control and piezo. Offset locking is a scheme whereby the incoming light is mixed with a small fraction of the outgoing light and this signal is then electrically mixed with a signal of a chosen frequency. This combined signal is then fed back to the laser to force the outgoing light to be separated in frequency from the incoming light by the designated frequency. In this way the new laser light directed to the master spacecraft carries all the information of the received light but with much greater power at a slightly shifted frequency. This

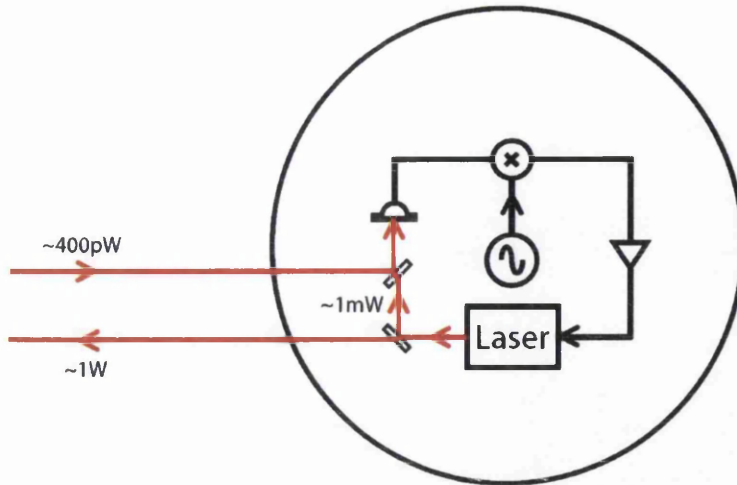


Figure 7.2: *Conceptual schematic of a single arm of one LISA spacecraft showing incoming weak light and outgoing phase locked light. Laser beams are indicated by red lines.*

model lends itself to laboratory demonstration as all the parameters present in the LISA situation can be reproduced.

### 7.3 Laboratory demonstration

The final laboratory demonstration will consist of two Nd:YAG non-planar ring oscillator lasers phase locked together as shown in Figure 7.3. The light from the master and slave lasers are combined at two points, one with comparable power levels in each arm and one with the master light heavily attenuated. This produces two beatnotes of constant phase difference (assuming no path length variations in the interferometers) but of different amplitude. The slave laser light is offset locked to the master light using the low amplitude signal to simulate the LISA case. The full power interference is used to provide an independent measurement of the stability of the lock. The shot noise of the full

power beatnote is a factor of  $\sim 1000$  lower than for the low power beatnote.

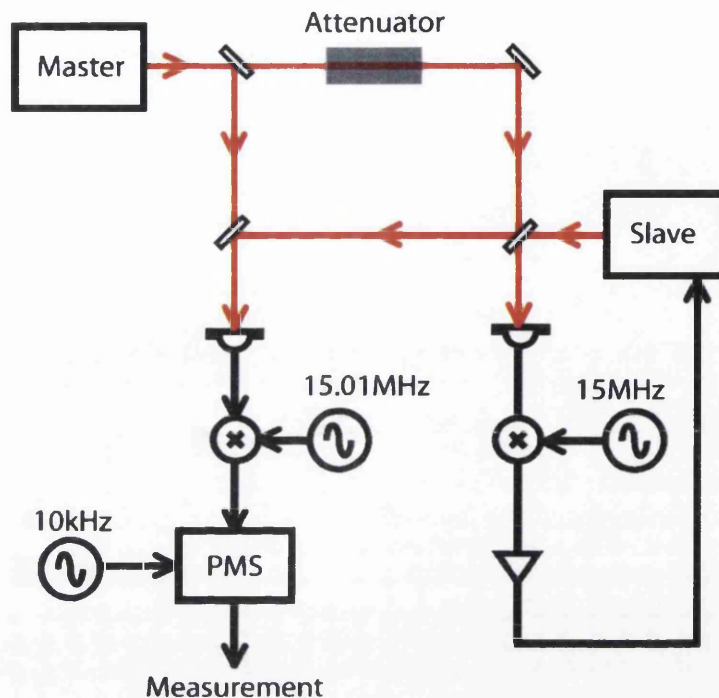


Figure 7.3: *Conceptual schematic of experimental layout to demonstrate weak light phase locking. Laser beams are indicated by red lines. The 10 kHz reference for the PMS is generated by mixing the two signal generator outputs in order to achieve the stability needed.*

### 7.3.1 Phase stability of interferometers

Path length variations between the two interferometers must be kept to a very low level. Previously this has been attempted by using polarisation schemes where both beams follow identical paths to make any path length variations common mode [51]. This can lead to difficulties in ensuring that the individual interferometers are behaving in a completely separate manner.

The creation of a suitably stable optical system using polarising optics is very

challenging and a preferable approach is to have the two interferometers as separate entities, but each with a suitable intrinsic stability. This need is addressed by using the prototype LTP optical bench whose stability was proven by tests described in Chapter 4.

While the optical chain prior to the optical bench is different to the LTP tests, the optical bench remains the same apart from one modification. The prototype optical bench was built to have equal power in the interferometer arms. For this application the light in one arm of an interferometer has to be heavily attenuated. The attenuator is described in Section 7.4.7.

### 7.3.2 The need for signal demodulation

The phasemeter can only measure the phase difference of  $\sim$  kHz signals, as it relies on the fast clock frequency being much larger than the heterodyne frequency. For this application the fast clock was set at 20 MHz. In order to measure the phase stability of the 15 MHz phase lock the signals were demodulated to 10 kHz. This introduces a new area for phase instabilities to enter into the measurement and is discussed in Section 7.4.2.

The low power beatnote signal is detected on a high frequency photodiode. It is then passed through an amplifier chain, band pass filtered and split two ways. One of the signals enters the *rf* port of a mixer and is demodulated to *d.c.* at the mixer output using a 15 MHz signal from an Agilent 33120A signal generator which drives the local oscillator port of the mixer. The mixer output is low pass filtered and used as the error point of the locking servo. The servo feeds back to both the temperature control of the slave laser crystal and to a piezo attached to the laser crystal. Applying signals to these actuators yields a change in laser frequency: the temperature control dominates the low

frequency (below 1 Hz) region and has large range while the piezo has a smaller range but can operate at higher frequencies.

The low power beatnote signal can simultaneously be demodulated to a convenient heterodyne frequency and injected into the phase measurement system (PMS) which is described in Section 7.4.1. The phase of the heterodyne signal can then be measured relative to the phase of a stable reference signal (from a signal generator phase locked to the demodulating signal generator) or to the phase of another optically generated signal. Using this signal, an output of the PMS can be used to drive the low frequency feedback path for the phase lock in order to avoid mixer flicker noise and low frequency electronic noise in the analogue servo. This additional feedback path is indicated in Figure 7.4.

The high power beatnote is demodulated using a separate signal generator (phase locked to the 15 MHz generator) to provide an out of loop input to the PMS. The phase stability of this signal compared to the phase of the electrical reference signal gives an independent measure of the phase locking quality. The aim of the experiment is to be shot noise limited by the low power light, as measured by the full power signal, over the frequency range appropriate for LISA.

In order to demonstrate phase locking at the LISA level, frequency stabilisation of the light is required. This is because the path lengths of the interferometer arms are not exactly equal, giving a coupling of frequency noise to phase noise. The frequency noise is measured and removed as described in Section 4.3.5. This interferometer has been omitted from Figure 7.3 for clarity.

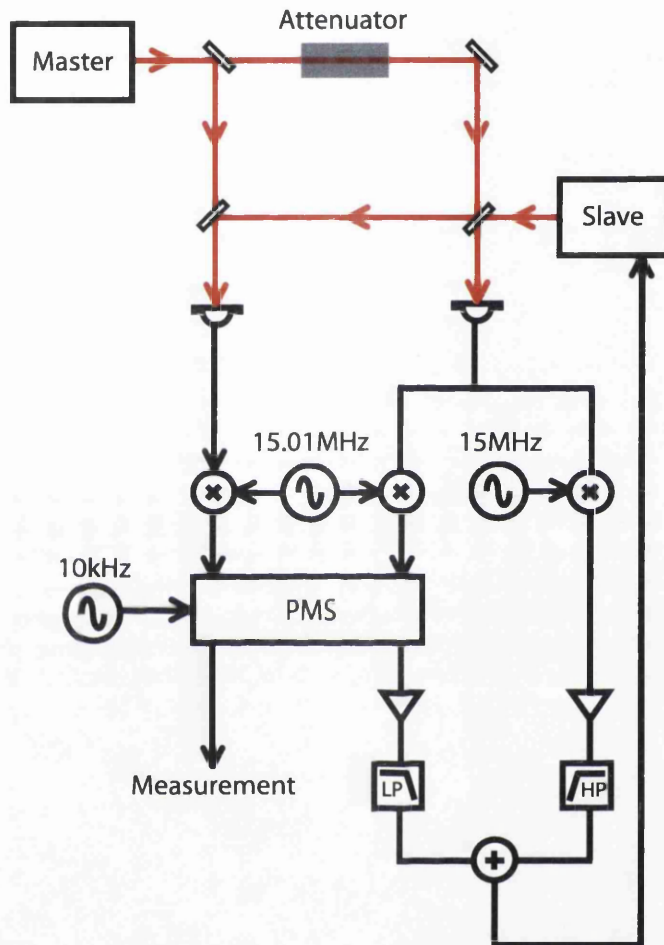


Figure 7.4: Schematic of experimental layout to demonstrate weak light phase locking showing the dual path analogue and digital feedback. Laser beams are indicated by red lines. The 15 MHz and 15.01 MHz signal generators are phase locked together.

## 7.4 Subsystems

There now follows a discussion of preliminary investigations conducted to demonstrate that the subsystems of the experiment operate without introducing excess noise into the integrated system. The amplitude of the low power beatnote ultimately planned for use in this experiment gives a shot noise limited phase noise of around  $6 \mu\text{cycles}/\sqrt{\text{Hz}}$  over the frequency range of interest, so the combined noise contribution of the measurement chain must be below this. These investigations were sequential and conducted as the experiment was constructed.

### 7.4.1 The phase measurement system and associated electronics

The first experiment to be conducted is the simplest possible: phase locked signal generators driving a phasemeter. Even this small scale experiment requires significant effort to reach the LISA stability goal. The phasemeter used in the prototype optical bench stability tests described in 4.1.2 has demonstrated performance close to the required level. Some minor modifications were made for this experiment.

The simplest set up of three phase locked Agilent 33120A signal generators supplying 10 kHz signals to the phasemeter *via* comparators was tested, as shown in Figure 7.5, with one signal used as a reference to which the other two have their phase compared. The results are shown in Figure 7.6. This demonstrates that the phasemeter is capable of measuring phase differences down to  $2 \mu\text{cycles}/\sqrt{\text{Hz}}$  which is below the expected limits imposed by shot noise.

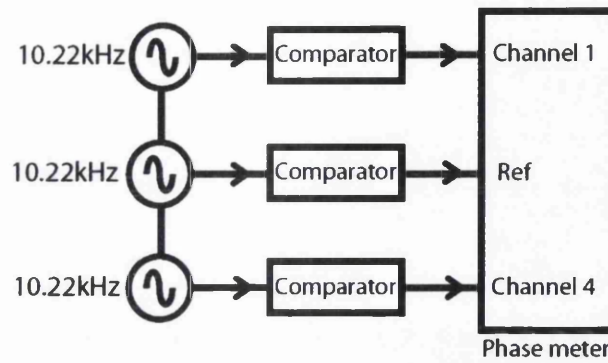


Figure 7.5: Diagram showing set up for phase stability testing of comparators and phasemeter.

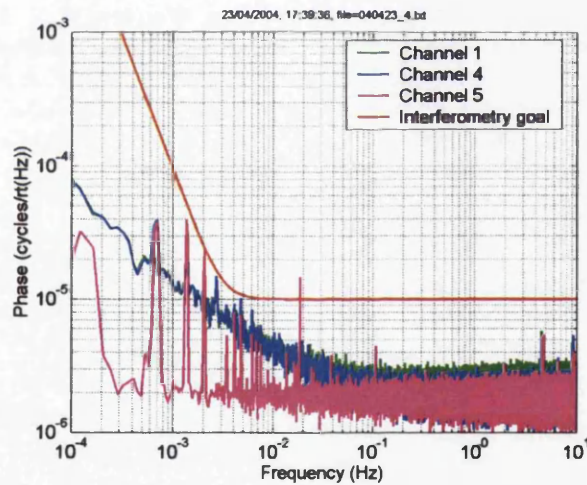


Figure 7.6: PSD showing result of test set up shown in Figure 7.5. Channels one and four are two measurement channels and channel five is the difference between one and four. The red line is the LTP interferometry goal, shown for reference. The LISA goal is  $6 \mu\text{cycles}/\sqrt{\text{Hz}}$ .

The next test was to introduce mixers to the chain. The mixers used were Minicircuits model SBL-1. The stability of these mixers is vital as separate mixers are needed to demodulate each of the optical signals from the high frequency photodiodes. The experimental set up is shown in Figure 7.7 and the results are shown in Figure 7.8. Significant noise is seen in channels one and four (the measurement channels). This noise was tracked to one of the comparators which was later changed. In this run the noisy comparator was used in the reference channel chain and so the noise is common mode in the phase difference measurements, as demonstrated by the phase comparison between channels one and four (labeled 'channel five' on the plot).

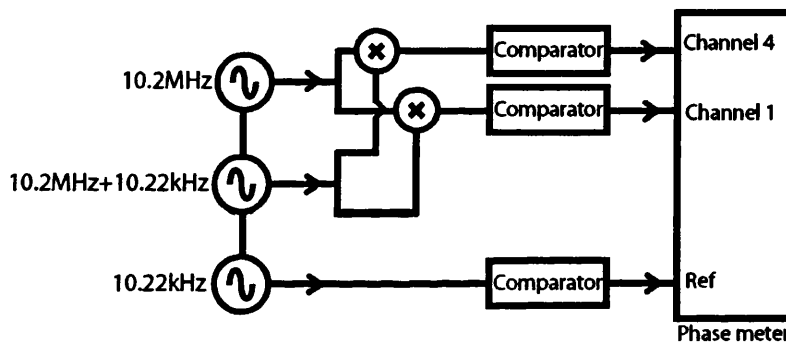


Figure 7.7: Diagram showing set up for phase stability testing of mixers.

These signals were filtered immediately prior to the comparators using four pole low pass Chebychev filters [69] with a corner frequency at 14 kHz. The amplitude response of one of the filters is shown in Figure 7.9. Filtering is required as the PMS is sensitive to noise at harmonics of the heterodyne frequency, which exist at the mixer outputs. 15 MHz passive band pass filtering is used on the high frequency signals to reduce high frequency harmonics which could be picked up and demodulated elsewhere in the system. These harmonics can generate excess noise if the signal pick up is not phase stable with respect to the signal being measured.

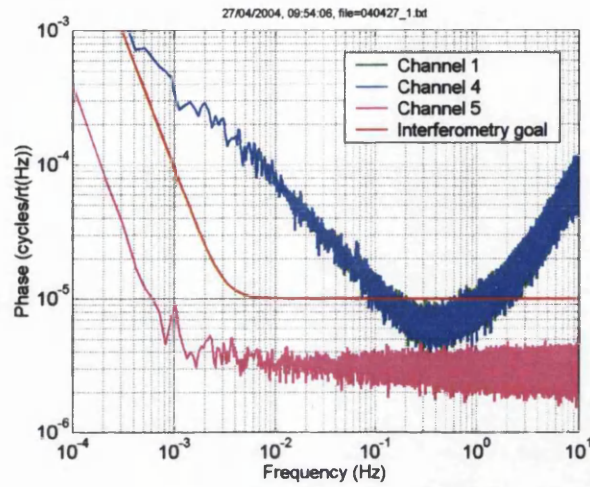


Figure 7.8: PSD showing result of test set up shown in Figure 7.7. Channels one and four are two measurement channels and channel five is the difference between one and four. The red line is the LTP interferometry goal, shown for reference. The LISA goal is  $6 \mu\text{cycles}/\sqrt{\text{Hz}}$ .

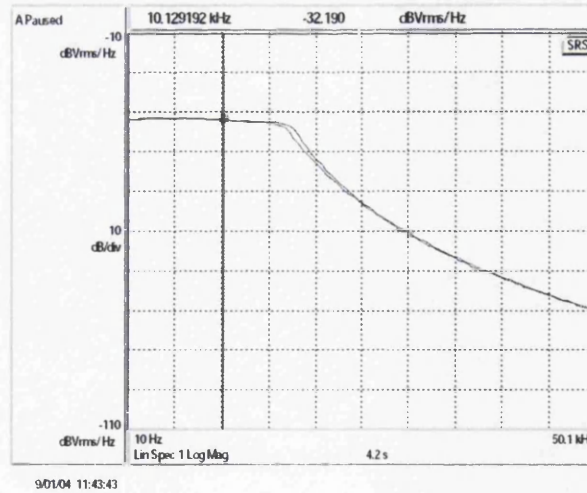


Figure 7.9: Amplitude response of the 10 kHz low pass filters used prior to the phasemeter.

### 7.4.2 Signal demodulation

We require a demodulation signal to transfer the phase information of the 15 MHz beatnotes to a convenient frequency for the phasemeter. This leads to the signal splitting and demodulation scheme depicted in Figure 7.10; a corresponding circuit layout is illustrated in photograph 7.11.

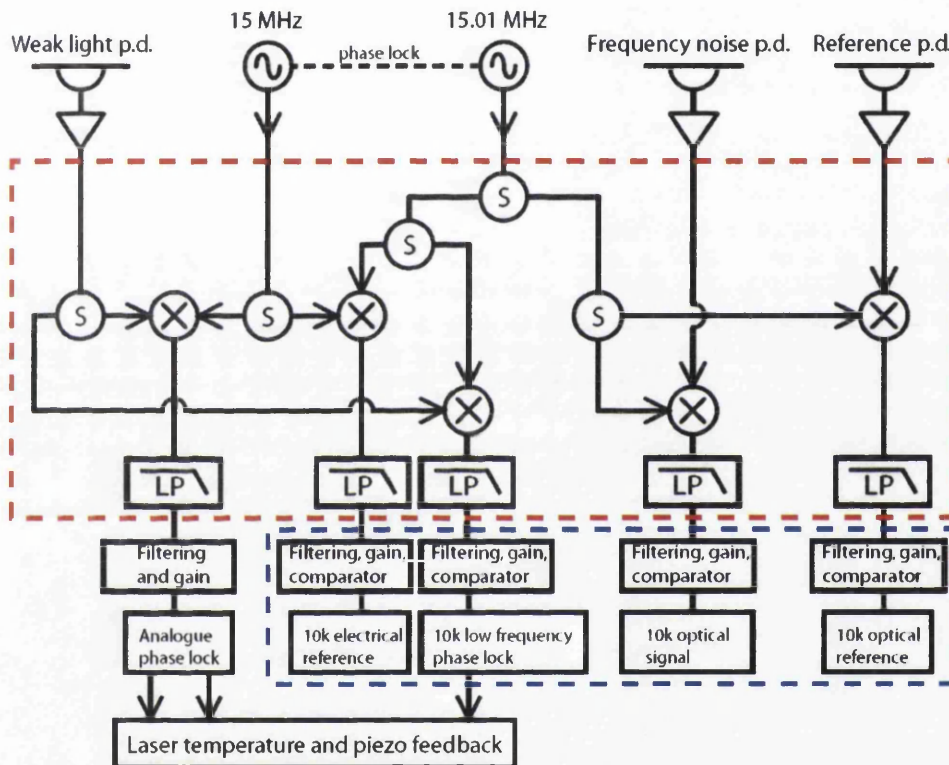


Figure 7.10: Diagram showing the signal splitting and demodulation scheme for the full experiment. 'LP' denotes a low pass filter, 'S' a 50:50 signal splitter, 'p.d.' a photodiode and 'X' mixers. The red dashed line indicates the limits of the circuit board used to demodulate the high frequency signals to 10 kHz outputs. The constituents of the PMS are within the blue dashed line.

The circuit board has the following inputs:

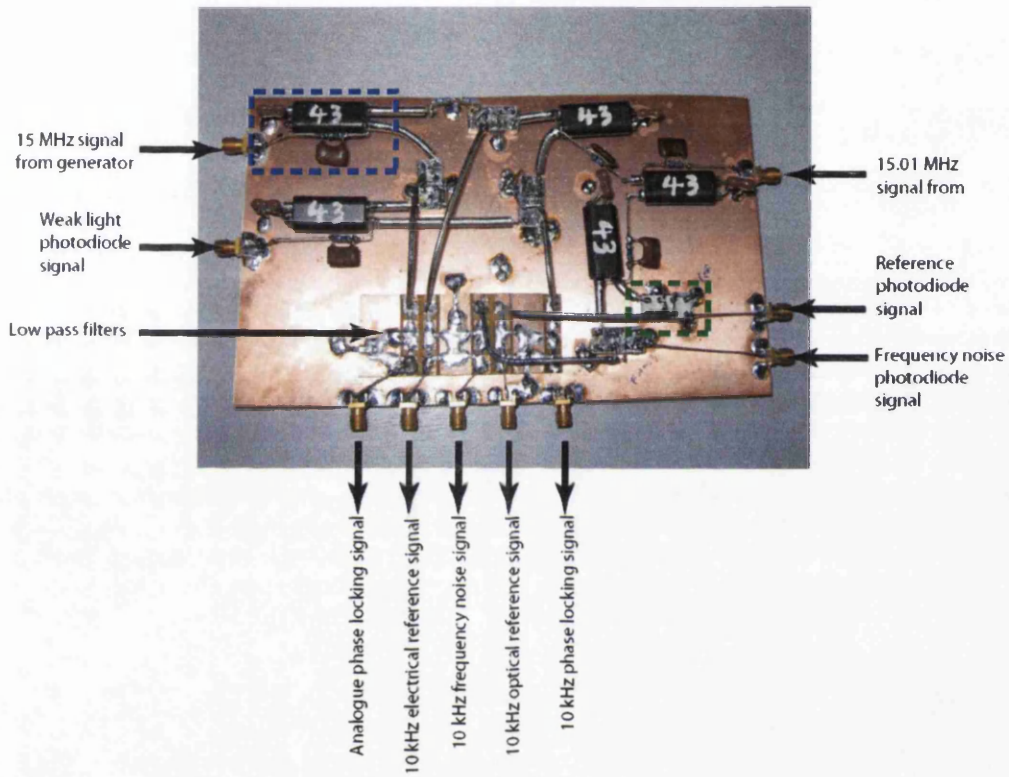


Figure 7.11: Photograph of the signal splitting and demodulation board. One of the 50:50 signal splitters is boxed with a blue dashed line and one of the mixers with a green dashed line. The 10 kHz outputs go to the filters and PMS.

- the output of the photodiode measuring the weak light beatnote, which will be used to lock the lasers,
- the output of the optical reference photodiode (measuring the same light as the weak light but with both beams unattenuated),
- the output of the frequency noise photodiode,
- the 15 MHz signal generator output (the offset lock frequency), and
- the 15.01 MHz signal generator output (used to demodulate signals to 10 kHz for the PMS).

From these signals the board outputs the following 10 kHz signals to the phase measuring system:

- an electrically generated (no optical influence) reference signal,
- an optical measurement beatnote signal (the combination of the 15.01 MHz electrical signal and the unattenuated interference signal),
- an optical frequency noise beatnote signal, and
- a signal from the weak light photodiode that is used to provide the low frequency phase locking error point.

In addition to these, the demodulation board also produces a signal from the weak light photodiode that is driven to zero by the analogue phase locking servo.

The signal sizes and *rf* power levels at each mixer input must also be managed to obtain the desired performance although this is not discussed here.

If the demodulation signals are not relatively stable for each demodulation then spurious phase noise will appear. Phase stability is also required of the 15 MHz signals being used to set the offset lock and of the low frequency signal used as an electrical reference for the PMS<sup>1</sup>.

This aspect of the experiment is not relevant to LISA as there the received signal stability is a feature of the dimensional stability of the armlengths, however it must be addressed for a laboratory demonstration of this kind.

Following extensive investigations it was concluded that only two signal generators should be used throughout as the phase lock between generators had insufficient stability to use more than one generator at each frequency. The signals from the two generators are split and the signal sizes adjusted to provide the required signals for locking and demodulation.

The demodulation board was tested using electrically generated signals (similar to the tests described in Section 7.4.1) and developed by using different components, building techniques and by adding filters until the signals produced were phase stable.

### 7.4.3 Testing of *rf* amplifiers

Once the demodulation board and PMS had been proven stable when supplied with phase stable input signals, they could be used to test other parts of the signal chains. This involves using the input ports for signals other than the designated use.

The optical signals from the high frequency photodiodes at the output of the

---

<sup>1</sup>A phase locked signal generator operating at 10 kHz proved to have poor phase stability when compared with the beatnote between a 15 MHz and a 15.01 MHz generators.

optical bench require amplification. As each signal will be amplified by an independent amplifier, the amplifiers are required not to introduce spurious uncorrelated phase changes. The Motorola amplifiers referred to in Section 4.1.1 were used, although further *rf* shielding was applied.

Figure 7.12 shows the test set up for the amplifiers. The attenuators shown are to balance the signals appropriately and had previously been tested for phase stability.

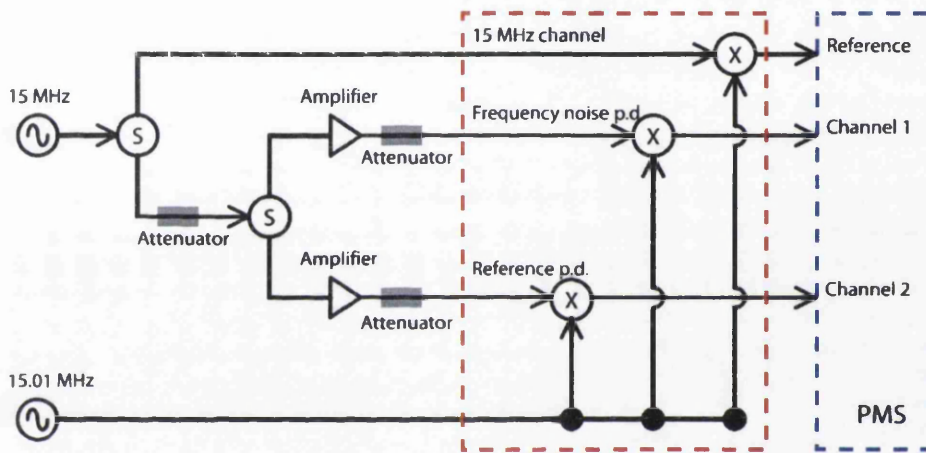


Figure 7.12: Diagram showing the set-up being used to test the amplifiers using only electrically generated signals. 'S' indicates a 50:50 signal splitter and 'X' a mixer. The red dashed line indicates the limits of the demodulation board and the blue dashed line the PMS.

For the purpose of the test two phase locked 15 MHz and 15.01 MHz signal generators were used to mimic the expected photodiode signals. These were then introduced onto the demodulation board *via* the amplifiers being tested. Upon demodulation the phase of the 10 kHz beatnotes between the electrically generated reference and the two amplifier chains should be phase stable, unless some part of the chain is causing instability. Figure 7.13 shows the resulting stability curve. The overall stability shows some excess noise which will have

to be reduced.

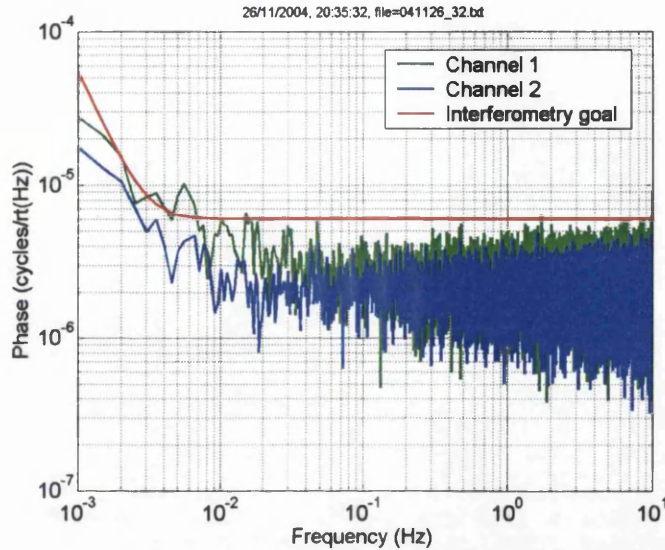


Figure 7.13: PSD showing phase stability of the amplifiers. Channels one and two are the phase stability of the amplifiers with respect to the electrical reference. The red line shows the interferometry target sensitivity, which is set by the shot noise limit of the weak light interference.

Considerable effort was made to improve the amplifier performances, and particularly to bring them both to the same phase stability. The amplifiers are nominally identical and the difference in phase stability highlights the difficulty of realising such electrical circuitry.

Other low noise amplifiers (such as Minicircuits MAR1A) were tested with voltage controlled supplies but were found to be less phase stable than the Motorola amplifiers. The amplifier testing will continue until a suitable system is in place.

With the electrical measurement chains performing at a near satisfactory level optical signals were introduced. Although signal generators tend to have mul-

multiple harmonics in their output, these can usually be filtered relatively easily using bandpass filters. 'Real' signals have higher background noise around the desired beat signal and this could introduce noise sources not seen when using electrically generated signals.

#### 7.4.4 Optical signal generation

The two laser beams are fibre coupled onto the stable optical bench using single mode, polarisation maintaining fibres similar to those described in Section 4.1.1. A photograph of the laser preparation bench is shown in Figure 7.14. The optical bench is housed in a vacuum chamber, under a vacuum of  $\sim 2 \times 10^{-2}$  mbar, in order to reduce the effects of refractive index fluctuations in the air.

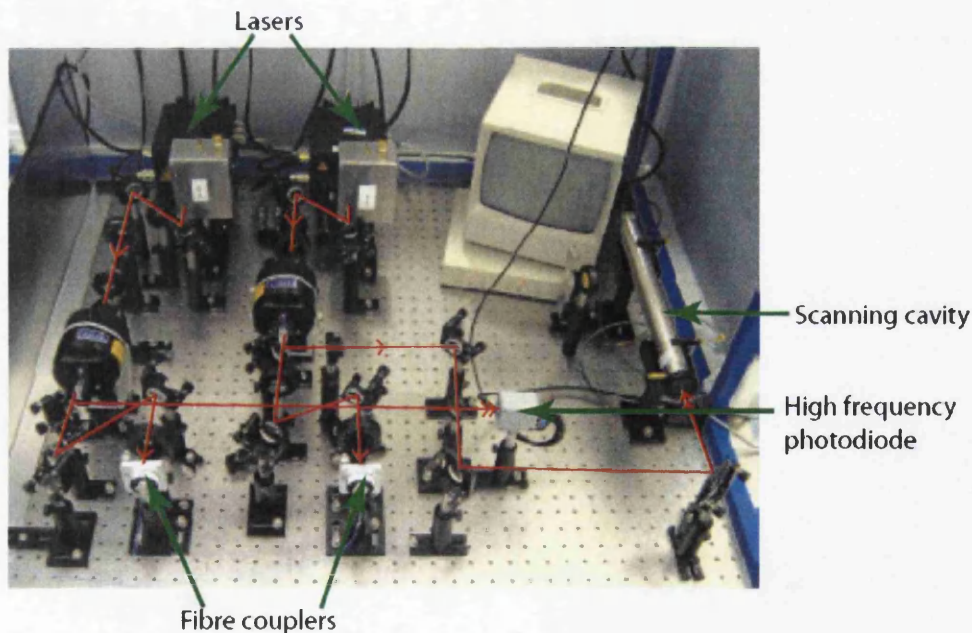


Figure 7.14: *Photograph of the laser preparation bench.*

The prototype optical bench described in Chapters 3 and 4 is used to combine

the beams. The beams from the optical bench illuminate high frequency photodiodes (manufactured by EG&G, model C30642G [70]) outside the vacuum tank. The signals are stripped of their *d.c.* components and the *rf* component is amplified to the appropriate level by low noise wideband amplifiers. These signals are then demodulated and supply the phasemeter measurement channels.

#### 7.4.5 Phase locking servo

The free running lasers can be initially many GHz separated in frequency and the phase locking servo will not capture lock under these conditions. The beatnote of the two laser frequencies is manually driven to  $\sim 100$  MHz using the temperature control of one laser crystal. For this stage the beatnote is monitored using the high frequency photodiode (connected to a high frequency spectrum analyser) and then the scanning Fabry-Perot cavity, both shown in Figure 7.14. The scanning cavity has a free spectral range of 300 MHz. Convenient operating temperatures and injection currents must be chosen so that both lasers run single mode.

The phase locking is then accomplished by a dual feedback path to the slave laser. Analogue electronics are used to offset lock the slave laser to the free running master light in the region from  $\sim 0.5$  Hz to a few kHz (the laser piezo has a resonance at 320 kHz which limits the upper frequency of the gain). The phasemeter is used to provide a digital output for the frequencies below  $\sim 0.5$  Hz *via* a digital to analogue converter.

An EOM was placed in the slave light beam after noise at the heterodyne frequency was observed. This actuator was implemented as only limited gain at this frequency can be provided by the internal laser actuators. Improvements

to the servo system were made and preliminary investigations suggest the EOM path may not be needed: narrow band, high frequency noise around the heterodyne frequency was injected into the loop and no effect was seen in the low frequency phase noise spectrum.

#### 7.4.6 Test of measurement electronics using optical signals

With the interferometers and phase locking servo in place, the measurement electronics can be tested using optical signals. The slave laser was locked 15 MHz from the master laser frequency using the phase locking servo.

For the purpose of these tests only one interferometer is needed. The beatnote of the two lasers is initially split electronically immediately before the amplifiers, as shown in Figure 7.15. The beatnote is demodulated and used to lock the lasers. It is also used to measure the phase lock, *i.e.* this is an in-loop measurement. The current best result of this set up is shown in Figure 7.16.

Channel two is the apparent phase stability of the locking signal compared to the electrical reference signal. This can be driven arbitrarily quiet, depending only on the loop gain of the system. Channel one is the measurement channel apparent stability with respect to the electrical reference. Encouragingly, this appears to be limited by the electrical noise seen in Figure 7.13. Whether this is actually the case will be known when suitably phase stable amplifier systems are assembled.

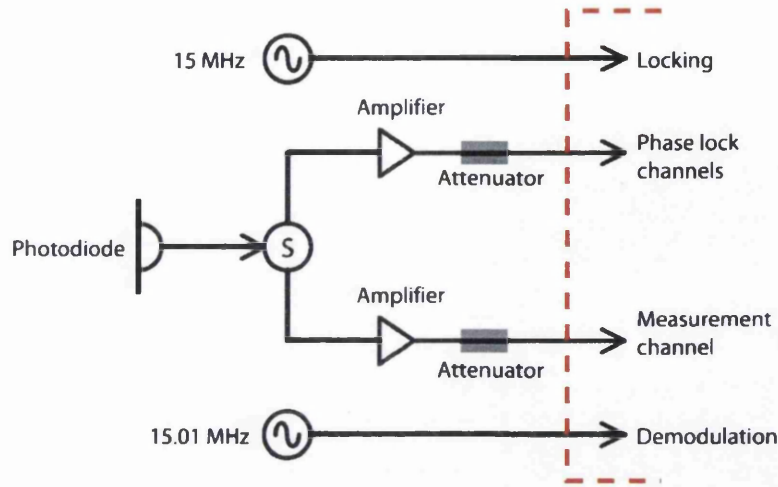


Figure 7.15: Diagram showing the set up for the test of the measurement electronics using an optical signal.

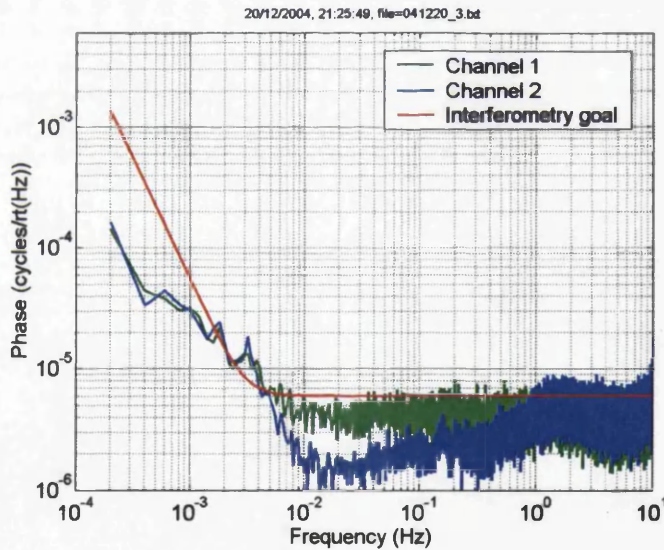


Figure 7.16: PSD showing apparent phase stability of the independently measured in-loop signal (channel one) and the locking signal (channel two) with respect to the electrical reference signal. The red line shows the interferometry target sensitivity, which is set by the shot noise limit of the weak light interference.

### 7.4.7 Attenuation

For the experiment to be relevant to LISA, the beam combination that is used for the phase locking must be heavily unbalanced, *i. e.* one beam must be attenuated. In the case of LISA this is an unwanted but unavoidable result of having large distances between spacecraft. The optical bench was originally designed to operate with equal power in each arm, so for the laboratory demonstration the attenuation is achieved by reflecting most of the light from one arm out of the optical system.

The ejection of light is achieved by placing four mirrors at an angle to the beam such that the attenuated transmitted beam continues in the same direction that the unattenuated beam traveled. For the specific mirrors used, this angle was  $27^\circ$  yielding a transmission of 2.5% through each mirror. By placing these mirrors as matched pairs the beam direction was maintained. These mirrors were assembled on a microscope slide as a unit prior to being placed in the beam and are shown in Figure 7.17 and in situ on the optical bench in Figure 7.18. These mirrors provide an attenuation reducing a beam of 1 mW to  $\sim 400$  pW.

If the additional material in one beam path introduces noise due to the extra beam path in fused silica then equivalent (but anti-reflection coated) pieces shall be placed in the other arm to balance transmissive paths in the two arms and thereby benefit from common mode rejection of temperature driven refractive index fluctuations.

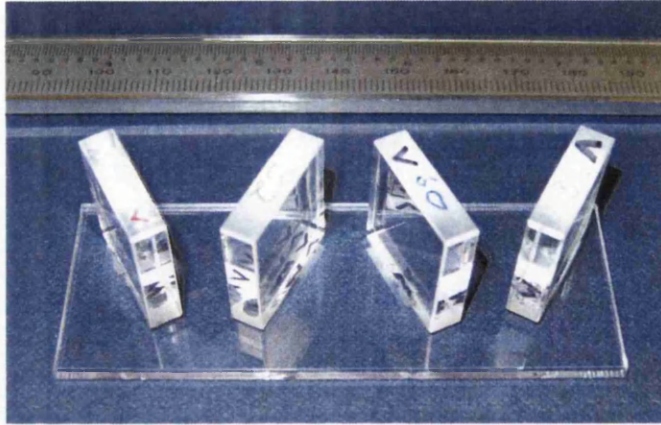


Figure 7.17: *Photograph of the beam attenuator subassembly.*

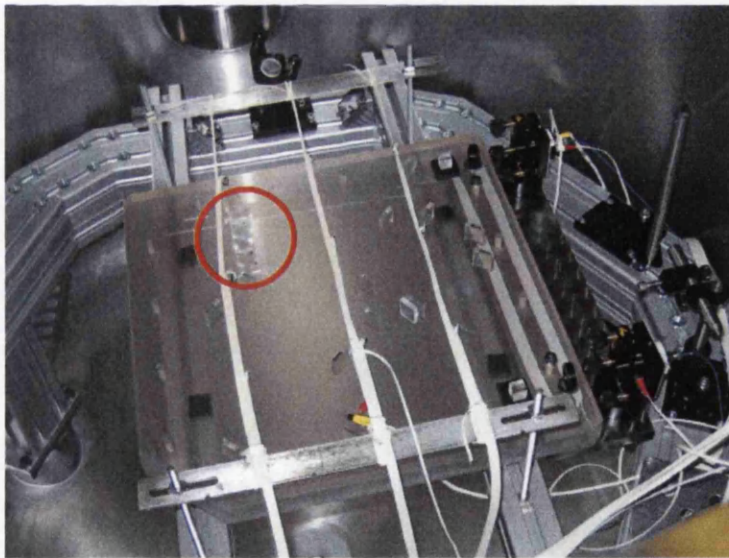


Figure 7.18: *Photograph of the beam attenuator subassembly in place on the optical bench (circled in red).*

## 7.5 Current status

The current issue appears to be the relative phase stability of the amplifier chains. The cause of the excess noise here is not yet fully understood but is under investigation. Once the amplifier chains are in place work can continue on testing the amplifier chains using a real optical signal.

The experiment will then be slightly modified so that the optical signal used to lock and measure will be *optically* split and two photodiodes used to provide the locking and measurement signals. This is to demonstrate that the individual photodiodes are not contributing excess noise (this would not be seen in the electrical splitting test as it would be common to both locking and measurement channels).

Once the optical splitting test has been successfully conducted the experiment will be run using the interferometers on the optical bench (initially with full light powers in each arm). This is not anticipated to be a difficult step as the optical bench has proven stability and therefore should not generate excess noise.

The final stage will be to lock the lasers using the weak light beatnote (which is already installed) and measure the apparent stability of the lock using the measurement ('full' power) interferometer. Success at this stage will mean that one approach to weak light phase locking at the LISA performance requirements will have been demonstrated.

# Chapter 8

## Conclusions

Ground-based gravitational wave detectors are currently taking data and could soon make the first direct detection of a gravitational wave. If detections are not made with this generation of detectors then it is widely believed that the second generation of detectors will open the field of gravitational wave astronomy.

To complement the ground-based work and access many interesting sources not available to ground-based detectors LISA is due for launch in the next decade. LISA Pathfinder will develop some of the many technological challenges that LISA faces. This thesis has discussed some of the issues relating to the optical interferometry to be used for LISA and LISA Pathfinder.

Techniques for the construction of optical benches able to satisfy the demanding requirements of ultra-stable low frequency space interferometry have been developed. These techniques have been used to construct the first optical bench of a new *genre*, which was demonstrated to be stable to the  $10 \text{ pm}/\sqrt{\text{Hz}}$  from 3 mHz to 30 mHz, with the exception of a minor spectral feature of temperature

driven excess noise when operated in a laboratory environment.

Valuable lessons learned during the construction and testing of the prototype optical bench have aided the successful construction and testing of the LTP engineering model optical bench interferometer.

The engineering model in turn has informed aspects of the flight model interferometer construction, which is currently under way. The tighter tolerances for the flight model have raised many additional challenges which are being addressed using new techniques and the development of custom components, all of which will be vital information when the time comes for designing and building the LISA optical benches.

While the LISA Pathfinder mission is required for investigation of the performance of some critical subsystems of LISA, there are other aspects of LISA technology that can be demonstrated on Earth. The continuing work on interferometry for LISA is reported, particularly the development of weak light laser phase locking. In this the demanding mixture of high frequency electronics and picometre stability low frequency interferometry with light at the few picoWatts level results in the experiments being affected by a variety of subtle problems. The experimental progress described is expected to provide useful insights into the problems to be encountered for the final LISA phase locking scheme and their solutions.

# Appendix A

## Optical test bench

This Appendix describes the design and construction of an optical test bench for prototype LISA Technology Package (LTP) and LISA phase measurement systems (PMS). This work was undertaken as part of an ESA programme of work [71]. The results of the testing are reported in full in [72] (for the LTP section) and [73] (for the LISA section).

### A.1 Approach

The requirements for testing a LTP type PMS are quite different to those for testing a LISA type PMS. For the LTP tests a signal of frequency between 0.5-2 kHz is required with a modulation depth of up to 90%. The LISA PMS tests require a signal in the frequency range 0.1-20 MHz with contrast of  $< 4 \times 10^{-4}$ .

The approach adopted was to divide the test bench into two separate blocks to produce suitable optical signals to stimulate photodiodes with phase-stable electrical reference signals. The light source was a monolithic Nd:YAG laser

with a wavelength of 1064 nm. The light was amplitude modulated at the desired frequency using the schemes described below.

### A.1.1 LTP modulation scheme

The LTP arm of the test bench was set up as shown in Figure A.1:

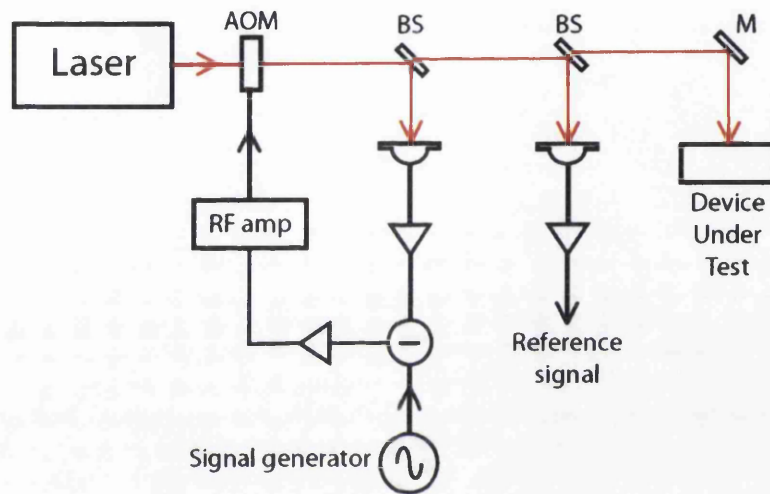


Figure A.1: Schematic layout of the LTP side of the optical test bench.

The beam passes through an acousto-optic modulator (AOM) and the light diffracted into the first order is split three ways:

- one beam is part of a closed loop servo,
- one beam is the optical reference and
- one beam is diverted to the device under test.

The modulation for the LTP arm is achieved *via* a control loop that forces the laser power at the AOM output to follow a user defined input. This is achieved using the *rf* drive to the AOM as an actuator. Figure A.2 shows how

the optical signal responds when the *rf* drive power has a signal applied to it. The closed loop servo is used to remove this non-linearity. Figure A.3 shows an independent measurement of the optical signal and the drive signal when the control loop is active.

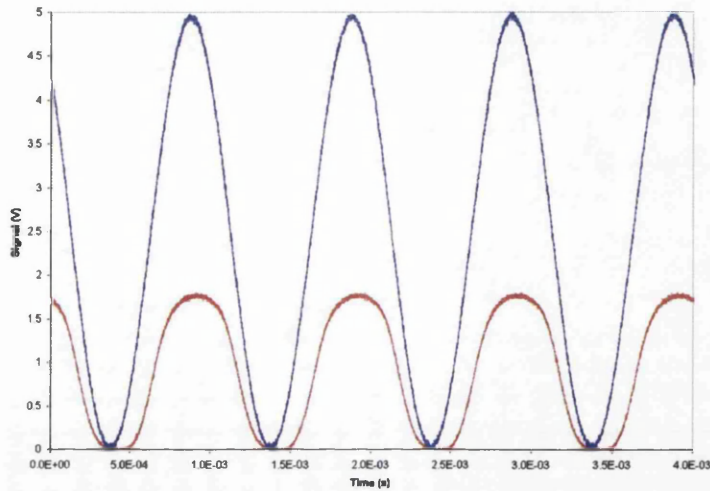


Figure A.2: Drive signal to AOM (blue) and optical signal (red) with no control loop.

The expected control loop performance was modeled and is plotted with the actual performance in Figure A.4. This shows a good match between predicted and experimental results with the control loop having a high bandwidth, good gain and phase margins. The overall effect is that the non-linearity of the AOM is no longer an issue. The phase of the signal from the device under test can thence be compared the reference phase to verify the LTP style PMS.

### A.1.2 LISA modulation scheme

The light after the AOM providing the LTP modulation signal can be stabilised and used as the input for the LISA modulation signal (*n.b.* in this mode of

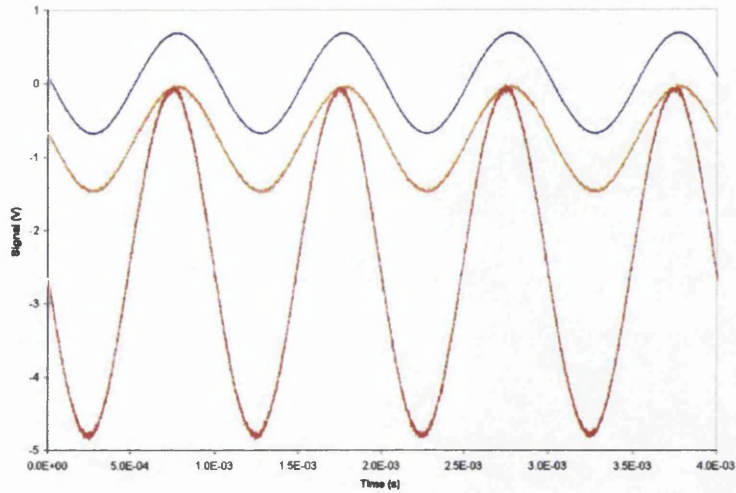


Figure A.3: Drive signal to AOM (blue), in loop signal (orange) and independent optical signal (red) with control loop on (the red line is entirely obscured by the blue trace).

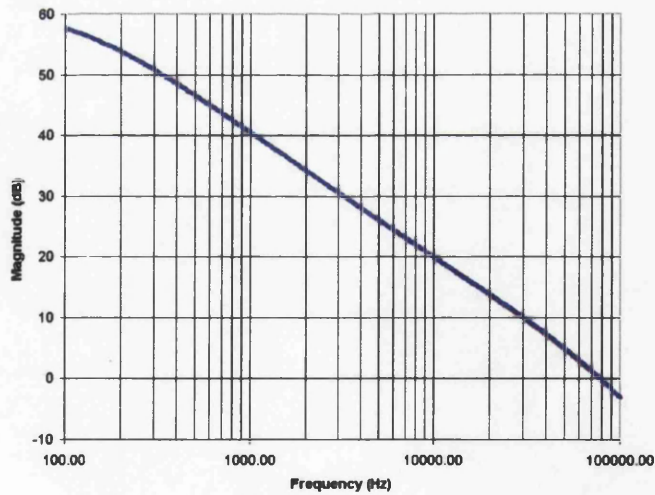


Figure A.4: Modeled (blue) and actual (red) control loop performance.

operation the LTP arm is used to stabilise the light and so cannot be used simultaneously). This is accomplished by supplying the AOM drive with a stable *d.c.* signal. This stable input light can then be modulated using an electro-optic modulator (EOM). This is a necessary transition as the AOM is suitable for low frequency signals of large amplitude variation and the EOM is capable of driving high frequency signals.

When a signal is applied to the EOM the plane of polarisation of the light at the EOM output is rotated. The EOM is followed in the optical chain by a polariser, the net effect being that the amplitude of the light is varied as the input signal.

The light from the polariser is then split into two beams, as shown in Figure A.5.

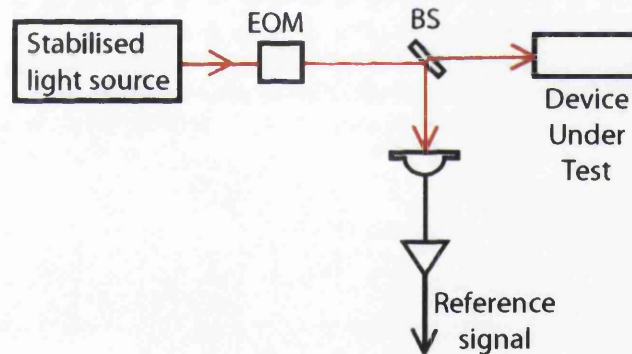


Figure A.5: Schematic layout of the LISA side of the optical test bench.

Similarly to the LTP arm, the signal from the device under test can then be compared with the reference signal to verify the LISA style PMS.





# Appendix B

## Optical fibre positioning unit

The correlation between laser beam direction and collimation from an optical fibre output and the position of the fibre end relative to the collimating lens, as well as overall pointing stability, must be well characterised to address design issues on the optical bench for the space based gravitational wave detector LISA [37]. A schematic of one of the LISA optical benches is shown in Figure B.1 (the fibre positioning unit is at the bottom left). It is clear from this diagram that the control of the fibre positioning unit is vital to the successful operation of the other components as a beam misdirection here would have ramifications at every other stage.

As well as being stable in the locked mode, the fibre positioning unit must also be able to move with fine resolution in a controlled manner. There is the need for redundancy in the system so that should a fibre or laser fail a backup can replace the failed hardware. The contingency plan is for the failed fibre end (or fibre end attached to the failed laser) to be moved away from the optical bench and a spare into its place. Also, the beam from the telescope is required to be defocussed during the acquisition phase by a movement of fibre end relative to

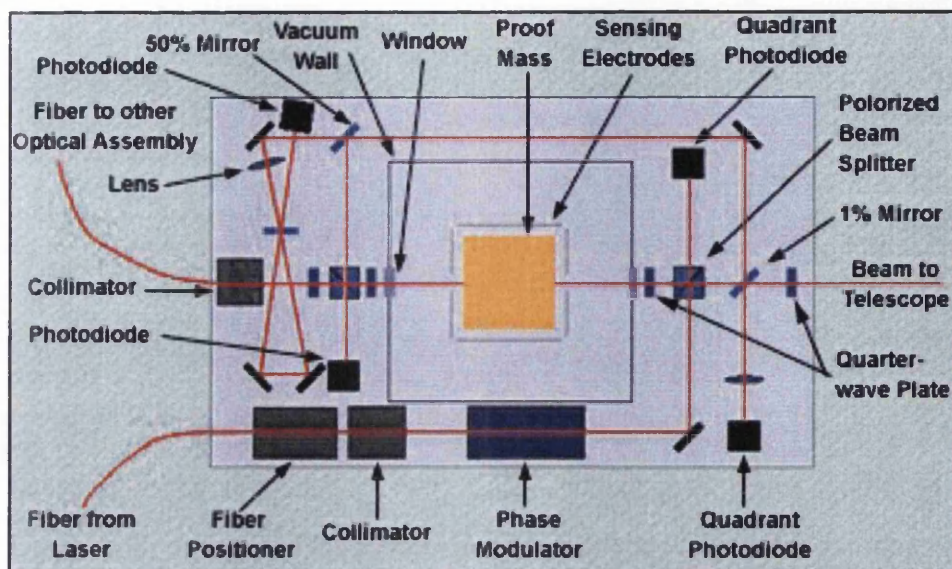


Figure B.1: *Schematic of the LISA optical bench.*

collimating lens.

This Section outlines the design of an experiment that aims to gather data on precision positioning units. To make this relevant to LISA issues stability measurements will be taken on long time scales. Temperature sensitivity will also be tested.

## B.1 LISA requirements

For LISA to achieve required sensitivities the beams to be emitted *via* the telescopes have a corresponding stability: the pointing error. These beams must be collimated during measurement periods to maximise the signal at each detector although a specific amount of defocus is required during the acquisition phase. The fibre positioning unit for LISA will have to be stable enough and have suitable positioning capabilities to satisfy the constraints

shown below.

Pointing error budget ( $\mu\text{rad}$ )	$\pm 0.50$	(ref [74])
Defocus for acquisition phase ( $\mu\text{rad}$ )	$\pm 11$	

## **B.2 Relating fibre end movement to optical bench field of view and to telescope field of view**

To appreciate how adjusting the fibre position will affect the overall point ahead angle (the angle between emitted and received beams) we need to know the relation between the fibre position to optical bench field of view and the optical bench field of view to telescope field of view. The field of view is the solid angle from which the detector receives radiation. After considering the practicalities of lens and fibre mounting it was thought more practically viable (and in line with current LISA plans) to adjust the fibre end position with respect to the coupling lens *i.e.* the lens remains fixed in position. So to control the light direction we need to control the fibre end and this depends on the actuator applying the force.

Figure B.2 shows how moving the fibre end laterally by a distance  $\delta x$  will alter the output field of view. Figure B.3 shows the effect of fibre end translation on the optical bench field of view (only the divergent situation is shown for clarity - if the fibre end was moved in the opposite direction, the beam would converge at the same rate that the shown beam diverges).

Figures B.4 and B.5 show how the changing optical bench field of view alters the telescope field of view. It should be noted that the telescope introduces

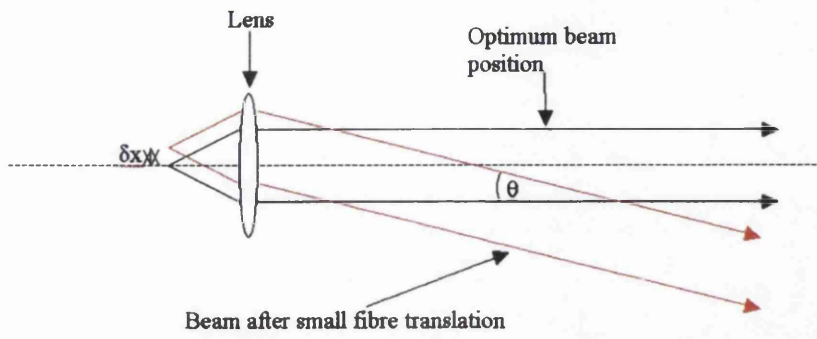


Figure B.2: *Effect of lateral fibre end movement on optical bench field of view.*

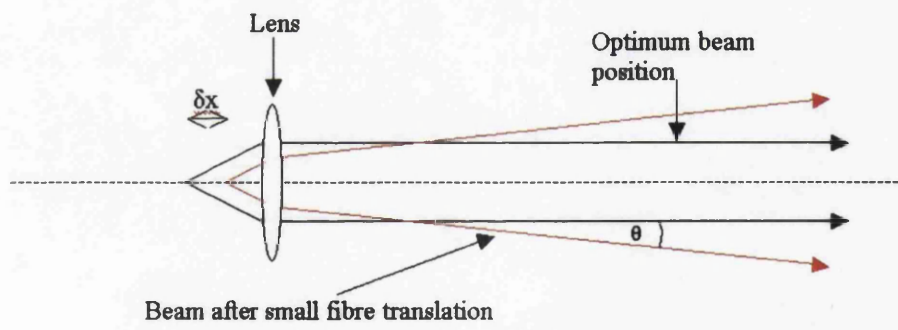


Figure B.3: *Effect of fibre end translation on optical bench field of view.*

an angular magnification of  $g_\alpha$  that has the effect of increasing the optical bench field of view by the magnification, *i.e.* the optical bench field of view corresponds to the telescope field of view multiplied by  $g_\alpha$ . The primary optics to be used for LISA are 30 cm Dall-Kirkham telescopes with an angular afocal magnification of  $60\times$ .

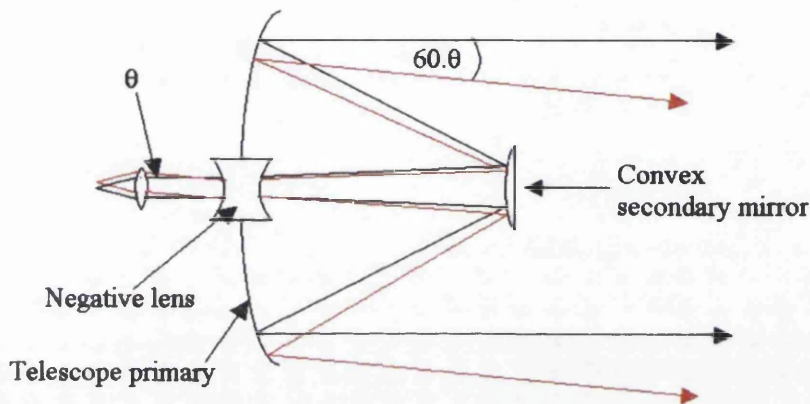


Figure B.4: *Effect of optical bench field of view on telescope field of view for lateral translation.*

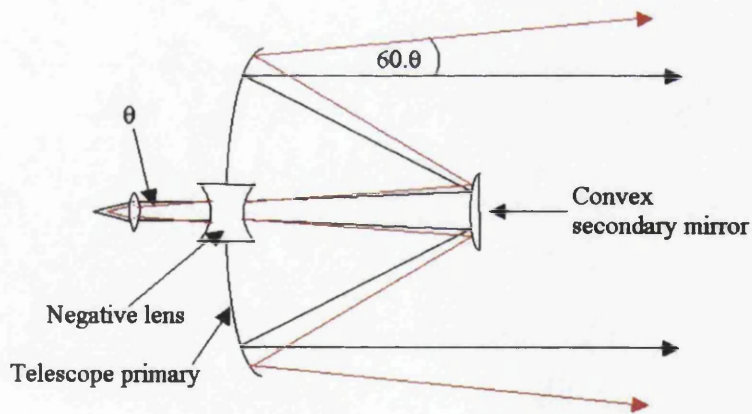


Figure B.5: *Effect of optical bench field of view on telescope field of view for defocus.*

### B.2.1 Calculating lateral translation of fibre end to telescope field of view relationship

Figure B.6 shows a sketch indicating the parameters used to calculate the relationship between lateral translation of fibre end and the telescope field of view.

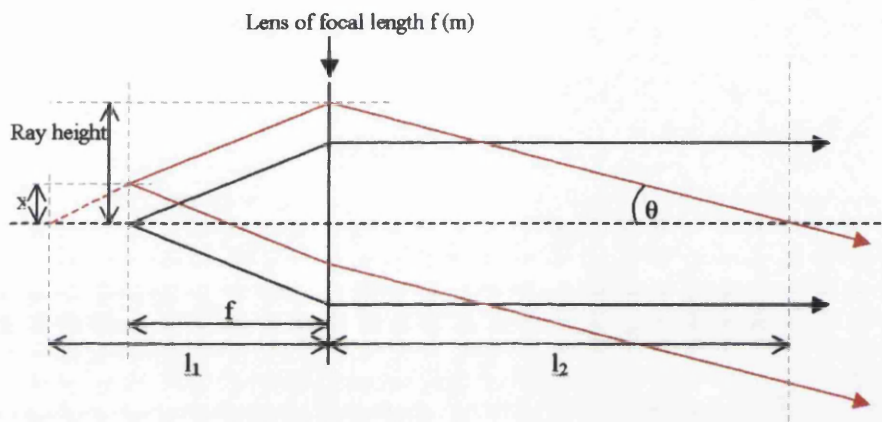


Figure B.6: Diagram showing parameters for calculating effect of lateral displacement of fibre end.

The light leaves the fibre end with a numerical aperture ( $NA$ ) which corresponds to an angle of  $\sin^{-1}(NA)$ . Using this,  $l_1$  is given by

$$l_1 = f + \frac{x}{\tan(\sin^{-1} NA)} \quad (B.1)$$

and then  $l_2$  by

$$l_2 = \frac{1}{\frac{1}{f} - \frac{1}{l_1}} \quad (B.2)$$

We can see that the ray height is given by

$$\text{Rayheight} = f \{ \tan(\sin^{-1} NA) \} \quad (\text{B.3})$$

and thus the optical bench field of view by

$$\theta = \tan^{-1} \left[ \frac{x + f \{ \tan(\sin^{-1} NA) \}}{l_2} \right] \quad (\text{B.4})$$

where  $\theta$  is the optical bench field of view. The telescope field of view is related to the optical bench field of view as

$$\text{Telescope field of view} = \frac{\text{Optical bench field of view}}{g_\alpha} \quad (\text{B.5})$$

Figure B.7 is obtained by plotting suitable values of fibre end position ( $x$ ) against telescope field of view. From this we can see that a  $0.58285 \mu\text{m}$  adjustment at the fibre end yields a  $0.5 \mu\text{rad}$  change in the telescope field of view. This suggests a comprehensive data set would contain measurements every  $10 \text{ nm}$  over a  $1 \mu\text{m}$  range around the critical value.

### **B.2.2 Calculating defocus of beam from fibre to telescope field of view relationship**

Using a similar process as in Section B.2.1, we arrive at Figure B.8 for beam defocus. Note that moving the fibre along the optical axis to the left or to the right in this sketch causes the same magnitude of defocus. The beam is required to be convergent for acquisition but I have shown the divergent beam here also as it is needed to calculate  $l_2$ .

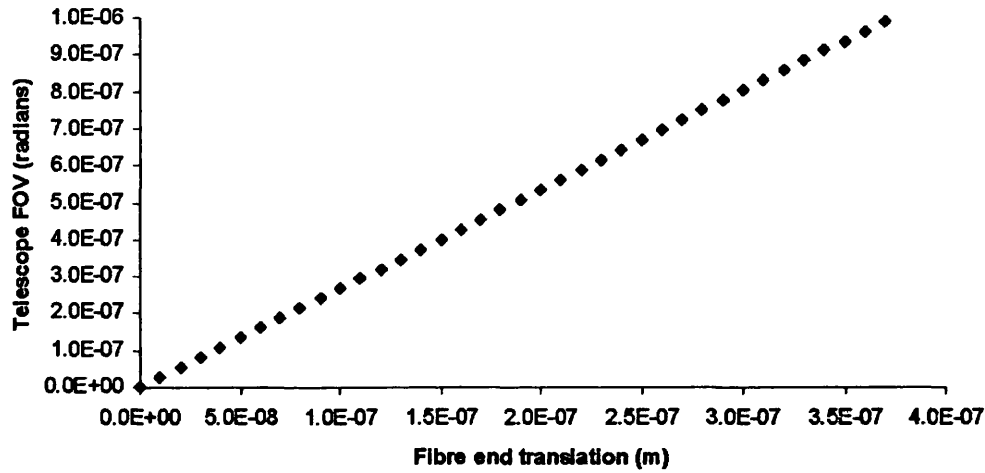


Figure B.7: *Lateral translation of fibre end versus telescope field of view.*

We know that in this case  $l_1 = f \pm d$ . We can calculate  $l_2$  using the thin lens equation:

$$l_2 = \frac{1}{\frac{1}{f} - \frac{1}{f+d}} \tag{B.6}$$

and the ray height is given by

$$\text{Rayheight} = \{f + d\} \times \{\tan(\sin^{-1} NA)\}. \tag{B.7}$$

From this we can calculate the optical bench field of view;

$$\theta = \tan^{-1} \left( \frac{\text{Rayheight}}{l_2} \right) \tag{B.8}$$

We convert the optical bench field of view to telescope field of view as in equation B.5 and plot fibre position against telescope field of view as shown in

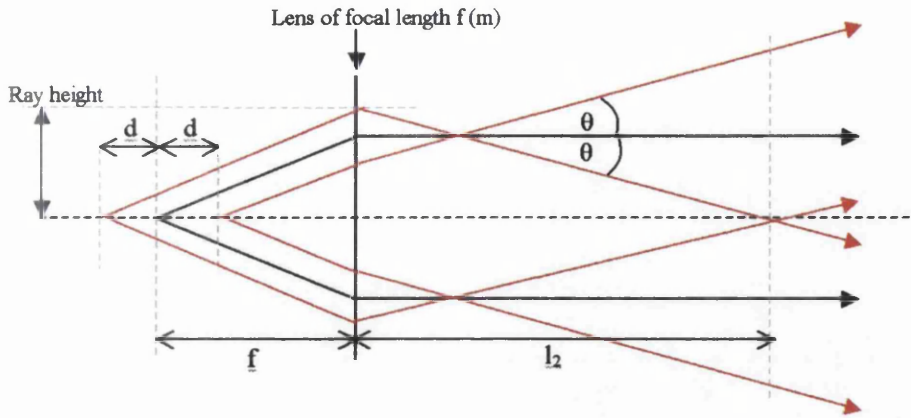


Figure B.8: *Diagram showing parameters for calculating effect of defocus.*

Figure B.9. From this we see that to achieve the required  $11 \mu\text{rad}$  change in telescope field of view for acquisition we must move the fibre end towards the collimating lens by  $29.38 \mu\text{m}$ . This positioning accuracy required for defocus is of the order  $100\times$  less sensitive than for lateral translation.

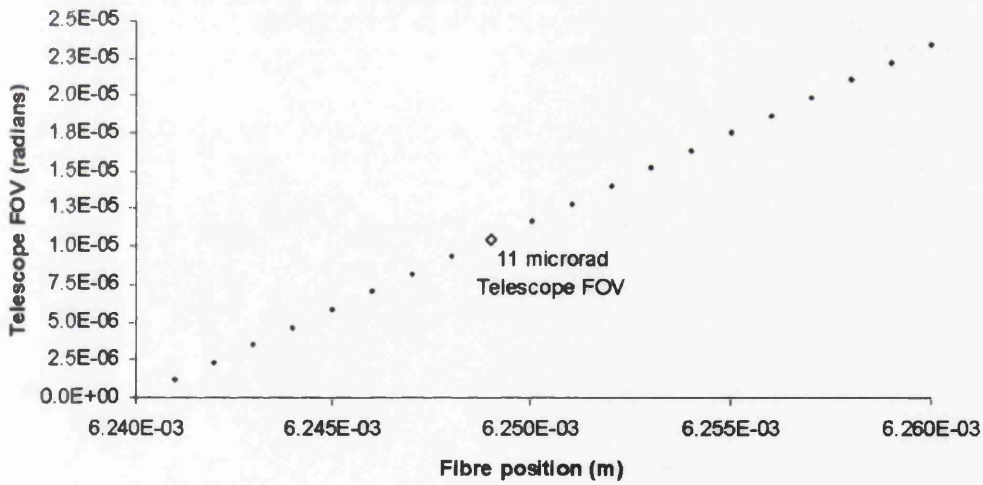


Figure B.9: *Lateral translation of fibre end versus telescope field of view.*

## B.3 Measurement requirements

The actuator motion needs to be measured to an accuracy that will demonstrate whether it is capable of fulfilling the requirements for the fibre positioning unit. For the smallest measurement (lateral translation of the fibre end relative to coupling lens) the maximum acceptable change in optical bench field of view is  $30\ \mu\text{rad}$ . This corresponds to an actuator translation of  $0.58285\ \mu\text{m}$ . The behaviour of the actuator needs to be characterised up to and beyond this point, so a target resolution of the measuring system should be of the order of  $1\ \mu\text{rad}$ . If the measurement occurs at a distance of 1 m from the coupling lens, this translates to a change in beam waist of  $1\ \mu\text{m}$ . It is proposed that the actuator shall move a mirror that is part of a Mach-Zender interferometer. The interference pattern at the output of the interferometer can be observed and the movement of the mirror inferred.

Control tests will be conducted without an actuator in the system to ensure that the noise level inherent to the apparatus is below the sensitivity we are trying to measure. Temperature sensitivity will also be characterised.

## B.4 Current status

An in depth study of available actuator technologies has been carried out and an actuator has been chosen. An actuator stage using a UHVL Inchworm® motor from EXFO Burleigh Products Group will be tested (model number: UHVL-1100) which has 25 mm of travel and a specified resolution of 20 nm. This shall be driven by a single axis controller (model number: 8200-1-1) with GPIB interface. The data acquisition system is to be finalised.

Since starting on the study it has been realised that an investigation into actuator technology is also required for the LISA telescope articulation mechanism which may require actuation at the 0.1 nm level. While it is unlikely this experiment will measure movements of that size it will be a relevant first test of this technology for both the fibre positioning unit and the telescope articulation mechanism.

The actuator tests will be carried out at the CCLRC Rutherford Appleton Laboratory in Oxford.

## Appendix C

# Investigation of amplitude modulation created by acousto-optic modulators

An investigation to study the magnitude of amplitude modulated light present on light from acousto-optic modulators was undertaken as part of a study headed by the Albert Einstein Institute in Hannover.

In the context of this work acousto-optic modulators are employed to frequency shift the light. Of particular interest is the beatnote signal at a photodiode when an acousto-optic modulator is driven by two frequencies.

The following report is entered as it was presented.

An investigation of signal generation at a photodiode  
when two frequencies of light with different amplitude  
are present.

Christian Killow  
Institute for Gravitational Research,  
Department of Physics and Astronomy,  
University of Glasgow,  
Glasgow.  
G12 8QQ

March 10, 2005

**Abstract**

During stability tests of the prototype optical bench (OB) at Glasgow two acousto-optic modulators (AOMs) were driven at slightly different frequencies. It was noted that light of both frequencies was present on the signal from the output photodiodes even when light from only one AOM was present (these signals were not due to direct electrical  $rf$  pick-up at the photodiode).

This investigation was undertaken to establish how the level of spurious heterodyne frequency signal (arising from the two frequencies of light having been mixed at the photodiode) varies with the level of drive frequency signals.

It was found that the level of spurious signal varies linearly with the difference between the two drive frequency signal amplitudes over a wide range of laser powers and  $rf$  drive levels.

**Distribution List**

<b>Distribution List</b>	<b>Affiliation</b>
D Robertson	UGL
H Ward	UGL

**Issue Record**

<b>Date</b>	<b>Issue/Revision</b>	<b>Comments</b>
07:02:2005	0.1	Draft for comments
10:03:2005	0.2	Updated after comments by D Robertson

## 1 Introduction

The set up for the monolithic optical bench (OB) stability tests at Glasgow comprised of one laser (Nd:YAG NPRO laser operating at 1064 nm) split and directed through two individual acousto-optic modulators (AOMs). One AOM was driven at 80 MHz and the other at 80.01 MHz. The AOMs were aligned so as to deliver most of the light into the first order. This was in order to generate a beatnote at a convenient frequency ( $\sim$ kHz) upon beam recombination. These beams were sent through fibres and onto the OB where they were split and recombined in three places, making three Mach-Zender interferometers. The recombined beams left the OB and were measured using single element silicon photodiodes.

When one beam was blocked before travelling through an AOM, a small amount of signal at 10 kHz (the heterodyne frequency) was detected at the photodiode, suggesting that both 80 and 80.01 MHz signals were present at the photodiode. This 10 kHz signal was not present when the second beam was blocked, eliminating direct electrical *rf* pick-up as the source. The mechanism for a signal at the heterodyne frequency appearing at the photodiode under these circumstances is the mixing of light beams shifted in frequency from the original by the two drive frequencies.

The level of *rf* drive to the AOMs was of order 1.5 W, which was provided by using signal generators and power amplifiers. While much care was taken to avoid pick-up between the two transmission lines, it is very difficult to keep this level of *rf* power from being omnipresent at some level in a compact experimental arrangement.

## 2 Test set up

The apparatus was set up as shown in figure 1. A Nd:YAG NPRO laser operating at 1064 nm was directed through a single AOM and the beam was incident on a single element silicon photodiode. Some of the laser beam was also directed into a Fabry-Perot scanning cavity (not shown) to ensure the laser was running single mode for all measurements.

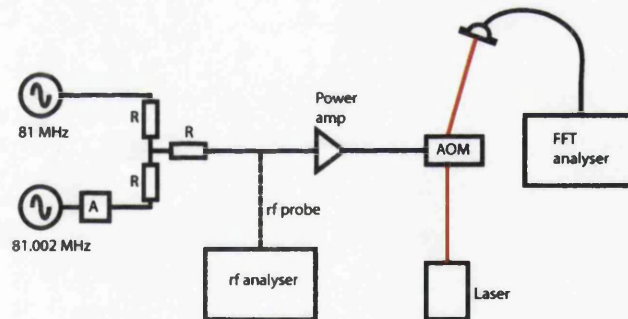


Figure 1: Schematic layout of experiment. 'A' represents a signal attenuator, 'R' represents 17 Ohm resistors.

The AOM drive was from two signal generators, combined using a resistive network, and power amp. A high frequency probe attached to a spectrum analyser was used immediately before the power amplifier to measure the absolute and relative levels of the signals from

the two generators. The output of the photodiode was connected to either an oscilloscope (for dc light level measurements) or FFT analyser (to measure the amplitude of the 2 kHz signal).

The aim was to drive the AOM with two frequencies (whose amplitude could be varied) and measure the beatnote level from the photodiode under varying conditions. The drive frequency for the AOM was 81 MHz with the second drive frequency being 2 kHz away at 81.002 MHz. These values were chosen for the spectral purity of the generators and as a heterodyne frequency of the order of 2 kHz is expected for LISA Pathfinder.

### 3 Results and conclusions

Data was taken showing that the actual drive to the AOM (after the power amplifier) was linear as the signal generator output level was increased over the entire range that readings were taken.

Figure 2 shows the dc light level at the photodiode as a function of *rf* drive (the power amplifier adds  $\sim 35$  dB to this). This shows how the optical power level in the diffracted beam varies non-linearly with applied *rf* power.

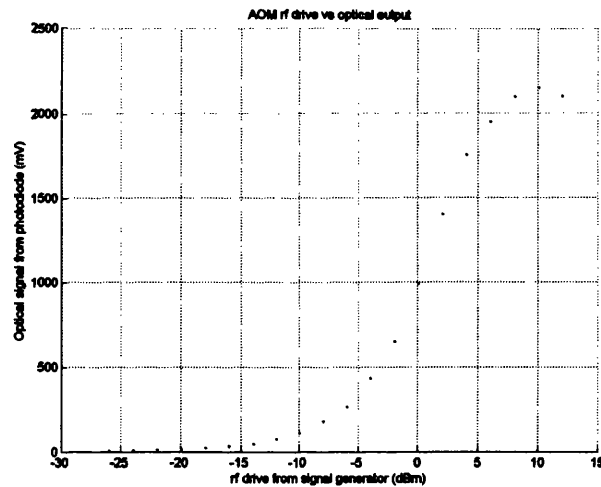


Figure 2: Plot showing dc light level at photodiode as a function of *rf* drive from signal generator

Figure 3 shows the size of the 2 kHz signal from the photodiode against the difference in signal size of the drive frequencies for three different set ups. The variables are as follows:

- Laser injection current ( $i_1 = 0.765$  A,  $i_2 = 1.1$  A)
- dc voltage from photodiode ( $v_1 = 0.368$  V,  $v_2 = 1.95$  V,  $v_3 = 0.834$  V)

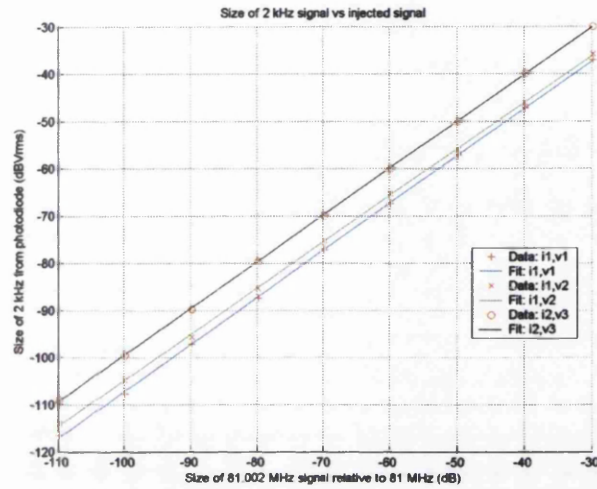


Figure 3: Plot showing magnitude of 2 kHz signal as a function of 81.002 MHz amplitude with respect to 81 MHz amplitude. Points are experimental data, solid lines are fits.

The solid lines indicate the fits (as calculated by Matlab) for which the gradients are all approximately 1 and the offset varies slightly. Thus the level of spurious 2 kHz signal varies linearly with the difference between the two drive frequency signal amplitudes over a wide range of laser powers and *rf* drive levels.

# Bibliography

- [1] LISA Study Team. *Pre-Phase A Report, second edition*, July 1998.
- [2] Astrium GmbH. *Optical Metrology Subsystem Requirements Specification, S2-ASD-RS-3010 Issue1*, February 2005.
- [3] A. Einstein. *Näherungsweise Integration der Feldgleichungen der Gravitation. Sitzungsber Preuss. Akad. Wiss*, 688, 1916.
- [4] H. Bondi. *Relativity. Rep. Prog. Phys.*, 22 No. 1:97–120, 1959.
- [5] B. Schutz. *Gravitational wave astronomy. Class. Quantum Grav.*, 16:A131–A156, 1999.
- [6] David G. Blair. *The Detection of Gravitational Waves*. Cambridge University Press, 1991.
- [7] B. Allen and J. D. Romano. *Detecting a stochastic background of gravitational radiation: Signal processing strategies and sensitivities. Phys. Rev. D*, 59, 1999.
- [8] N. A. Robertson. *Laser interferometric gravitational wave detectors. Class. Quantum Grav.*, 17:R19–R40, 2000.
- [9] R.A. Hulse and J. H. Taylor. *Discovery of a pulsar in a binary system. Astrophys. J.*, 195:51–53, 1975.

- [10] J. H. Taylor, R. A. Hulse, L. A. Fowler, G. E. Gullahorn, and J. M. Rankin. *Further observations of the binary pulsar PSR 1913+16*. *Astrophys. J.*, 206:53–58, 1976.
- [11] J. H. Taylor and J. M. Weisberg. *A new test of general relativity: Gravitational radiation and the binary pulsar PSR 1913+16*. *Astrophys. J.*, 253:908–920, 1982.
- [12] J. H. Taylor and J. M. Weisberg. *Further experimental test of relativistic gravity using the binary pulsar PSR 1913+16*. *Astrophys. J.*, 345:434–450, 1989.
- [13] J. Weber. *Detection and Generation of Gravitational Waves*. *Phys. Rev.*, 117:306–313, 1960.
- [14] J. Weber. *Evidence for discovery of gravitational radiation*. *Phys. Rev.*, 22:1320–1324, 1969.
- [15] A. de Waard, L. Gottardi, and G. Frossati. *MiniGRAIL progress report 2001: the first cooldown*. *Class. Quantum Grav.*, 19:1935–1941, 2002.
- [16] O. D. Aguiar *et. al.* *The status of the Brazilian spherical detector*. *Class. Quantum Grav.*, 19:1949–1953, 2002.
- [17] P. Astone. *Resonant mass detectors: present status*. *Class. Quantum Grav.*, 19:1227–1235, 2002.
- [18] B. Wilke for the GEO600 Team. *The GEO 600 gravitational wave detector*. *Class. Quantum Grav.*, 19:1377–1387, 2002.
- [19] A. M. Sintes for the GEO600 Team. *Detector characterization in GEO 600*. *Class. Quantum Grav.*, 20:S731–S739, 2003.

- [20] M. Hewitson for the GEO600 Team. *A report on the status of the GEO 600 gravitational wave detector*. *Class. Quantum Grav.*, 20:S581–S591, 2003.
- [21] B. Wilke for the GEO600 Team. *Status of GEO 600*. *Class. Quantum Grav.*, 21:S417–S423, 2004.
- [22] J. R. Smith for the GEO600 Team. *Commissioning, characterization and operation of the dual-recycled GEO 600*. *Class. Quantum Grav.*, 21:S1737–S1745, 2004.
- [23] B. Allen and G. Woan for the LIGO Scientific Collaboration. *Upper limits on the strength of periodic gravitational waves from PSR J1939+2134*. *Class. Quantum Grav.*, 21:S671–S676, 2004.
- [24] B. Abbott and The LIGO Scientific Collaboration. *Setting upper limits on the strength of periodic gravitational waves from PSR J1939+2134 using the first science data from the GEO 600 and LIGO detectors*. *Phys. Rev. D*, 69, 2004.
- [25] H. Grote for the GEO600 Team. *The status of GEO 600*. *Class. Quantum Grav.*, 22:S193–S198, 2005.
- [26] B. Abbott and The LIGO Scientific Collaboration. *First upper limits from LIGO on gravitational wave bursts*. *Phys. Rev. D*, 69, 2004.
- [27] B. Abbott and The LIGO Scientific Collaboration. *Analysis of LIGO data for gravitational waves from binary neutron stars*. *Phys. Rev. D*, 69, 2004.
- [28] B. Abbott and The LIGO Scientific Collaboration. *Analysis of first LIGO science data for stochastic gravitational waves*. *Phys. Rev. D*, 69, 2004.

- [29] B. Abbott and The LIGO Scientific Collaboration. *Search for gravitational waves associated with the gamma ray burst GRB030329 using the LIGO detectors.* *Phys. Rev. D*, 72, 2005.
- [30] B. Abbott and The LIGO Scientific Collaboration. *Upper limits on gravitational wave bursts in LIGO's second science run.* *Phys. Rev. D*, 72, 2005.
- [31] N. Robertson *et. al.* *Quadruple suspension design for Advanced LIGO.* *Class. Quantum Grav.*, 19:4043–4058, 2002.
- [32] A. Weinstein. *Advanced LIGO optical configuration and prototyping effort.* *Class. Quantum Grav.*, 19:1575–1584, 2002.
- [33] F. Acernese and the VIRGO Team. *Status of VIRGO.* *Class. Quantum Grav.*, 22:S869–S880, 2005.
- [34] M. Ando and the TAMA300 Team. *Observation results by the TAMA300 detector on gravitational wave bursts from stellar-core collapses.* *Phys. Rev. D*, 71, 2005.
- [35] S. Kawamura. *Status and plans for future generations of ground-based interferometric gravitational wave antennas.* *Class. Quantum Grav.*, 20:S127–S134, 2003.
- [36] European Space Agency ESA-SCI (2000) 11. *Laser Interferometer Space Antenna: A Cornerstone Mission for the Observation of Gravitational Waves. System and Technology Report*, 2000.
- [37] Astrium GmbH. *Final Technical Report, Report No. LI-RP-DS-009*, April 2000.
- [38] S. Anza and the LTP Team. *The LTP experiment on the LISA Pathfinder mission.* *Class. Quantum Grav.*, 22:S125–S138, 2005.

- [39] W. Fichter, P. Gath, S. Vitale, and D. Bortoluzzi. *LISA Pathfinder drag-free control and system implications*. *Class. Quantum Grav.*, 22:S139–S148, 2005.
- [40] R. Spero and A. Kuhnert. *The ST7 interferometer*. *Class. Quantum Grav.*, 21:S589–S595, 2004.
- [41] G. Heinzel, C. Braxmaier, R. Schilling, A. Rüdiger, D. Robertson, M. te Plate, V. Wand, K. Arai, U. Johann, and K. Danzmann. *Interferometry for the LISA technology package (LTP) aboard SMART-2*. *Class. Quantum Grav.*, 20:S153–S161, 2003.
- [42] C. Braxmaier, G. Heinzel, K. F. Middleton, M. E. Caldwell, W. Konrad, H. Stockburger, S. Lucarelli, M. B. te Plate, V. Wand, A. C. García, F. Draaisma, J. Pijenburg, D. I. Robertson, C. Killow, H. Ward, K. Danzmann, and U. A. Johann. *LISA pathfinder optical interferometry. Optical Fabrication, Metrology and Material Advancements for Telescopes. Proceedings of the SPIE. Edited by J. Hough and G. H. Sanders*, pages 164–173, 2004.
- [43] E. J. Ellife, J. Bogenstahl, A. Deshpande, J. Hough, C. Killow, S. Reid, D. Robertson, S. Rowan, H. Ward, and G. Cagnoli. *Hydroxide-catalysis bonding for stable optical systems for space*. *Class. Quantum Grav.*, 22:S257–S267, 2005.
- [44] Eoin Elliffe. *Aspects of Thermal Noise Modeling in Ground-based Gravitational Wave Detectors and Developments of Hydroxide Catalysis Bonding for Space-based Gravitational Wave Detectors and other Optical Applications*. PhD Thesis, University of Glasgow, 2005.
- [45] <http://www.schott.com>.

- [46] G. Heinzel, V. Wand, A. García, O. Jennrich, C. Braxmaier, D. Robertson, K. Middleton, D. Hoyland, A. Rüdiger, R. Schilling, U. Johann, and K. Danzmann. *The LTP interferometer and phasemeter. Class. Quantum Grav.*, 21:S581–S587, 2004.
- [47] D. I. Robertson for the LTP OBI Team. *S2-UGL-TN-3011 Scattered Light*, Feb 2006.
- [48] Felipe Guzmán Cervantes for the LTP OBI Team. *S2-UGL-TN-3017 Stray Light Analysis*, April 2006.
- [49] David Robertson, Christian Killow, Harry Ward, Jim Hough, Gerhard Heinzel, Antonio García, Vinzenz Wand, Ulrich Johann, and Claus Braxmaier. *LTP interferometer - noise sources and performance. Classical and Quantum Gravity*, 22(10):S155–S163, 2005.
- [50] [www.corning.com/semiconductoroptics/](http://www.corning.com/semiconductoroptics/).
- [51] Paul McNamara. *Development of optical techniques for spaceborne laser interferometric gravitational wave detectors*. PhD Thesis, University of Glasgow, 1998.
- [52] Logitech Ltd. *Equipment manual for the operation and maintenance of the GI20 measurement system, Ref: BE-04-6-4*.
- [53] H. Kogelnik. *On the Propagation of Gaussian Beams of Light Through Lenslike Media Including those with a Loss or Gain Variation. Applied Optics*, 4, No. 12:1562–1569, 1965.
- [54] <http://www.mathworks.com/products/matlab/>.
- [55] Innolight GmbH. *Mephisto Products Users Guide, version 4.6*, October 2004.
- [56] Motorola Inc. *Semiconductor Technical Data CA2832C/D*, 1994.

- [57] Analog Devices. *AD790 Data Sheet, Revision B. C1323-10-10/89*.
- [58] O. Jennrich, P. McNamara, D. Robertson, S. Rowan, H. Ward, and J. Hough. *Interferometry Developments for LISA and SMART-2*. *Class. Quantum Grav.*, 19:1731–1737, 2002.
- [59] Anthony E. Siegman. *Lasers*. Oxford University Press, 1981.
- [60] V. Wand, J. Bogenstahl, C. Braxmaier, K. Danzmann A. García, F. Guzmán, G. Heinzel, J. Hough, O. Jennrich, C. Killow, D. Robertson, Z. Sodnik, F. Steier, and H. Ward. *Noise sources in the LTP heterodyne interferometer*. *Class. Quantum Grav.*, 23:S159–S167, 2006.
- [61] K. Middleton. *OB-TN-3621-002 SMART-2 Optical Bench Engineering Model Optical Prescription*, January 2003.
- [62] [www.sukhamburg.de](http://www.sukhamburg.de).
- [63] G. Heinzel, C. Braxmaier, M. Caldwell, K. Danzmann, F. Draaisma, A. García, J. Hough, O. Jennrich, U. Johann, C. Killow, K. Middleton, M. te Plate, D. Robertson, A. Rüdiger, R. Schilling, F. Steier, V. Wand, and H. Ward. *Successful testing of the LISA Technology Package (LTP) interferometer engineering model*. *Class. Quantum Grav.*, 22:S149–S154, 2005.
- [64] <http://www.lightpath.com>.
- [65] <http://www.gnuplot.info/>.
- [66] C. Killow for the LTP OBI Team. *S2-UGL-TN-3009 Technical note on required alignment precision for construction of the LTP optical bench interferometer*, June 2005.
- [67] C. Killow for the LTP OBI Team. *S2-UGL-PL-3004 Strength test plan for ground-polished bonding*, May 2005.

- [68] C. Killow for the LTP OBI Team. *S2-UGL-TN-3009 Strength test report on ground-polished bonding*, June 2005.
- [69] P. Horowitz and W. Hill. *The Art of Electronics*. Cambridge University Press, 1986.
- [70] <http://optoelectronics.perkinelmer.com>.
- [71] ESA contract number 15580/01/NL/HB. *The LISA Technology Package on board SMART-2*, October 2002.
- [72] Systems Engineering and Assessment Ltd (copyrighted). *SMART2 PMS Model Integration and Test Procedures and Test Results*, ESTEC contract number 15658/01/NL/EC, January 2005.
- [73] Systems Engineering and Assessment Ltd (copyrighted). *LISA PMS Front-End Model Integration, Test Procedures, and Test Results*, ESTEC contract number 15658/01/NL/EC, November 2004.
- [74] Astrium GmbH. *Study of Laser Interferometer Space Antenna, DSS Report No. LI-RP-DS-005*, February 2000.